Design of the Extraction Arc for the 2$^{\text{nd}}$ Beam Line of the Free-Electron Laser FLASH

Dissertation
zur Erlangung des Doktorgrades
des Department Physik
der Universität Hamburg

vorgelegt von
Matthias Scholz
aus Maulbronn

Hamburg
2013

Gutachter der Dissertation:	Prof. Dr. Jörg Roßbach Prof. Dr. Eckhard Elsen
Gutachter der Disputation:	Prof. Dr. Jörg Roßbach Prof. Dr. Florian Grüner
Datum der Disputation:	27. September 2013
Vorsitzender des Prüfungsausschusses:	Dr. Torsten Limberg
Vorsitzender des Promotionsausschusses:	Prof. Dr. Peter Hausschildt
Dekan der Fakultät für Mathematik, Informatik und Naturwissenschaften:	Prof. Dr. Heinrich Graener

Abstract

In this thesis, I will deal with the design of the extraction arc for the second beam line of FLASH, an FEL (Free-Electron Laser) user facility at DESY Hamburg. Both beam lines will use the same linear accelerator and their separation will take place behind the last accelerating module. I will present the constraints for the extraction arc given by the beam line layout of the existing machine, by the building environment of the new beam line and in particular, by coherent synchrotron radiation (CSR). The impact from CSR will be presented and I will show how to mitigate these effects and what that means for the beam line design. The optimization of the extraction arc was done applying the downhill simplex algorithm which will be presented, first in its basic form to explain the operation principle and then in a more advanced version as used in the applied program. I will introduce in this thesis the final layout of the extraction arc including the following matching section. This layout fulfills all given constraints and can provide the required electron beam quality for FEL operation. In order to prove this, I will present start-to-end simulations for different bunch charges and for two different wave length.

Zusammenfassung

In dieser Dissertation befasse ich mich mit dem Design des Extraktionsbogens für die zweite Beamline von FLASH, einer FEL (Freier-Elektronen Laser) Nutzeranlage am DESY Hamburg. Beide Beamlines werden den gleichen Linearbeschleuniger nutzen und ihre Trennung wird hinter dem letzten Beschleunigermodul stattfinden. Ich werde die Einschränkungen für den Extraktionsbogen, gegeben durch die Beamline der existierenden Maschine, durch die Gebäudeumgebung der neuen Beamline und besonders durch kohärente Synchrotronstrahlung (Coherent synchrtron radiation, CSR), vorstellen. Die Auswirkung von CSR wird beschrieben und ich werde aufzeigen, wie diese Effekte abgeschwächt werden können und welche Auswirkung das auf die Beamlinegestaltung hat. Zur Optimierung des Extraktionsbogens wurde der Downhill-Simplex-Algorithmus verwendet, welcher vorgestellt werden wird, zunächst in einer grundlegenden Form um sein Funktionsprinzip zu erklären, und dann in einer erweiterten Version, wie er in dem angewendeten Programm eingesetzt wurde. Ich werde in dieser Dissertation den endgültigen Aufbau des Extraktionsbogens vorstellen. Dieser Aufbau erfüllt alle gegebenen Anforderungen und kann die, für den FEL-Betrieb notwendige Elektronenstrahlqualität bereitstellen. Um das zu belegen, werden Start-to-End Simulationen für verschiedene Ladungen und für zwei verschiedene Wellenlängen vorgestellt.

Contents

1. Introduction **1**

2. High-Gain Free-Electron Laser **7**

3. Coherent Synchrotron Radiation **19**

4. FLASH II Project **27**

5. Multi Variable Optimization **33**

- 5.1. Introduction 33
- 5.2. Optimization Function 33
- 5.3. Downhill Simplex Algorithm 34
- 5.4. Optimization Procedure for the New Beam Line FLASH2 40

6. FLASH2 Beam Line Layout **49**

- 6.1. Introduction 49
- 6.2. Beam Distribution to the New Beam Line 49
- 6.3. Optimization of the Longitudinal Phase Space Evolution 51
- 6.4. Optimization of the Transverse Phase Space Evolution 57

7. FLASH2 Start to End Simulations **75**

- 7.1. Introduction 75
- 7.2. Start-to-End Simulations Using a 100 pC Bunch 76
  - 7.2.1. Particle Tracking Through the Extraction Arc 76
  - 7.2.2. FEL Simulations 78
- 7.3. Start-to-End Simulations Using a 250 pC Bunch 79
  - 7.3.1. Particle Tracking Through the Extraction Arc 79
  - 7.3.2. FEL Simulations 80
- 7.4. Start-to-End Simulations Using a 500 pC Bunch 85
  - 7.4.1. Particle Tracking Through the Extraction Arc 85
  - 7.4.2. FEL Simulations 87

7.5. Start-to-End Simulations Using a 1 nC Bunch 88
    7.5.1. Particle Tracking Through the Extraction Arc 88
    7.5.2. FEL Simulations 90
7.6. Conclusions of the Start-to-End Simulations 91

8. Summary and Conclusions 93

A. Calculations of FEL Quantities and CSR Parameters 95
A.1. FEL Quantities 95
A.2. CSR Parameters 98

B. Particle Distributions 99
B.1. Start-to-End Simulations 99
B.2. Gaussian Distributions 108

C. Simplex Optimization Code 111

D. Mismatch Parameter and Mismatch Amplitude 115

E. Mismatch Ellipses 119

F. Extraction Layout 121

List of Figures

1.1. Peak brilliance of different light sources. 3

2.1. Bunch compressor. 8
2.2. The particle's trajectory in an undulator. 9
2.3. The relation between the idealized gain length L_{g0} and the realistic gain length L_g. 15

3.1. Coherent synchrotron radiation and overtaking length. 20
3.2. The evolution of the longitudinal CSR wake field. 21
3.3. The longitudinal CSR wake field along the bunch at different positions. . 22
3.4. Shielding of coherent synchrotron radiation. 23
3.5. Impact from CSR on the longitudinal phase space, the emittance and the energy spread. 24

4.1. 3D-drawing of the FLASH II extension project. 27
4.2. Schematic layout of the FLASH II project. 28
4.3. Beam distribution scheme between FLASH1 and FLASH2. 29
4.4. The photon wave length range in FLASH2. 30

5.1. Flowchart of the downhill simplex algorithm. 36
5.2. Examples of the downhill simplex optimization algorithm. 38
5.3. Flowchart of the optimization procedure for FLASH2. 46

6.1. Magnetic field in the Lambertson septum. 50
6.2. The vertical kickers and the septum. 51
6.3. Achieving zero R_{56} with negative dispersion in the second bend of an arc. 53
6.4. Achieving zero R_{56} with a weak reverse bend. 53
6.5. Horizontal and longitudinal dispersion in the arc. 53
6.6. Course of the second order longitudinal dispersion in FLASH2. 55
6.7. Impact of CSR on the longitudinal phase space and on the current distribution. 56

6.8. Schematic drawings of the longitudinal phase space's modifications due to coherent synchrotron radiation. 57
6.9. Schematic drawings of the horizontal phase space's modifications due to coherent synchrotron radiation. 59
6.10. Emittance growth due to CSR-effects. 61
6.11. Top view of all magnets in the extraction arc. 62
6.12. Optics functions of the FLASH2 extraction arc. 63
6.13. Overall beta functions of FLASH2 starting at the electron gun. 65
6.14. Simulations with 3-σ-ellipses and ±1 % energy deviation without sextupole magnets. 67
6.15. Second order dispersion in the arc without sextupole magnets. 68
6.16. The second order dispersion after the correction with sextupole magnets. . 69
6.17. Simulations with 3-σ-ellipses and ±1 % energy deviation including sextupole magnets. 69
6.18. Course of the beta functions without the proposed third beam line. 71
6.19. 3-σ-ellipses for the beam optics without a beam waist for the proposed third beam line. 71
6.20. Mismatch amplitude for a mismatch parameter $m_p = 1.1$ 73

7.1. Results of the particle tracking simulation through the FLASH2 extraction arc using a 100 pC bunch. 77
7.2. Results of the FEL simulations using a 100 pC bunch. 79
7.3. Results of the particle tracking simulation through the FLASH2 extraction arc using a 250 pC bunch. 81
7.4. Results of the FEL simulations using a 250 pC bunch at 13.5 nm. 82
7.5. Results of the FEL simulations using a 250 pC bunch at 6 nm. 83
7.6. Results of the particle tracking simulation through the FLASH2 extraction arc using a 500 pC bunch. 86
7.7. Results of the FEL simulations using a 500 pC bunch. 87
7.8. Results of the particle tracking simulation through the FLASH2 extraction arc using a 1 nC bunch. 89
7.9. Results of the FEL simulations using a 1 nC bunch. 90

B.1. The 100 pC bunch optimized for the new beam line FLASH2 at the end of the FLASH linac. 100
B.2. The 100 pC bunch at the start of the undulator section in the FLASH2 beam line. 101

B.3. The 250 pC bunch optimized for the new beam line FLASH2 at the end of the FLASH linac. 102
B.4. The 250 pC bunch at the start of the undulator section in the FLASH2 beam line. 103
B.5. The 500 pC bunch optimized for the new beam line FLASH2 at the end of the FLASH linac. 104
B.6. The 500 pC bunch at the start of the undulator section in the FLASH2 beam line. 105
B.7. The 1 nC bunch optimized for the new beam line FLASH2 at the end of the FLASH linac. 106
B.8. The 1 nC bunch at the start of the undulator section in the FLASH2 beam line. 107
B.9. The 250 pC Gaussian distributed bunch as used for the simulations of the CSR induced emittance growth. 109
B.10. The 1 nC Gaussian distributed bunch as used for the simulations of the CSR induced emittance growth. 110

F.1. Top view of the extraction arc for FLASH2. 122

List of Tables

4.1. The electron beam parameters of FLASH2. 31

4.2. The photon beam parameters of FLASH2. 31

6.1. The mismatch parameters for the 3-σ-ellipses simulation in the FLASH2 extraction arc with $\Delta p = 1\,\%$ and including sextupole magnets to close the second order dispersion. 68

6.2. The mismatch parameters for the 3-σ-ellipses simulation in the FLASH2 extraction arc with $\Delta p = 1\,\%$ using the beam optics without a beam waist for the extraction of the proposed third beam line. 70

A.1. Summary of all parameters introduced in chapter 2 for the example case as described above. 98

1. Introduction

The growing interest of the science community and of the industry on research structures in the nano-scale has made it necessary to develop new instruments which are able to resolve these dimensions. In this context, the discovery of synchrotron radiation opened a whole new field of research opportunities and the development of light sources has been advancing continuously ever since.

The first observation of synchrotron light was made 1947 by Elder, Langmuir and Pollock in New York: "During the early operation of a 70-MeV synchrotron in this laboratory, intense visible radiation from the high energy electrons was observed through the glass wall of the accelerating tube."[1] However, in the first years after its discovery, synchrotron light was an unwanted byproduct in electron synchrotrons and storage rings used for particle physics, because the synchrotron light emitted by the particles reduces their kinetic energy and thus it is necessary to accelerate them continuously in order to maintain the required beam energy level over time.

The first experiments using synchrotron light were performed parasitically at synchrotrons or storage rings built for high energy physics. An example was the synchrotron DESY [1] (Deutsches Elektronen Synchrotron, the acronym giving its name to the laboratory DESY in Hamburg, Germany). It was built in the early 1960s to accelerate electrons to an energy of 7.4 GeV which were used for particle physics experiments in the years 1965-1974. The utilization of the synchrotron radiation emitted in the bending magnets started already in the year 1964. Such parasitically used facilities are called the first generation of synchrotron light sources.

A representative of the second generation light sources was BESSY (Berliner Elektronen-Speicherring Gesellschaft für Synchrotronstrahlung [2]) Germany's first dedicated synchrotron radiation source and the name giving machine of the corresponding research institution. Another example is the Synchrotron Radiation Source (SRS) at the Daresbury

---

[1] F. R. Elder, V. L. Langmuir and H. C. Pollock, *Radiation From Electrons Accelerated in a Synchrotron*, Physical Review, Volume 71, Number 1, Page 52, July 1 1948.

Laboratory in Cheshire, England which was the first dedicated synchrotron radiation source (and with this the first second generation synchrotron light source) worldwide [3]. Unlike for the first generation of synchrotron light sources, the beam optics in the second generation machines was optimized for maximum radiation power and beam quality. However, there are not many machines which can be assigned to the second generation because soon it became clear that the third generation matched even better to the demands given by the users.

The third generation of synchrotron light sources adopted the optimized beam parameters from the second generation but the storage ring design was changed such that insertion devices like undulators and wigglers (cf. chapter 2) could be installed in the straight sections between the bending magnets. Those force the electrons with a sequence of alternating dipole magnets on a sinusoidal trajectory and, due to constructive interference is the provided brilliance[2] of an undulator or wiggler orders of magnitudes higher than the brilliance of a single bending magnet. In addition, the emitted light is partially spatial coherent. The development of the peak brilliance is presented in figure 1.1 on the basis of a few selected synchrotron light sources. Examples for third generation light sources are the ALS (Advanced Light Source [4]) at the Lawrence Berkeley National Laboratory in Berkeley and ELETTRA at the Sincrotrone Trieste Laboratory [5] in Trieste, Italy, which both started in 1993. Furthermore, there is the ESRF (European Synchrotron Radiation Facility [6]) on the EPN Science Campus in Grenoble, France and PETRA III (Positron Elektron Tandem Ring Anlage) at DESY, a former particle physics machine which was partially rebuilt and became operational again in 2009 as a third generation synchrotron light source [7].

The fourth generation of synchrotron light sources are the free-electron lasers (FEL) which can cover the wavelength range between $10^{-2}\,\mathrm{m}$ (microwaves e.g. [8]) to $10^{-10}\,\mathrm{m}$ (hard X-rays [9, 10]). Two different designs have to be distinguished: Low gain FELs which require an optical resonator built around a short undulator, typically placed in a storage ring, and high gain single pass FELs which are based on the concept of a linear accelerator followed by an undulator. The first low-gain FEL was built by J. Madey et al. in the high energy physics laboratory of the Stanford University in the year 1976. "The wavelength was 3.417 μm and the average power output was 0.36 W."[3] Thus, the first

---

[2] Specified in units of $photons/(s\ mm^2\ mrad^2\ 0.1\%\ bandwidth)$

[3] J. M. J. Madey et al. *First Operation of a Free-Electron Laser*, Physical Review Letters, Volume 38, Number 16, Page 892, April 18 1977.

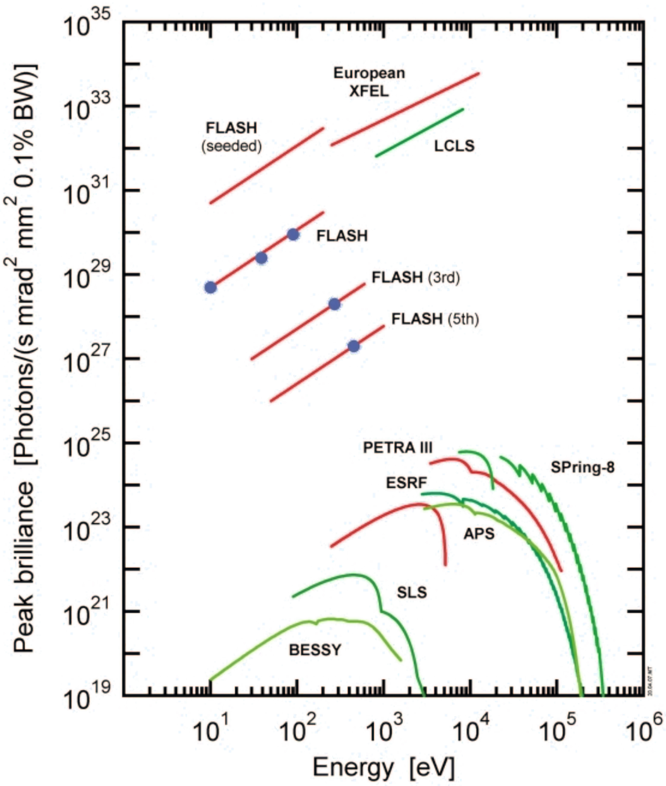

Figure 1.1.: The peak brilliance of different light sources of the third and fourth generation [11]. Light sources operated on the DESY side are depicted in red and the blue dots represent results obtained by measurements. The higher brilliance of the FELs like FLASH, LCLS and XFEL in comparison with the other light sources PETRA III, SPring-8, APS, SLS and BESSY is clearly visible. The lines named FLASH (3rd) and (5th) represent the peak brilliance of the third respectively the fifth harmonic of FLASH.

FEL operated in the infrared range. The ongoing efforts to develop these machines led to shorter and shorter wavelength. The world's first soft X-ray free-electron laser, FLASH (Free-Electron LASer in Hamburg [12]) at DESY, can cover the wavelength range of 4.1-40 nm and it can provide photon pulses with a length of 50-200 fs (FWHM) [13], with a peak brilliance[2] up to 10^{31}. High gain free-electron lasers can provide spatial coherent radiation in forward direction with a brilliance many orders of magnitudes higher than the brilliance of third generation synchrotron light sources.

Short wavelengths as mentioned for FLASH can only be achieved by a high-gain FEL "because here the reflectivity of metals and other mirror coatings drops quickly to zero at normal incidence."[4] That means, it is not possible to build an optical cavity, as required for a low-gain FEL, for wavelengths below 100 nm [14]. High-gain free-electron lasers will be described in more detail in the following chapters. More about low-gain FELs can be found e.g. in [14].

At the time of writing, the FEL FLASH at DESY is equipped with five experimental stations. A second undulator beam line named FLASH2 and a new experimental hall will be built in order to increase the number of photon beam lines. The FLASH linear accelerator will then provide electron bunches for both. The existing photon beam line will remain in operation under the name FLASH1. In addition to the new second beam line (FLASH2), there will be the possibility to install a proposed third beam line whose extraction can be realized at the end of the FLASH2 extraction arc.

This thesis deals with the design of the beam line for the extraction arc between the existing linear accelerator and the new undulator beam line. During the designing process of the beam line layout it was clear that the separation of FLASH1 and FLASH2 has to be realized with a septum deflecting the beam by an angle of 6-7 degree in order to keep further conditions (cf. chapter 4). Considering that the bunches in FLASH2 will be fully compressed at the extraction position - the length of the bunches will be in the μm range and the peak current will be around 2.5 kA - it was expected that coherent synchrotron radiation (cf. chapter 3) affects the beam quality and thus it is necessary to take appropriate measures to minimize these effects. This fact gives a significant restriction to the beam line layout and prevents that a standard design can be used for the extraction. It was thus necessary to find a tailor made solution for this arc which fulfills the above mentioned requirements and also further conditions like closed longitudinal and transverse dispersion (cf. chapter 6).

In the subsequent chapters, I will present a brief introduction to the FEL theory (cf. chapter 2) to explain, for example, the need of small emittances for SASE. Chapter 3 deals with the coherent synchrotron radiation and chapter 4 outlines the extension project at FLASH including the new beam line FLASH2. An introduction to the multi-variable optimization will be given in chapter 5, first in general and then on the basis of the optimization of the extraction arc for FLASH2 and it will be demonstrated how to find

---

[4] M. Dohlus, J. Rossbach, P. Schmüser, *Ultraviolet and Soft X-Ray Free-Electron Lasers*, Page 7, Springer, May 2008.

a solution for a beam line with a large number of variables and constraints. The solution which was found for FLASH2 will be described in detail in chapter 6. In order to verify the usability of this beam line layout, start-to-end simulations were carried out and the results are presented in chapter 7.

2. High-Gain Free-Electron Laser

The aim of this chapter is to give a brief introduction to high-gain FELs including a few formulas of the associated theory. Within the scope of this thesis, it is neither possible nor desired to derive each formula again, but the essential steps will be presented with references to the published literature where one can find a more detailed explanation. The textbook which was mainly used is [14], thus, most of the formulas and explanations in this chapter refer to it.

Unlike a classical LASER where a pump source, which can be another LASER operating at a different wave length, a flash lamp or electrical current, raises electrons, which are bounded to atoms in the so called active medium, to a higher energy level. In "a free-electron laser (...) the role of the active laser medium and the energy pump are both taken over by the relativistic electron beam."[1] For high-gain FELs, the relativistic electron energy is reached by using a linear accelerator (hereinafter called a linac) where electromagnetic fields oscillating in cavities are synchronized such that the electrons are continuously accelerated [15, 16].

The short bunches as required for FEL operation cannot be obtained directly from the electron gun due to the fact that the high charge density in such a short bunch at low beam energy would lead to strong space charge effects destroying the bunches. However, space charge becomes less important with the increasing beam energy [16] and the bunches can be compressed after the first acceleration modules in the linac. A bunch compressor is basically a dispersive section, usually build with four dipole magnets. The length of the particle's trajectory through a bunch compressor depends on its energy and thus bunches with a proper chosen linear energy chirp become shorter. The required energy chirp can be obtained with the electric field in the linac cavities upstream the bunch compressor. Figure 2.1 illustrates the compression process.

---

[1] M. Dohlus, J. Rossbach, P. Schmüser, *Ultraviolet and Soft X-Ray Free-Electron Lasers*, Page 7, Springer, May 2008.

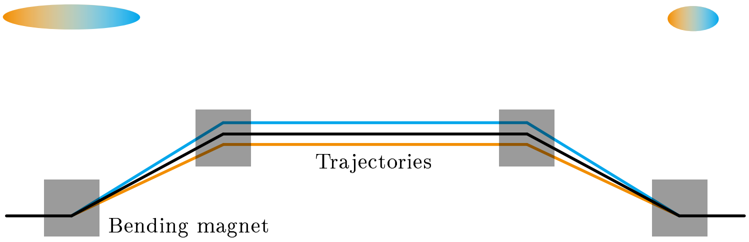

Figure 2.1.: Schematic drawing of a bunch compressor. The linear energy chirp over the bunch, which is necessary for compression, is indicated by different colors, blue for the lower energy at the bunch head and orange for the particles with higher energy at the bunch tail. The corresponding trajectories for the particles with different energies are plotted in the same colors. Due to the different path length of these trajectories, the bunch becomes shorter.

After compression and final acceleration, the bunches are send to the undulator or wiggler at the end of the machine in order to generate the synchrotron radiation. The difference between an undulator and a wiggler will be explained below, but both ”are periodic arrangements of many short dipole magnets of alternating polarity. The electrons move on a sinusoidal orbit through such a magnet (. . .) [and] the overall deflection of the beam is zero.”[2] The magnetic field on the ideal trajectory of the electrons in a planar undulator or wiggler can be described with the following formula [14]:

$$\vec{B} = -B_0 \sin\left(\frac{2\pi}{\lambda_u} z\right) \vec{e}_y, \tag{2.1}$$

with B_0, the maximum magnetic field of the device, λ_u, the period of the alternating magnet structure and z, the longitudinal coordinate of the undulator. The vertical unit vector $\vec{e}_y$ assigns the orientation of the magnetic field. A schematic drawing of an undulator including the trajectory of the particles is presented in figure 2.2.

The properties of an undulator respectively of a wiggler can be described with the dimensionless undulator parameter K:

$$K = \frac{eB_0\lambda_u}{2\pi m_e c}, \tag{2.2}$$

---

[2] M. Dohlus, J. Rossbach, P. Schmüser, *Ultraviolet and Soft X-Ray Free-Electron Lasers*, Page 3, Springer, May 2008.

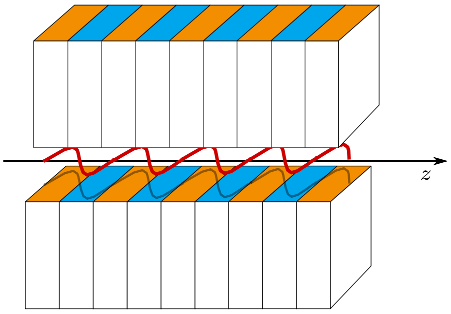

Figure 2.2.: The sinusoidal trajectory of the particles in an undulator is presented as a red colored line and the alternating polarity of the undulator magnets is indicated with the two colors blue and orange.

with the maximum magnetic field B_0 and the period length of the undulator (or wiggler) λ_u as described above. The electron mass is m_e, the elementary charge e and the velocity of light c. With the undulator parameter, the maximum angle of the particle's trajectory can be described as $\alpha_{max} = K/\gamma$ [14]. Since the synchrotron light is emitted in a cone in forward direction with the opening angle of $\alpha_{cone} = 1/\gamma$ [14], the undulator parameter describes also the overlap of the synchrotron radiation emitted at different positions of the particle's trajectory in the undulator. A small undulator parameter ($K < 1$) means that there is a large overlap of the emitted radiation which describes, in turn, the characteristics of an undulator. Thus, large undulator parameters ($K > 1$) stand for wigglers. The different overlaps have an influence on the spectrum of the devices: The smaller the undulator parameter, the more are the higher harmonics of the synchrotron radiation suppressed and the more dominates the first harmonic. The wavelength of the first harmonic can be calculated with the following formula:

$$\lambda_l = \frac{\lambda_u}{2\,\gamma_r^2}\left(1 + \frac{K^2}{2} + \gamma_r^2\Theta^2\right), \tag{2.3}$$

with the Lorenz factor γ_r and the vertical angle between the observer position and the undulator axes Θ. This formula shows that the wavelength of the undulator or wiggler radiation can be tuned by changing the energy of the particles or by changing the undulator parameter. The latter can be realized in practice by changing the gap between the upper and the lower magnets which changes the magnetic field B_0 and thus K.

Two modes of operation are possible for a high-gain FEL, SASE (self-amplified stimulated emission) and seeding which implies the use of an external seed. "The most intuitive explanation of SASE is that the electrons produce spontaneous undulator radiation in the first section of a long undulator magnet which then serves as seed radiation in the main part of the undulator."[3] In the following, I will describe briefly the theory of high-gain SASE FELs. It was mentioned in the introduction that, in absence of appropriate mirrors, it is not possible to build an optical cavity for wave lengths below 100 μm. "Thus the light amplification must be achieved in a single pass through a very long undulator magnet. (...) The amplitude of the light wave grows considerably during the motion through the undulator. This growth and the development of a microbunch structure at the level of the optical wavelength are the essential new features of the high-gain FEL theory."[4] The microbunching effect "is based on the following principle: electrons losing energy to the light wave travel on a sinusoidal trajectory of larger amplitude than electrons gaining energy from the light wave (...). The result is a modulation of the longitudinal velocity which eventually leads to a concentration of the electrons in slices which are shorter than the optical wavelength λ_l. These microbunches are close to the positions where maximum energy transfer to the light wave can happen (...). The particles within a microbunch radiate like a single particle of high charge. The resulting strong radiation field enhances the microbunching even further and leads to an exponential growth of the radiation power."[4] In addition, this effect leads to transverse coherent radiation in forward direction in SASE FELs.

I will start this theoretical consideration with the one dimensional high-gain FEL theory where e.g. the transverse electromagnetic field components and the transverse structures of the electron bunches are neglected and, in addition, the bunches are assumed to be infinitely long. In this case, the characteristics of a high-gain FEL can be described with a set of four coupled first-order equations which are presented in the equations 2.4-2.7 [14].

$$\frac{d\psi_n}{dz} = 2k_u\eta_n. \qquad n = 1 \dots N \tag{2.4}$$

$$\frac{d\eta_n}{dz} = -\frac{e}{m_e c^2 \gamma_r}\Re\left\{\left(\frac{\hat{K}\tilde{E}_x}{2\gamma_r} - \frac{i\mu_0 c^2}{\omega_l}\cdot\tilde{j}_1\right)e^{i\psi_n}\right\} \tag{2.5}$$

---

[3] http://photon-science.desy.de, June 2013

[4] M. Dohlus, J. Rossbach, P. Schmüser, *Ultraviolet and Soft X-Ray Free-Electron Lasers*, Page 38, Springer, May 2008.

$$\tilde{j}_1 = j_0 \frac{2}{N} \sum_{n=1}^{N} e^{-i\psi_n} \tag{2.6}$$

$$\frac{d\tilde{E}_x}{dz} = -\frac{\mu_0 c \hat{K}}{4\gamma_r} \cdot \tilde{j}_1. \tag{2.7}$$

The individual equations and their components will be explained in the following. First of all, the last three equations include symbols labeled with a tilde which indicates that these quantities are given as complex functions. The first three equations include the index n which identifies the n^{th} out of N electrons in a bunch slice.

Equation 2.4 shows the derivative of the ponderomotive phase ψ_n with respect to the longitudinal position in the undulator z. It describes the phase relation between the light wave and the sinusoidal trajectory of the n^{th} electron in the undulator. A phase of $\psi_n = 0$ indicates the ideal relation for the energy transfer from the electron to the light wave and the counterpart $\psi_n = \pm\pi$ stands for the optimum energy transfer from the light wave to the electron. A ponderomotive phase of $\psi_n = \pm\pi/2$ is corresponding to a vanishing energy exchange. Furthermore, the wavenumber of the sinusoidal electron trajectory in the undulator $k_u = 2\pi/\lambda_u$ is used with the undulator period length λ_u. The relative energy deviation η_n of the n^{th} electron can be calculated as shown in the following formula using the Lorenz factor γ_r corresponding to the resonant energy of the undulator and the Lorenz factor γ_n corresponding to the related electron [14]:

$$\eta_n = (\gamma_n - \gamma_r)/\gamma_r \qquad \text{for} \qquad \eta \ll 1. \tag{2.8}$$

The second equation of the set (equation 2.5), describing the derivative of the relative energy deviation of the n^{th} electron η_n with respect to the longitudinal coordinate z depends on the elementary charge e, the electron mass m_e, the velocity of light c and the magnetic constant μ_0. In addition, there is the modified undulator parameter $\hat{K}$ which takes the longitudinal oscillation of the electrons in the undulator into account and which can be calculated as follows [14]:

$$\hat{K} = K \left[J_0 \left(\frac{K^2}{4 + 2K^2} \right) - J_1 \left(\frac{K^2}{4 + 2K^2} \right) \right], \tag{2.9}$$

with the Bessel functions J_0 and J_1. The unmodified undulator parameter K was defined before in equation 2.2. The angular frequency of the light wave is described with ω_l and

$\tilde{j}_1$ is the amplitude of the current density modulation $\tilde{j}(\psi, z) = j_0 + \tilde{j}_1(z)\exp(i\psi)$. $\tilde{E}_x$ is the transverse amplitude of the electromagnetic wave. All further quantities were described above for equation 2.4.

The current density modulation amplitude $\tilde{j}_1$ was mentioned just before and is described in equation 2.6. It depends on the number of electrons per bunch slice N and on the DC current density j_0.

The last equation of the set, equation 2.7, presents the derivative of the horizontal electromagnetic wave amplitude $\tilde{E}_x$ with respect to the longitudinal position z. All quantities used in this equation was explained in the last paragraphs. This formula shows clearly that the microbunching effect described by the current density modulation amplitude $\tilde{j}_1$ has a decisive influence on the growth of the light field's intensity in a high-gain FEL.

"The main physics of the high-gain FEL is contained in the coupled first-order equations [as described above] (...), but unfortunately these equations possess no analytical solution. If we make the additional assumption that the periodic density modulation remains small it is possible to eliminate the quantities ψ_n and η_n characterizing the particle dynamics in the bunch and derive a differential equation containing only the electric field amplitude $\tilde{E}_x(z)$ of the light wave. This equation has the great advantage that it can be solved analytically."[5] The third-order equation is presented in equation 2.10 [14] and will be discussed in the following.

$$\frac{\tilde{E}_x'''}{\Gamma^3} + 2i\frac{\eta}{\rho_{\mathrm{FEL}}}\frac{\tilde{E}_x''}{\Gamma^2} + \left(\frac{k_p^2}{\Gamma^2} - \left(\frac{\eta}{\rho_{\mathrm{FEL}}}\right)^2\right)\frac{\tilde{E}_x'}{\Gamma} - i\tilde{E}_x = 0 \tag{2.10}$$

In this equation, $\tilde{E}_x'$ indicates the derivative of the horizontal component of the electromagnetic wave with respect to the longitudinal position z and, correspondingly, $\tilde{E}_x''$ and $\tilde{E}_x'''$ indicate the second respectively the third derivative. Γ represents the gain parameter which will be used below to calculate the power gain length of an idealized FEL [14]:

$$\Gamma = \left[\frac{\mu_0 \hat{K}^2 e^2 k_u n_e}{4\gamma_r^3 m_e}\right]^{1/3}, \tag{2.11}$$

---

[5] M. Dohlus, J. Rossbach, P. Schmüser, *Ultraviolet and Soft X-Ray Free-Electron Lasers*, Page 49, Springer, May 2008.

with the electron density in the bunch slices n_e. A further new quantity in equation 2.10 is the space charge parameter [14]:

$$k_p = \sqrt{\frac{2\lambda_l}{\lambda_u}} \cdot \frac{\omega_p^*}{c} \tag{2.12}$$

that depends on the plasma frequency [14]:

$$\omega_p^* = \sqrt{\frac{n_e e^2}{\gamma_r \epsilon_0 m_e}}, \tag{2.13}$$

with the vacuum permittivity ϵ_0. The gain parameter Γ and the space charge parameter k_p have both the dimension of an inverse length.

The last new quantity in equation 2.10 is the dimensionless FEL parameter [14]:

$$\rho_{\mathrm{FEL}} = \frac{\Gamma}{2k_u}. \tag{2.14}$$

If one uses the "idealized [power] gain length of the one-dimensional theory [L_{g0},] assuming a mono-energetic beam and neglecting space charge forces"[6] the FEL parameter can be written as [14]:

$$\rho_{\mathrm{FEL}} = \frac{1}{4\pi\sqrt{3}} \cdot \frac{\lambda_u}{L_{\mathrm{g0}}}, \tag{2.15}$$

with

$$L_{\mathrm{g0}} = 1/(\sqrt{3}\Gamma). \tag{2.16}$$

The FEL parameter will be used later again to calculate or estimate further parameters. All quantities presented above are computed for FLASH2 in appendix A.

Using the ansatz $\tilde{E}_x(z) = Ae^{\alpha z}$ to solve the third order equation 2.10 one obtains, for adequately large z, the power of the light wave grows as [14]

$$P(z) \propto e^{\sqrt{3}\Gamma z} \equiv e^{z/L_{\mathrm{g0}}}. \tag{2.17}$$

Equation 2.17 shows how the photon beam power develops traveling through the undulator, however, this "exponential growth cannot continue indefinitely because the beam

---

[6] M. Dohlus, J. Rossbach, P. Schmüser, *Ultraviolet and Soft X-Ray Free-Electron Lasers*, Page 55, Springer, May 2008.

energy decreases due to the energy loss by radiation and the modulated current density $\tilde{j}_1$ becomes eventually comparable in magnitude to the dc current density j_0 [(fully developed microbunching)]. Moreover, the particles begin to move into the phase space region where energy is taken out of the light wave."[7] Thus the photon beam power will reach a point of saturation[8]. It turns out that the FEL power at saturation can be described in the one-dimensional theory with the following approximation [14]:

$$P_{\text{sat}} \approx \rho_{\text{FEL}}\, P_{\text{Beam}} \qquad \text{with} \qquad P_{\text{Beam}} = \frac{\gamma_r m_e c^2 I_0}{e}. \tag{2.18}$$

In the following we consider additional effects going beyond the ideal situation as described above were we used the one-dimensional FEL theory for a mono energetic beam without space charge. It turns out that the realistic gain length L_{g} of an FEL is then longer than the idealized gain length L_{g0} derived before. For this example the impact from finite beam energy spread, from space charge and from the magnitude of the transverse emittance on the gain length and saturation power will be discussed briefly below. For this considerations, the particular bunch and machine parameters from FLASH2 will be used to estimate their impact on the gain length.

These effects are exemplified in figure 2.3, where simulation results are presented showing the relation between the idealized gain length L_{g0} and the realistic gain length L_{g} as a function of the relative energy deviation of the electrons in units of the FEL parameter η/ρ_{FEL} for three different values of the space charge parameter k_p in units of the gain parameter Γ, respectively for three different values of the energy spread parameter σ_η in units of the FEL parameter ρ_{FEL}. In both simulations, the respective other parameter was set to zero.[9] Taking the values of the FLASH2 undulator beam line for a 1 GeV beam with 0.5 MeV rms energy spread and a undulator parameter of 1, one obtains $k_p \approx 0.19\,\Gamma$ and $\sigma_\eta \approx 0.20\,\rho_{\text{FEL}}$ (cf. appendix A). Comparing these values with the results from the simulations presented in figure 2.3 it becomes evident that the impact on the FEL gain length from energy spread is larger than the impact from space charge. For this example, the impact from space charge increases the gain length by approximately 1 % and the energy spread causes an extension of the gain length by approximately 10 %. For this reason, the energy spread of the bunches used for SASE has to be kept small.

---

[7] M. Dohlus, J. Rossbach, P. Schmüser, *Ultraviolet and Soft X-Ray Free-Electron Lasers*, Page 68, Springer, May 2008.

[8] The regime of FEL saturation can be studied using a numerical solution for the coupled first-order differential equations 2.4-2.7 [14].

[9] In a SASE FEL, the relative energy deviation will level off at the peak position of the respective curve as presented in figure 2.3 [14, 17].

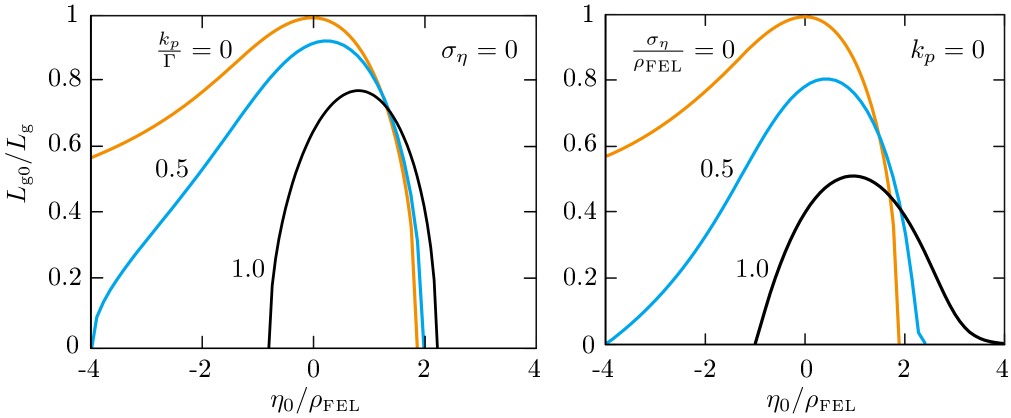

Figure 2.3.: The relation between idealized gain length L_{g0} and the realistic gain length L_{g} as a function of the relative energy deviation η in units of the FEL parameter ρ_{FEL} for three different space charge parameter values (on the left hand side) and for three different energy spreads (on the right hand side) (Courtesy of M. Dohlus).

In the next step, two different requirements on the maximum emittance size will be considered in order to ensure satisfactory FEL operation. The first restriction is given by the fact that a large electron beam emittance entails also a large beam divergence at positions with small beta functions. The divergence has in turn an impact on the transverse and longitudinal velocity of the electrons which finally has the same effect on the FEL operation like an energy spread [14]. An upper limit for the emittance restricted by this effect can be derived and the result is presented in the following inequation, depending on the resonant energy γ_r and on the average beta function in the undulator section β_{av} [14]:

$$\epsilon_x < \frac{\beta_{\mathrm{av}}}{2\sqrt{2}\gamma_r^2}\,\rho_{\mathrm{FEL}}. \tag{2.19}$$

This applies only to the plane where the transverse deflection of the electron beam takes place caused by the alternating dipoles of the undulator. At this point, it has to be mentioned that it is not an appropriate solution to enlarge β_{av} in order to allow larger emittances because this would lead to a smaller electron density n_e and thus to a larger gain length L_{g0} (cf. equation 2.11 - 2.16). However, it is possible to derive an optimum beta function β_{opt} balancing the effects on FEL operation from the electron density and the transverse velocity variations as published by Saldin et al. [18].

The second restriction on the emittance comes from the necessary overlap between the electron beam and the light wave. The following inequation describing the emittance limit given by this condition is derived in [14]:

$$\epsilon_x \leq \frac{\lambda_l}{4\pi} \tag{2.20}$$

For FLASH2, inequation 2.19 necessitates a physical emittance below 1.4 nm rad at a energy of 1 GeV and inequation 2.20 a maximum emittance around 0.5 nm rad in the case of the corresponding photon wavelength of 6.1 nm (cf. appendix A). Comparing this values with the foreseen physical emittance of the new beam line $\epsilon_x \approx \epsilon_y \approx 0.5\,\mathrm{nm\,rad}$ at 1 GeV (normalized emittance $\epsilon_n \approx 1\,\mu\mathrm{m\,rad}$), it becomes evident that a further emittance growth in the extraction arc and in the matching section upstream the undulators must be avoided as good as possible in order to obtain the desired radiation properties.

In the last contribution of this chapter, I will present a further and more precise approximation of the FEL gain length and saturation power than described above. M. Xie published a parametrization method for the gain length [19] where he comes to the conclusion that the real gain length of an FEL can be described in relation to the idealized gain length L_{g0} as follows:

$$L_{\mathrm{g,xie}} = L_{\mathrm{g0}}\,(1 + \Lambda), \tag{2.21}$$

with the correction term Λ depending on L_{g0}, σ_η, λ_l, the average beta function in the undulator and the rms radial width of the beam. The correction term for FLASH2 is in the range of $\Lambda = 0.165$ (for a 1 GeV electron beam energy, 0.5 MeV rms energy spread, an undulator parameter of 1, an average beta function of 6 m and a physical emittance of 0.5 nm rad, cf. appendix A), thus, the real gain length is about 16.5 % longer than the ideal gain length as calculated with the one-dimensional FEL theory.

The calculation of the saturation power including energy spread, emittance, space charge, finite bunch length and radiation diffraction is described in [14] and [20]. They derived an approximation of the saturation power P_{sat} depending on the FEL parameter ρ_{FEL}, the electron beam power P_{Beam} and the ratio of the idealized and the realistic gain length:

$$P_{\text{sat, xie}} \approx 1.6\ \rho_{\mathrm{FEL}}\ P_{\mathrm{Beam}} \left(\frac{L_{\mathrm{g0}}}{L_{\mathrm{g,xie}}}\right)^2 \tag{2.22}$$

Using the same parameters, the saturation length in FLASH2 is $P_{\text{sat, xie}} \approx 4.7\,\mathrm{GW}$. The related calculations can be found in appendix A.

The theoretical considerations, especially those taking into account the effects which go beyond the one-dimensional theory, lead to the conclusion that it is important to conserve the emittance size during the passage of the extraction arc as good as possible and to mitigate the increase of the energy spread. In chapter 6, describing the beam line layout, these two parameters will play an important role.

3. Coherent Synchrotron Radiation

The consideration of coherent synchrotron radiation (CSR) and its effects in developing the extraction arc for FLASH2 was mandatory in order to be able to obtain a sufficient electron beam quality for FEL operation. The consequences resulting from these deliberations led to a major influence on the final beam line layout (cf. chapter 6). This chapter will give a brief introduction to CSR and its impact on the electron bunches, especially on the horizontal emittance and on the energy spread. In order not to exceed the framework of this thesis, I will present example calculations for typical parameter sets to introduce the basic effects and refer, where applicable, to the related publications.

I will explain the CSR effects on the basis of a short, Gaussian distributed bunch with a charge of 100 pC, a one-sigma length of 5 μm yielding a peak current of 2.5 kA and an energy of 1 GeV. These parameters are comparable with those in the FLASH2 start-to-end simulations (cf. appendix B) and the bending magnet used for the example has the same parameters as the septum used for the FLASH2 extraction (cf. chapter 6). The 100 pC bunch is the shortest typically used in FLASH and the septum has the smallest bending radius in the extraction arc, thus, the largest effects are expected with this combination.

"If short bunches travel along trajectories with small bending radii a simple geometrical condition permits strong longitudinal and radial wake fields to act on the bunch: electromagnetic fields emitted by a particle can "overtake" on a shorter straight trajectory and interact with particles which are ahead in the bunch. The bunch then starts to radiate coherently"[1]. Figure 3.1 represents this situation.

In order to get a prediction about the expected coherence of the emitted radiation, one can regard the ratio of the bunch length σ_z and $\sigma_0 = \rho/\gamma^3$ with the bending radius ρ and the Lorentz factor γ [21]. A ratio below 1 indicates a fully coherent radiation, a ratio between 1 and 10^7 a coherent and energy independent radiation and a ratio above 10^7 stands for incoherent radiation [17, 21]. For the example with the 100 pC bunch in the

---

[1] M. Dohlus, T. Limberg, *Emittance growth due to wake fields on curved bunch trajectories*, Nucl. Instr. Meth. A 393 (1997) 494-499.

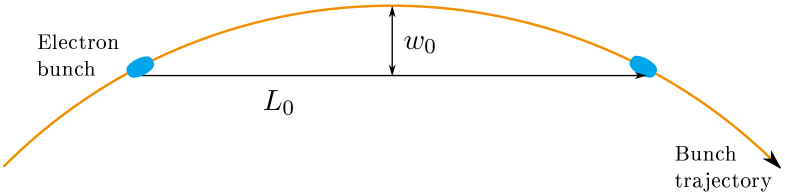

Figure 3.1.: The curved bunch trajectory in a bending magnet is longer than the direct path, thus, synchrotron radiation emitted from particles in the bunch tail can overtake and has then an impact on the electrons in the bunch head. The overtaking lengths L_0 and the distance between the direct and the electron trajectory w_0 are marked in the plot.

septum, the ratio is about $\sigma_z/\sigma_0 \approx 4200$ and thus in the region of coherent and energy independent radiation.

The overtaking length L_0 as presented in figure 3.1 is a measure for the interaction length inside a bending magnet and can be calculated using the one-sigma length of the bunch σ_z and the bending radius ρ [22]:

$$L_0 = \sqrt[3]{24\,\rho^2\sigma_z}. \tag{3.1}$$

The distance between the direct trajectory and the trajectory of the electron bunches, $w_0 = \sqrt[3]{\rho\,\sigma_z^2}$ [22], is important for the shielding of the coherent synchrotron radiation as it will be discussed later on. For the example as described above, the overtaking length is $L_0 \approx 0.21\,\mathrm{m}$ and the distance between the trajectories is $w_0 \approx 0.6\,\mathrm{mm}$ (cf. appendix A).

One can observe the wake field from CSR as two independent parts, the longitudinal and the transverse wake. Since the amplitude, and with it the effect on the bunch, of the transverse wake is small in comparison with the longitudinal wake [21, 22], I will only describe the effects caused by the latter one in this chapter. The steady state field in the center of the bunch and the decay of the longitudinal wake field downstream a bending magnet can be approximated on the basis of the overtaking length L_0 and the peak current I_0 [17]:

$$E_c \approx \frac{1}{\pi}\frac{Z_0\,I_0}{L_0} \tag{3.2}$$

$$E_{\mathrm{dec}}(d) \approx -\frac{1}{2\pi}\frac{Z_0\,I_0}{0.5\,L_0 + d} \tag{3.3}$$

with $Z_0 = \sqrt{\mu_0/\epsilon_0}$ and the distance between the end of the bending magnet and the calculated position of the decaying wake field d. For the 100 pC bunch in the septum, as described in the example above, the approximated steady state field is $E_c = -1.43\,\mathrm{MV/m}$ (cf. appendix A). Following these approximations, the transverse wake field is reduced to 10 % of its maximum value at a position about 1 m downstream from the septum. This fact will be used in section 6.3.

Figure 3.2 shows the course of the longitudinal CSR field field amplitude in the bunch center. The approximated steady state field in the bend and the approximated decay in the following drift section (both as a blue line), as well as the data from a CSRtrack[2] simulation (orange line) are presented. It is apparent that the approximation is in good agreement with the simulation. The maximum absolute field is at a position of about $1\,L_0$ downstream from the septum entrance.

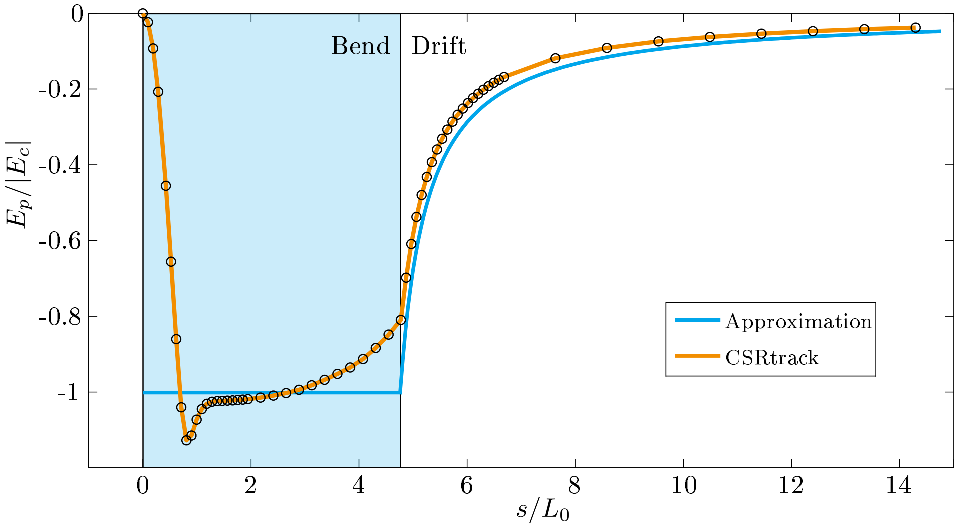

Figure 3.2.: The course of the longitudinal CSR wake field of a 100 pC bunch in the septum (light-blue rectangle) and in the following drift section. Presented are the results obtained by a CSRtrack simulation (orange) and the approximated course of the longitudinal CSR wake field (blue). The field strength is normalized to the absolute value of the approximated steady state field $|E_c|$ and the longitudinal position is normalized to the overtaking length L_0.

Figure 3.3 shows the field strength along the bunch at different positions in the septum (plot a) and in the following drift section (plot b). The positions are specified in units of the overtaking length L_0 in order to be able to compare these positions with those in figure 3.2. The abscissa of both plots, showing the value of the transverse wake field, are normalized to the absolute value of the steady state field $|E_c|$ and the ordinates of both

---

[2] These simulations were carried out using the projected force model.

plots, showing the positions in the bunch, are normalized to its one-sigma length. These plots were obtained with the data of the 100pC bunch as used for the examples.

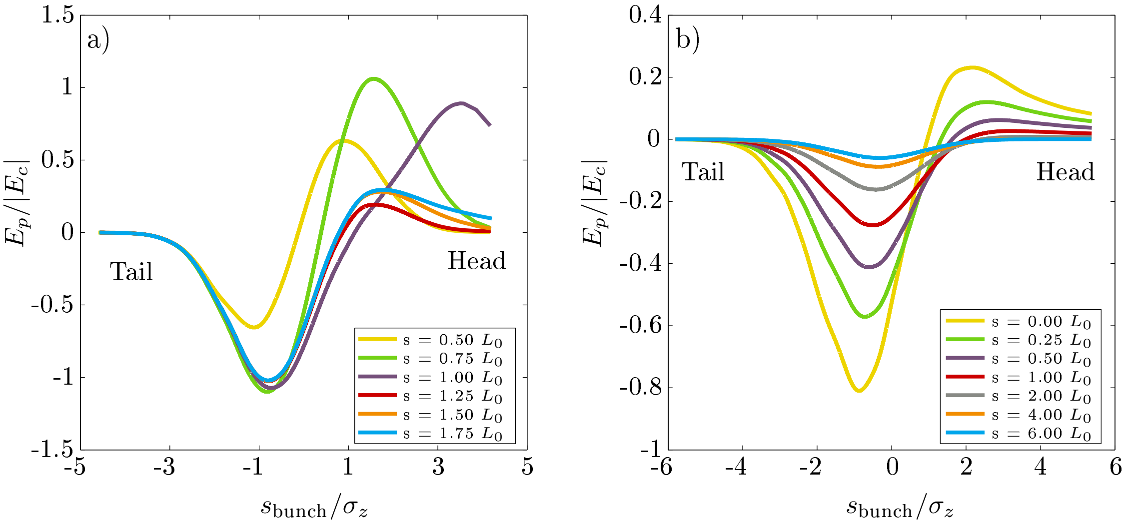

Figure 3.3.: The longitudinal CSR wake field along the bunch at different positions in the septum (plot a) and in the following drift section (plot b). The field strength is normalized to $|E_c|$ and the positions in the bunch are normalized to its one-sigma length. The differently colored lines represent the field at different longitudinal positions in units of the overtaking length L_0 measured from the start of the septum (plot a) respectively from the start of the following drift section (plot b).

The plots in figure 3.3 show that the energy of the electrons in the bunch center will be reduced and the energy in the bunch head will be increased. Furthermore, it is evident that the impact form CSR on the bunch is not terminated with the end of the bending magnet, thus the modification of the bunch in the following drift section has to be taken into account as well. More about this interaction will be presented in the chapter 6.

In figure 3.1, the distance w_0 between the trajectory of the electron bunches in a bending magnet and the direct trajectory was introduced and it was mentioned that this parameter is of interest for CSR shielding. If the photons from CSR are prevented from traveling along the direct trajectory, the effects described above will not occur. In order to achieve this, the distance between the vacuum chamber (or any other shield) and the trajectory of the electrons has to be in the range of w_0 or smaller. However, in the case of the 100 pC bunch in the septum, w_0 is about 0.6 mm (cf. appendix A) and thus much too small to be realized with the vacuum chamber.

If it is not possible to shield the coherent synchrotron radiation, it is necessary to study also the mirror charges in the vacuum chamber and their impact on the bunch. In figure 3.4, the results from two simulations are presented, one including the mirror charges from a cylindrical vacuum chamber with a radius of $r = 20\,\mathrm{mm}$, in accordance with the vacuum chamber in FLASH2, and a second simulation without mirror charges.

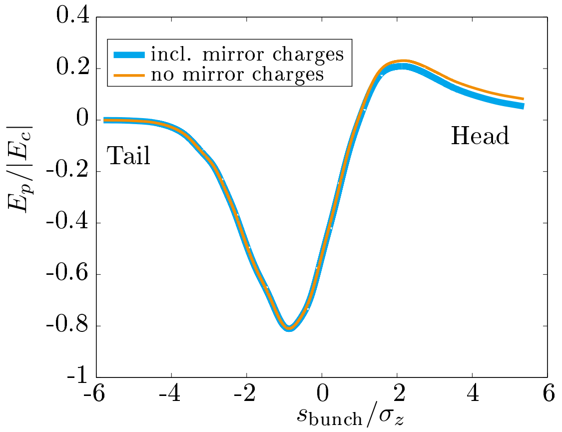

Figure 3.4.: This plot shows the longitudinal CSR wake field along the bunch at the end of the bending magnet (cf. with the yellow line in figure 3.3, plot b). One simulation was carried out including mirror charges from a vacuum chamber with 20 mm radius and the second simulation without these effects. These plots show that there is only a small deviation in the head of the bunch.

The simulation results show that the impact from mirror charges on the bunch is small due to the large distance of 20 mm between the electrons and the vacuum chamber. For this reason, these effects will not be considered in the following simulations as presented in chapter 6 and chapter 7.

The plots in figure 3.5 show the longitudinal phase space (plots a), the slice emittance along the bunch (plots b) and the slice energy spread along the bunch (plots c) of the example bunch before (plots on the left hand side in blue) and after (plots on the right hand side in orange) the impact of the CSR effects. The final position was chosen 1 m behind the septum magnet, which corresponds to about 5 times L_0, where the transverse wake field is decayed at this position to about 10 % of its initial value.

The modification of the particle distribution in the longitudinal phase space is evident and the above mentioned energy loss in the bunch center, as well as the increased energy

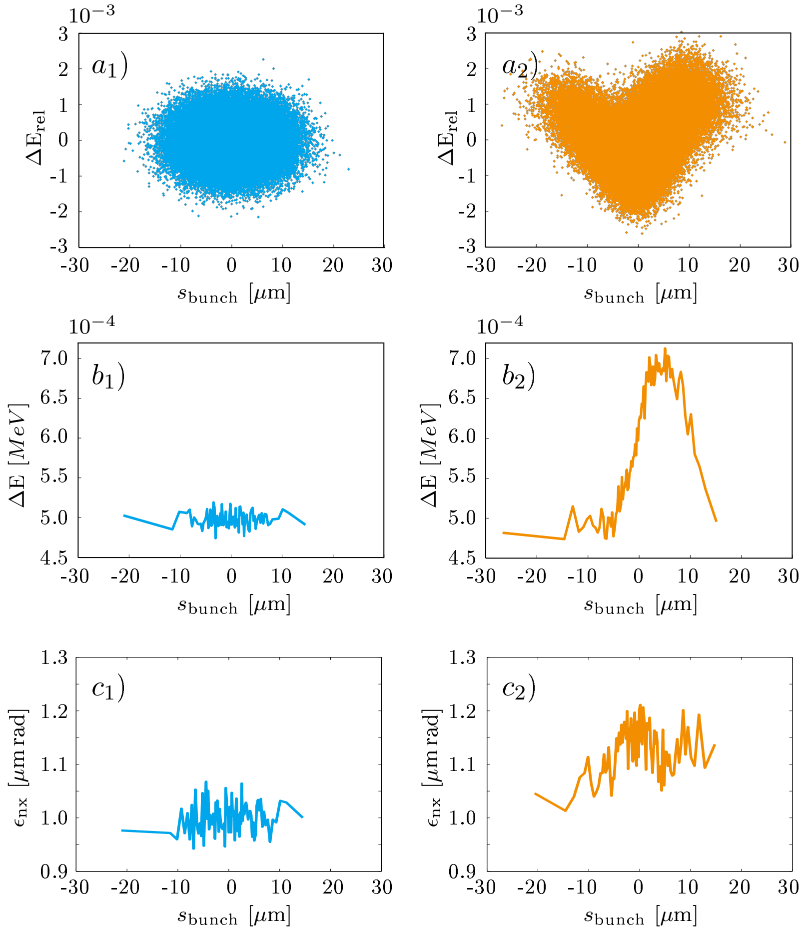

Figure 3.5.: These plots show the impact from CSR effects on the longitudinal phase space (plots a_1 and a_2), the horizontal emittance (plots b_1 and b_2) and the energy spread (plots c_1 and c_2). The blue plots on the left hand side represent the situation before the septum and the orange plots on the right hand side the situation 1 m (about 5 times L_0) behind the septum. At this position, the longitudinal wake field is decayed to about 10 % of its initial value.

in the bunch head is clearly perceptible. The horizontal slice energy spread becomes also larger in the bunch center and in the bunch head which is "caused by two effects: nonlinearly varying CSR forces for different transverse positions and directions of particles in the same slice on one hand and different longitudinal positions of particles that are initially (and approximately finally) in the same slice on the other."[3] Before discussing the emittance growth due to CSR effects, it has to be mentioned that the additional particle offset caused by dispersion at the position downstream the bending magnet was subtracted before the emittance evaluation was carried out. The growth of the horizontal slice emittance is in the range of about 10 %, however, the projected emittance doubles. This is due to the modified energy in the bunch and the resulting mismatch at the corresponding positions in the bunch. Further simulations concerning the impact from CSR on the slice emittance are presented in section 6.4.

The results presented in this chapter showed clearly that the CSR effects can lead to an increased transverse emittance and energy spread. Particular attention has to be paid to these effects during the designing process of the extraction arc in order to mitigate them.

Two possibilities to reduce CSR effects on emittance growth will be presented briefly, the $-I$ transfer matrix and the defined courses of the horizontal Twiss functions in the bending magnets. Required for the first option is an extraction arc with four bending magnets, symmetrically arranged to their midpoint and with a -I transport matrix between the two bends in the middle. This layout is used e.g. at the FEL FERMI@Elettra for the spreader, which is comparable with the extraction arc, and "this arrangement in horizontal plane provides a basis for a compensation of emittance excitation due to coherent synchrotron radiation in the spreader's bending magnets" [4]. The specified transfer matrix in the middle of the arc leads to the situation that the transverse displacement of the particles caused by the first two bends will be canceled in the last two bends.

The second solution is based on the fact "that slice emittance growth (...) can depend

---

[3] M. Dohlus, T. Limberg, *Impact of Optics on CSR-related Emittance Growth in Bunch Compressor Chicanes*, Proceedings of 2005 Particle Accelerator Conference, Knoxville, Tennessee.

[4] A. Zholents1 et al., *Spreader Design for FERMI@Elettra Free-Electron Laser*, LBNL-62345, CBP Tech Note-370, January 18, 2007.

heavily on the initial beam parameters chosen."[5] This paper deals with bunch compressors but the described CSR effects mitigation technique can also be applied on the extraction arc for the FLASH2 beam line. This approach requires a horizontal beam waist about in the center of the respective bending magnets. The decision which of the two CSR mitigation techniques will be used for the FLASH2 extraction arc will be presented and explained in the following.

---

[5] M. Dohlus, A. Kabel, T.Limberg, *Optimal beam optics in the TTF-FEL bunch compression sections: Minimizing the emittance growth*, Proceedings of the 1999 Particle Accelerator Conference, New York, 1999

4. FLASH II Project

The extension of FLASH[1] [23], consisting of the second undulator beam line with additional user stations, became necessary as the existing machine was overbooked most recently by a factor of 4 [24]. The SASE photon beam parameters from FLASH2 will be the same as in the existing beam line and there will be the possibility to operate the new beam line in seeding mode. Variable gap undulators in FLASH2 will make it possible to

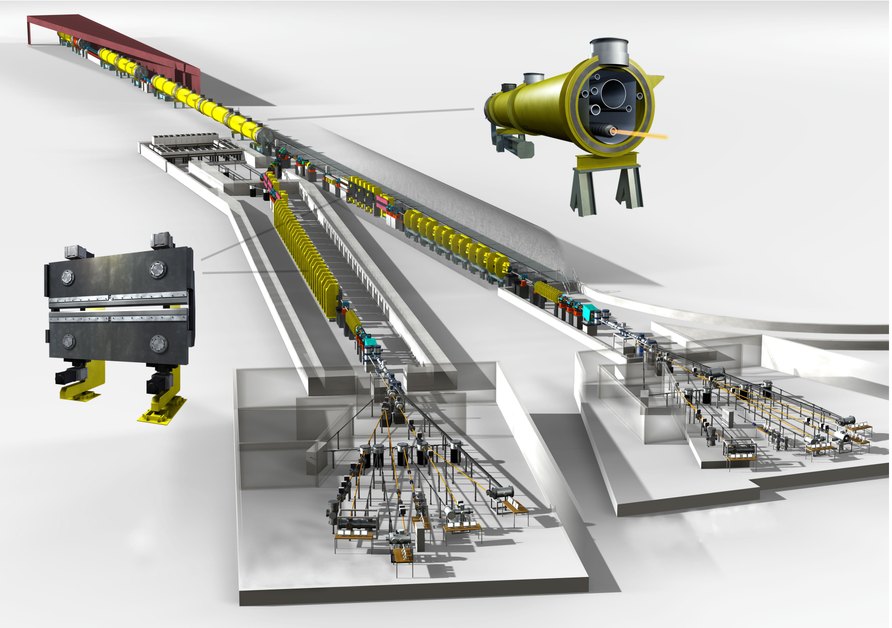

Figure 4.1.: Planning sketch of the FLASH II extension project including the linac, the two undulator beam lines FLASH1 (on the right hand side) and FLASH2 (on the left hand side) and the corresponding experimental stations [25]. A sectional drawing of an accelerating module and an extra sketch of an FLASH2 variable gap undulator are shown next to the beam line tunnels.

---

[1] To avoid confusion, a few names and designations have to be mentioned and explained: The existing FEL is operated so far under the name FLASH and this name will remain after the extension is completed for the entire machine including both beam lines. The extension project itself is named FLASH II with a roman numeral and the undulator beam lines will be distinguished, as mentioned in chapter 1, with Arabic numerals like FLASH1 (the existing undulator beam line) and FLASH2 (the new beam line).

change the photon wavelength without changing the electron's energy. Two independent lasers at the electron gun cathode will allow, within limits, to serve different numbers of bunches per bunch train, different repetition rates for FLASH1 respectively for FLASH2 and different bunch charges for the two beam lines. Furthermore, it will be possible to apply different RF (Radio frequency) settings on the bunches for the different beam lines by means of accordingly modified RF pulses [26]. This allows to provide different bunch shapes in the longitudinal phase space for FLASH1 respectively for FLASH2 which is necessary when different bunch charges are demanded or if FLASH2 is in seeding operation. Due to the different layouts of the beam lines downstream the linac, slightly different compression schemes for FLASH1 and FLASH2 are also necessary even for bunches with the same charge used for SASE.

The extension project comprises a minor modification of the existing beam line in the separation area, the extraction arc which will transport the electrons from the extraction position to the undulators with an overall angle of 12 degree in reference to the existing machine and the undulator beam line housed in a new tunnel. In addition, there will be a new hall for experimental stations. A schematic layout of the linac and the two future beam lines is presented in figure 4.2.

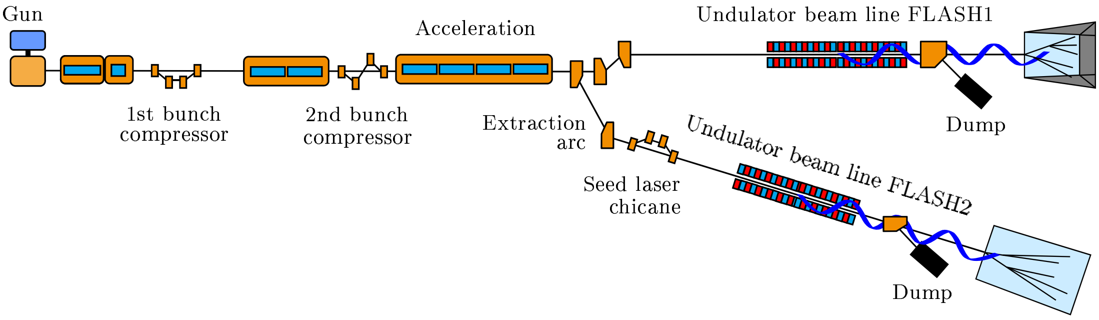

Figure 4.2.: Schematic layout of the extension project of FLASH including the linac, the bunch compressors and the undulator beam line FLASH1 of the existing FEL as well all the extraction arc and the new undulator beam line FLASH2 [23].

The separation of the two beam lines will be realized with fast kickers and a septum because that allows a fast switching between FLASH1 and FLASH2. The kickers are fast enough to deliver bunches to both beam lines with a 10 Hz repetition rate [23, 26]. A time gap of at most 50 μs between the bunch trains for the first and the second beam line is sufficient to raise the magnetic field in the kickers. The total length of both bunch trains plus the time gap has to be smaller than 800 μs which is the maximum length of the RF pulse in the cavities. A scheme showing the bunch trains and their chronology is presented in figure 4.3.

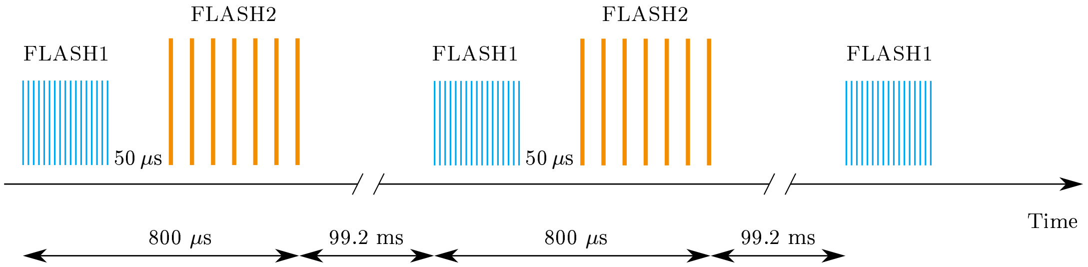

Figure 4.3.: The beam distribution scheme for the two beam lines FLASH1 and FLASH2. Two bunch trains, created with two independent lasers, with a maximum total length of 800 μs and a gap of at most 50 μs are distributed to both beam lines with a 10 Hz repetition rate [23, 26]. The kicker field can be raised within the 50 μs gap to deflect the bunches dedicated for FLASH2 to the corresponding position in the septum (drawings are not to scale).

It has already been mentioned in chapter 3 that CSR necessitates a suitable beam line layout in the extraction arc in order to mitigate the associated effects on the electron beam and two possible techniques were briefly introduced. Due to the fact that FLASH is a very densely packed machine, there are additional boundary conditions which have to be taken into account and which bring in restrictions regarding the free choice of the beam line design. For example, the photon beam line of FLASH2 has to cross the tunnel of the third generation synchrotron light source PETRA III [7] in order to reach the experimental hall which is built on the other side of the ring. Since the distance between the extraction position and PETRA III is fixed, and since the length of the undulator beam line cannot be shortened without deteriorating the photon beam quality and intensity, the extraction arc has to be designed as short as possible. This fact, besides the lack of space at the extraction position, prevented a lattice layout using the -I transfer matrix for CSR mitigation. Thus the second method using the defined Twiss functions in the bending magnets will be used for the extraction arc.

Besides the mitigation of CSR effects, further conditions resulting from the requirements on the beam quality in FLASH2 must be taken into account. This includes a closed dispersion in both transverse planes as well as a zero longitudinal dispersion (no compression or decompression of the bunches in the extraction arc).

FLASH2 will be equipped with 12 variable gap undulators which allow to change the photon wavelength, within limits, independently from the electron energy and thus also independently from FLASH1. It will be possible to vary the undulator gap between 9-18 mm which corresponds approximately to an rms undulator parameter K_{rms} between 0.7 and 2.0. The FLASH2 undulator period will be 31.4 mm and the focusing of the beam will be realized using a FODO structure with an average beta function of 6 m. The plots in figure 4.4 show the relation between the undulator gap size and the emitted photon wavelength for three typical electron beam energies in FLASH. The photon wavelength of 13.5 nm can be obtained for beam energies between 0.7 GeV and 1.2 GeV. This is important because about one third of the actual experiments at FLASH use this wavelength [24] and it was demanded to provide this beam to the users independently of the wavelength in FLASH1.[2]

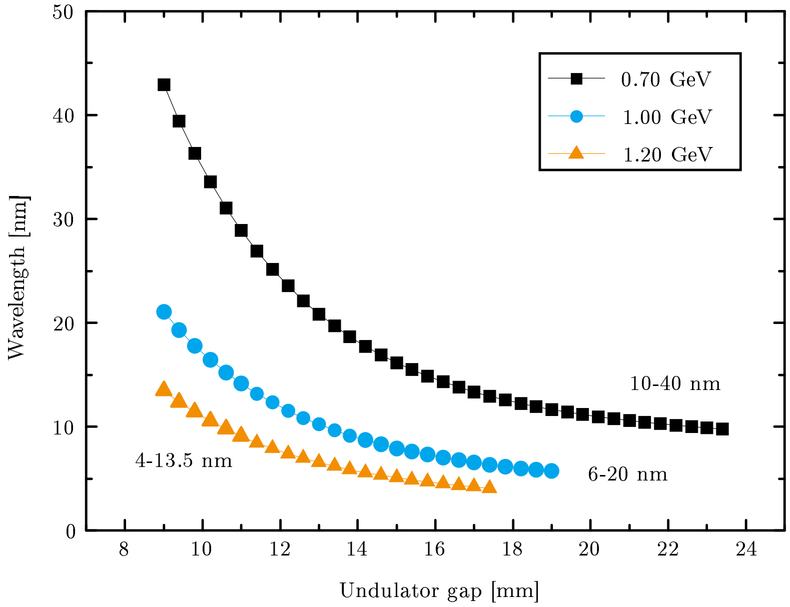

Figure 4.4.: This plot shows the possible wavelength range for three different beam energies. One can see that the wavelength of 13.5 nm is available for all presented beam energies.

A summary of the main electron and photon beam parameters of FLASH2 can be found in the tables 4.1 respectively 4.2 [24, 25]. The typical bunch charges for both beam lines

---

[2] FLASH1 uses fixed gap undulators, thus, the wavelength in this beam line can only be varied with the beam energy.

of FLASH are in a range between 100 pC and 1 nC. In order to present an overview of these particle distributions, plots including additional information are presented in appendix B in the figures B.1 - B.8. These distributions were also used for the start-to-end simulations as presented in chapter 7.

At the time of writing, the modifications of FLASH1 have finished, but the construction of FLASH2 is still on-going. The FLASH2 commissioning with an electron beam is scheduled to take place in 2014 and FLASH1 is scheduled to be commissioned until October 2013. This implies that FLASH1 can be operated while the FLASH2 beam line is still under construction.

Table 4.1.: The electron beam parameters of FLASH2.

Energy range	0.7-1.25 GeV
Peak current	2.5 kA
Charge range	(0.02 nC -) 0.1 - 1 nC
Max. pulses per train	800

Table 4.2.: The photon beam parameters of FLASH2.

Wavelength range	4.1-40 μm
Average single pulse energy	1-500 μJ
Pulse duration (FWHM)	10-200 fs
Peak power	1-5 GW
Peak brilliance[2]	10^{28} -10^{31}

---

[2] Specified in units of $photons/(s\ mm^2\ mrad^2\ 0.1\%\ bandwidth)$

5. Multi Variable Optimization

5.1. Introduction

In order to find a suitable layout for the extraction arc of the new beam line FLASH2, many simulations were carried out using the simplex optimization algorithm as implemented in the tracking and optimization code `Elegant` [27]. The aim of this chapter is to provide an insight to the challenges which had to be solved during the optimization process, starting with common explanations about multi variable optimization on the basis of a simplified example with two variables and proceeding with the presentation of the more specific approach to the optimization of the extraction arc.

5.2. Optimization Function

Before starting an optimization, one has to develop an optimization function. This function consists usually of several summands whereby their number is determined by the number of given constraints. Let us assume, for example, that the Twiss function α should have specific values τ_1 and τ_2 at two given positions s_1 and s_2 and that the course of α is determined by the strength of two quadrupole magnets k_a and k_b. In this case, the constraints can be described as:

$$\alpha(s_1, k_a, k_b) = \tau_1 \qquad \text{and} \tag{5.1}$$

$$\alpha(s_2, k_a, k_b) = \tau_2. \tag{5.2}$$

Before we can build an optimization function using these constraints, they have to be described as functions which are zero when the required values are obtained (least squares approach):

$$f_1(k_a, k_b) = \left(\frac{\alpha(s_1, k_a, k_b) - \tau_1}{\sigma_1}\right)^2 \qquad \text{and} \tag{5.3}$$

$$f_2(k_a, k_b) = \left(\frac{\alpha(s_2, k_a, k_b) - \tau_2}{\sigma_2}\right)^2, \tag{5.4}$$

whereby σ_1 and σ_2 are weighting factors which can be used if one of the constraints is more important for the result than the other. If the importance of both functions is the same, set $\sigma_1 = \sigma_2 = 1$. The final optimization function is then composed of the functions as described above:

$$f(k_a, k_b) = f_1(k_a, k_b) + f_2(k_a, k_b). \tag{5.5}$$

The aim of an optimization run is to find a set of variables $k_{a,\text{min}}$ and $k_{b,\text{min}}$ describing the global minimum of the optimization function. The distinction between a local and a global minimum can be explained as follows: For a set of optimization parameters $\vec{x}_1$ describing a local minimum of the optimization function, it applies that

$$\begin{gathered} f(\vec{x}_1) \leq f(\vec{x}_i) \text{ for all sets of optimization parameters } \vec{x}_i \\ \text{satisfying } |\vec{x}_i - \vec{x}_1| \leq \epsilon \text{ for some } \epsilon \geq 0. \end{gathered}$$

For a global minimum however, the statement $f(\vec{x}_1) \leq f(\vec{x}_i)$ is true for all parameter sets $\vec{x}_i$ without any restrictions [28].

5.3. Downhill Simplex Algorithm

The downhill simplex algorithm[1] was invented by John Nelder and Roger Mead in 1965 and it will be described in more detail because it was used to optimize the extraction arc for the new beam line FLASH2. The simplex algorithm is appropriate for optimizations with nonlinear functions depending on a large number of variables.

The algorithm uses a heuristic approach that means it is necessary to have some knowledge of the system to be optimized and to use it for the optimization process. On the basis of this information, conjectures and conclusions can be drawn about how to proceed with the optimization. Typically, the information used for that are the values of the optimization function obtained with the current set of variables and the optimization function calculated with the potential next set of variables. This approach allows to run the optimization without calculating the derivatives of the related function which is an

---

[1] This section is partly based on the following articles from the free online encyclopedia Wikipedia: Simplex Algorithm, Nelder-Mead Method, Hill Climbing, Search Algorithm, Simplex, Polytope and Heuristic.

advantage over many other algorithms because it reduces the required computing time and makes the optimization also more robust.

Before starting an optimization with N variables, according to Nelder and Mead, one has to select $N+1$ initial sets of variables $\vec{x}_1, \ldots, \vec{x}_{N+1}$ with $\vec{x}_i = (x_1, x_2, \ldots, x_N)^T$ and calculate the optimization function's values $f(\vec{x}_1) \ldots f(\vec{x}_{N+1})$. Chose the indices of the variable sets such that the following applies: $f(\vec{x}_1) \leq f(\vec{x}_2) \leq \cdots \leq f(\vec{x}_{N+1})$. Thus, $\vec{x}_1$ has the lowest function value and $\vec{x}_{N+1}$ the highest. This sorting will make it easier to explain the further description of the optimization process.

Each set of variables $\vec{x}_i$ represents a vertex of an N-simplex (an N-dimensional polytope) in the variable space of the optimization function. To give a few examples: The 1-simplex is a line with two vertices, the start and the end point. The 2-simplex is a triangle in a two dimensional variable space and the three vertices are the connections between the lines. In three dimensions, the 3-simplex is a tetrahedron with four vertices and so on.

In each optimization step, the algorithm uses one out of its four possible operations: reflection, contraction, expansion or reduction of the N-simplex. Each of this operations has the goal to move the vertices of the simplex closer to the global minimum. In the first three cases, the worst set ($\vec{x}_{N+1}$) will be replaced by a new one $\vec{x}_n$ if $f(\vec{x}_n) < f(\vec{x}_{N+1})$. The new set $\vec{x}_n$, obtained using the set $\vec{x}_{N+1}$, will be carried out in relation to the center of gravity $\vec{x}_0$ of the remaining sets $\vec{x}_1 \ldots \vec{x}_N$ which can be calculated as follows:

$$\vec{x}_0 = \frac{1}{N} \sum_{i=1}^{N} \vec{x}_i. \tag{5.6}$$

If the fourth operation, the reduction, is used to calculate the vertices for the next optimization step, the last N sets $\vec{x}_2 \ldots \vec{x}_{N+1}$ will be modified such that the simplex is contracted in the direction of $\vec{x}_1$.

All possible operations will be described in more detail below and the conditions for their use are presented in the flowchart shown in Fig. 5.1.

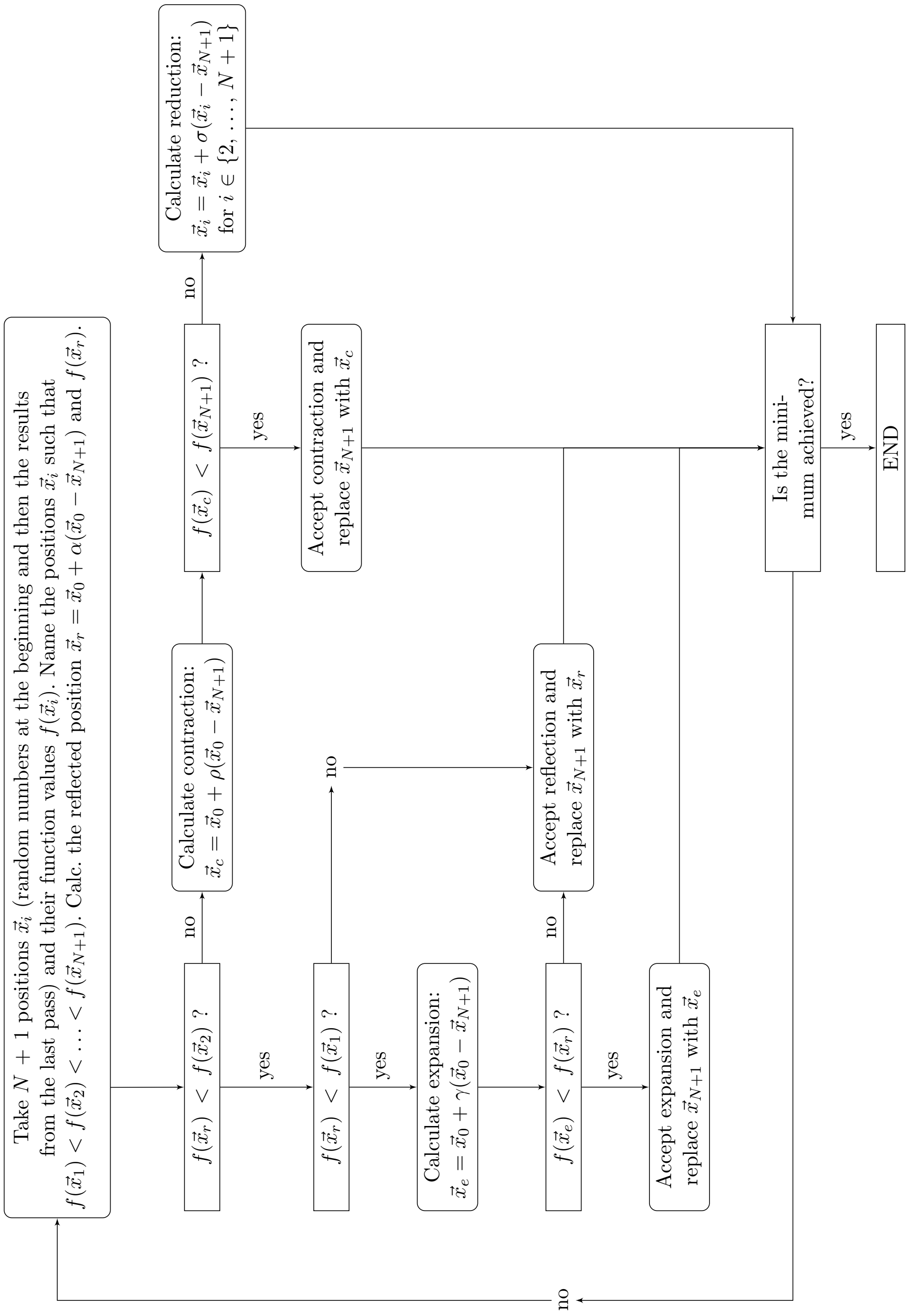

Figure 5.1.: Flowchart for the downhill simplex algorithm. There are four different operations applicable: reflection, contraction, expansion and reduction. The decisions on how to proceed with the optimization are made on the basis of the comparison between the optimization function's values for different sets of variables.

- **Reflection**: The variable set with the highest function value $\vec{x}_{N+1}$ will be reflected at the center of gravity of the remaining particles $\vec{x}_0$. The new set is then called $\vec{x}_r$. The reflection coefficient α can be used to stretch or shrink the new simplex and the recommended value for $\alpha = 1$. The position $\vec{x}_r$ can be calculated as follows:

  $$\vec{x}_r = \vec{x}_0 + \alpha\,(\vec{x}_0 - \vec{x}_{N+1}). \tag{5.7}$$

  The function value of the new set $f(\vec{x}_r)$ has to be calculated as well in order to be able to continue the optimization as described in the flowchart in figure 5.1.

- **Expansion**: This step is like the reflection but the expansion coefficient γ is larger than α, the coefficient of the reflection. Thus, the new vertex described by $\vec{x}_e$ is further beyond the center of gravity $\vec{x}_0$ of the remaining particles. A common value for γ is 2. How to calculate the expansion position $\vec{x}_e$ is presented in the following formula:

  $$\vec{x}_e = \vec{x}_0 + \gamma\,(\vec{x}_0 - \vec{x}_{N+1}). \tag{5.8}$$

  The next step of the algorithm depends on the ratio between the function value of the reflected set $f(\vec{x}_r)$ and the function value of the expanded set $f(\vec{x}_e)$ and is described in the flowchart.

- **Contraction**: In many cases it is better to contract the simplex by reducing the distance between the variable set with the highest function value $\vec{x}_{N+1}$ and the gravity center of the remaining positions $\vec{x}_0$. The contraction coefficient ρ is recommended to be -0.5. The calculation of $\vec{x}_c$ is described in formula 5.9.

  $$\vec{x}_c = \vec{x}_0 + \rho\,(\vec{x}_0 - \vec{x}_{N+1}). \tag{5.9}$$

  The ratio between the new function value $f(\vec{x}_c)$ and the worst one so far $f(\vec{x}_{N+1})$ determines the next step as described in figure 5.1.

- **Reduction**: The vertices described by $\vec{x}_2, \ldots, \vec{x}_{N+1}$ are shifted towards the position with the lowest function value $\vec{x}_1$. The reduction coefficient σ determines the size of the new simplex and its recommended start value is 0.5.

  $$\vec{x}_i = \vec{x}_i + \sigma\,(\vec{x}_i - \vec{x}_1) \qquad i \in \{2, \ldots, N+1\}. \tag{5.10}$$

  Since this is the final step in the main loop of the optimization algorithm, no further comparisons of function values are required. In fact, all variable sets except x_1 will be exchanged with the related new values calculated with formula 5.10.

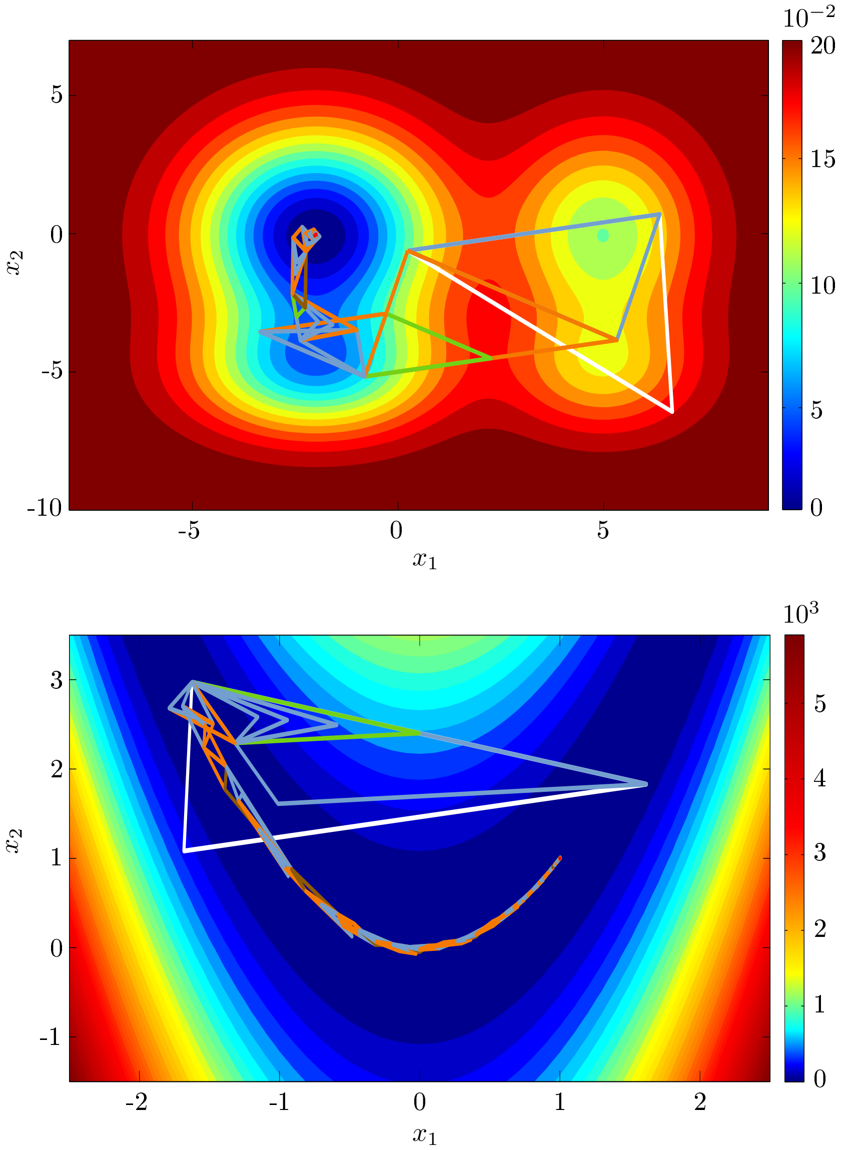

Figure 5.2.: Examples of the downhill simplex algorithm finding the global minimum of two different functions with two variables. The upper plot shows a function with three local minima and one global minimum. The aim is to find the global minimum without getting distracted by the other minima. The lower plot shows the Rosenbrock function where the global minimum is located at position (1,1). Finding this positions is difficult because its located in a long narrow valley. The different colors of the triangles represent the four possible actions of the algorithm. Orange stands for reflection, brown for expansion, blue for contraction and green for reduction. The white simplizes represent the randomly chosen starting values.

The operations of the downhill simplex algorithm are repeated in the main loop (cf. figure 5.1) until, in the ideal case, the global minimum of the optimization function is reached within the defined tolerance. Occasionally, it can happen that the optimization process stops in a local minimum and that has to be recognized in order to be able to reject the corresponding result. How this can be applied during the optimization of an extraction arc will be explained later in a more specific example, but just one remark: It helps to restart the optimization several times with different initial variable sets and to compare the results of all runs to be able to distinguish the local minima from the global minimum.

A script for MATLAB[2] performing the downhill simplex algorithm was prepared to show the abilities of the algorithm on the basis of two simple examples with each two variables. The results of these optimizations are presented in figure 5.2. The starts of both optimizations were carried out with randomly selected values. The simplizes of the individual optimization steps (in this case with $N = 2$ variables, the simplizes are triangles) are plotted in different colors representing the different operations used during the optimization process.

The first function[3] shown in the upper plot of figure 5.2 is combined out of four Gaussian distributions and has three local minima besides the global minimum. The difficulty in this case is to find the global minimum without getting stucked in one of the local minima. In spite of the fact that the vertices at the start are distributed in the area of two local minima, the algorithm managed to find the global minimum as demanded.

In the second example, the algorithm was applied on the so called Rosenbrock function.[4] This function is well suited and often used to test optimization algorithms. Its particular feature is that the global minimum is located in a long narrow valley surrounded by steep slopes and thus it is difficult to be found. The path of the simplizes representing the searching process shows that the valley itself can be found within a few steps but the

---

[2] MATLAB, a numerical computing environment developed by MathWorks. The script is presented in section C.

[3] $f(x_1, x_2) = \left(\frac{1}{2}\exp\left[\frac{-(x_1-5)^2}{5}\right] + \exp\left[\frac{-(x_1+2)^2}{8}\right]\right)\left(-\frac{1}{5}\exp\left[\frac{-x_2^2}{13}\right] - \frac{1}{8}\exp\left[\frac{-(x_2+5)^2}{5}\right]\right) + 0.21$

[4] $f(x_1, x_2) = (1 - x_1)^2 + 100\,(x_2 - x_1^2)^2$

algorithm managed also to travel along the valley bottom and to find the global minimum at the position $\vec{x}_{\text{gm}} = (1, 1)$.

These two examples show the ability of the algorithm as used in the script to find the global minimum, at least for optimization functions with two variables and under the circumstances that the optimization function is known previously. However, for the optimization of a complex beam line layout it is essential to have a program which can handle more variables and it would be an advantage if this program is also capable of calculating the optimization function itself. On this account, amongst others, it was reasonable to use existing optimization programs, like `Elegant`, which fulfill these demands instead of elaborating the script used for the simple examples as presented above. In addition, the downhill simplex algorithm as used in `Elegant` comes with additional features which help to complete the optimizations successfully. These features will be explained, inter alia, in the next section.

5.4. Optimization Procedure for the New Beam Line FLASH2

A simple example to demonstrate the operational capability of the downhill simplex algorithm as presented previously takes a few seconds to find the global minimum with a high probability, irrespective of the variable's values at the start. This is not the case when it comes to more complex tasks like the optimization of the extraction arc for the new beam line FLASH2. If the brute force method[5] is used for the optimization of such a case, it will not succeed because the number of variables and conditions is too large to find the global minimum of the optimization function. This approach would lead with a high probability to a local minimum or several variables will reach their maximum values, which, in turn, will cause the termination of the process. The only possibility to be successful with this method is to start with a set of variables being close to their optimized values, which is a very unlikely situation if one starts with a randomly generated set. Thus, the brute force method can only be applied on such a problem to refine an existing solution at the end of the optimization procedure.

---

[5] Running the optimization using the brute force method means here that all conditions are implemented to the process and all variables (all magnet positions and strengths) are part of the optimization from the beginning. Furthermore, it means that no further assistance based on knowledge concerning the algorithm respectively the beam optics is used.

It is rather necessary to start an optimization using the available knowledge about beam optics in an extraction arc and the knowledge about the interactions between the single optics functions in order to be able to guide the optimization process on a successful path. Furthermore, it is important to take the characteristics of the used algorithm into account. Considering these things allows to include useful additional conditions (or to replace existing conditions with new ones) which are easier to be implemented to the optimization but which have the same outcome. To present an example: Instead of demanding the same horizontal beta functions with opposite slopes at the start and at the end of a drift section (comparing four variables $\alpha_1, \alpha_2, \beta_1$ and β_2 and setting two conditions $\alpha_1 = -\alpha_2$ and $\beta_1 = \beta_2$) one could instead demand a beam waist in the middle of the drift (just one variable and one condition $\alpha_c = 0$). Due to the courses of the beta functions in a drift section, this will lead to the same result but it requires less computational power, thus, it will reduce the time required for the optimization.

It is essential to understand which effects could cause beam quality impairment, e.g. coherent synchrotron radiation (CSR, cf. chapter 3), in order to be in a position to circumvent them. As it was mentioned in chapter 2 and as it will be covered in the following chapter, the beam quality impairment caused by this effect can be mitigated using specific beam optics which can be implemented to the optimization as constraints for the Twiss functions α and β at the concerning position. The other, less favorable, possibility to mitigate emittance growth due to CSR would be to track a large number of particles after each optimization step in order to be able to analyze the beam quality and to make a decision if the last step caused an improvement or a deterioration. Finally, both approaches will work and the beam quality will be improved after the optimization but the first method will take just a fraction of the time that would be needed by the second approach.

As mentioned before, the variable's start values have a large impact on the progress of the optimization, thus, they have to be considered as well. It is recommended to use e.g. quadrupole strengths in the range of their likely final values if that is possible. This will not be realizable for each magnet but, to give an example, a quadrupole upstream a required horizontal beam waist must have a positive gradient (it will be focusing in the horizontal plane) and the start value can be chosen accordingly. There are also quadrupoles in the beam line whose required strengths are difficult to be estimated and whose start values are usually set to zero. But, if an optimization attempt was not successful, it can help to use randomly chosen values for these quadrupole magnets' strength instead of a zero gradient.

Furthermore, the weight of each optimization function's summand has to be carefully audited, otherwise, the conditions with a too high quantification will be optimized at the expense of the others and this will prevent a successful process. It is advisable to chose the same weighting parameters for all conditions in the first optimization attempts and to modify the values step-by-step depending on the development of the optimization.

It is also useful to split the optimization procedure into several simpler units which can be solved step-by-step. For example, if a beam waist is required in the front section of the beam line, it is sufficient to consider the elements upstream this position because the other elements have no influence on it, but, including unnecessary beam line elements to the optimization increases the computing time.

In addition to the above mentioned advices, it is recommendable to keep the course of the optimization function in view. Depending on the development of its summands during the process one can understand which constraint prevents a successful completion or which variable is already at its maximum. This is also a possibility to see if the optimization process is trapped in a local minimum.

The last paragraphs have expressed the need of a well considered approach to the optimization of the FLASH2 extraction arc and it was pointed out that, in case that the optimization process has to be accelerated, one could simply upgrade the used computer system but in the most cases it makes more sense to reconsider the optimization strategy and, if its applicable, to make relevant modifications in order to improve it. The actual approach used to optimize the FLASH2 extraction arc will be explained in the following to give an example how an optimization strategy can be put into practice.

The simplex algorithm as implemented in `Elegant` comes with additional features which help to shorten the optimization respectively to necessitate less manual restarts. Three parameters, the number of evaluations, the number of passes and the number of restarts are the decisive parameters of these features. The number of evaluations sets how many evaluation steps will be taken before the optimization run stops, even if the target value of the optimization function (which is usually zero) has not yet been achieved. The number of passes defines how often the optimization will be repeated. The termination conditions for a pass are fulfilled when the number of evaluations is reached, when the optimization function is equal to the target value within the defined tolerance or when the optimization process is bogged down in a local minimum. The latter is the case when the function value does not change over several optimization steps while the target value has not been reached. For every pass, the simulation will be restarted using individually preassigned step sizes for each variable. The third parameter, the number of restarts, is an additional loop around the number of passes. The difference in this loop is that for the restarts, the optimized set of variables and not the initial set is used. This feature is recommended to be used if convergence problems appear. A flowchart showing the additional loops is presented in figure 5.3

The first step designing the FLASH2 extraction arc was to find suitable positions and strengths for the bending magnets such that the beam will be directed to the beam dump's position. Before the decisions regarding the dipole magnet's positions and deflection angles were made, considerations were given to the courses of the horizontal and longitudinal dispersion in the beam line. The synthesis of these thoughts resulted in a set of three bending magnets, where the second one deflects the beam with a small angle in the opposite direction than the two other magnets. This trick helps to improve the beam quality in FLASH2 and the reason for this will be described in chapter 6. Important is that this layout, and thus the improved beam quality, is based on the use of beam optics knowledge and it is unlikely that it could also have been obtained using the brute force method.

Once the dipole magnets' positions are defined, an operable set of quadrupole magnets distributed over the arc had to be determined in order to be able to control the courses of the optics functions. Each quadrupole has an impact on the beam quality and, in addition, there is very little space in the extraction arc for FLASH2. Thus, a solution had to be found which gets along with the smallest possible number of quadrupole magnets. This solution can only be approached step-by-step, starting with an estimated number of quadrupoles and adapting it to the demands during the optimization. In doing so, it is an advantage to start with more quadrupoles than eventually necessary (and not with less) because that enables the opportunity to reduce the strength of the surplus quadrupoles step-by-step and to replace them finally with drift sections. This is easier to put in practice than adding a quadrupole every time when it becomes evident that the actual number of quadrupoles is not sufficient to find a solution.

The required number and the distribution of the quads, as well as their approximated strength had to be estimated for the first optimization run on the basis of the requirements given by the beam optics. For example, if it is necessary to have defined Twiss functions in one plane at a certain position (e.g. in the horizontal plane, viz. the defined parameters are α_x and β_x) one will need at least two quadrupole magnets upstream of this position to achieve the two constraints. A similar task comes up when the beam has to be matched into a FODO structure e.g. at the end of the FLASH2 arc. This entails fixed Twiss functions in both planes, in other words, there are four constraints and thus one needs at least four variables appropriable in the optimization (normally the strength of four quadrupole magnets) to be able to achieve a perfect matching regardless of the Twiss functions at the start of the matching section.

In common, one can say that the number of optimization variables has to be at least the same or higher than the number of given constraints. But it should be considered that there are additional constraints which get easily forgotten: Having four quadrupoles at fixed positions to match into a FODO structure does only work in practice if the beta functions in between do not grow too large and if the maximum quadrupole strengths will not be exceeded. Otherwise, these additional boundary conditions will make it impossible to find a practicable solution. It has to be considered that a beam line layout in which each magnet position and strength is a fixed matching condition which can not be modified in the future if necessary e.g. for new diagnostic devices which could require a different beam optics. This problems can be circumvented by adding additional quadrupoles at critical positions to have further variables for the optimization. But this has to be evaluated carefully in order not to exceed reasonable costs and not to use drifts spaces which are needed for other beam line elements.

The priorities of the first quadrupole optimization run depends on the beam line layout and on the requirements given by the beam optics, respectively by the demands on good beam quality. It will take a few attempts until a suitable set of constraints (including their weighting factors and tolerances) will be found for the start of the optimization. To give an example: One possibility is to start with the main focus on the compliance of the maximum beta functions in both planes. But in order to guide the optimization in the direction of a useful overall result, the further requirements, like for example the horizontal and longitudinal dispersion, must also be taken into account, but with lower weighting factors and larger tolerances. In the subsequent optimization steps, these additional conditions have then to be more and more emphasized until they are also fulfilled. But, it can also be the case that it is the better approach to close first the dispersion, no matter what the maximum beta functions are, and to reduce them in the following steps.

The septum type which will be used for the FLASH2 extraction arc requires a vertical beam offset for the extracted particles which will be obtained with kicker magnets (cf. section 6.2). This fact leads to vertical dispersion in FLASH2 which had to be considered in the simulations. However, the deflections and the offset in the vertical direction are small compared with those in the extraction plane, which made it sufficient to start the simulations without the vertical kickers and to add them after a solution for the rest of the extraction arc was found.

For each step described so far, it is advisable to start the optimization using the first order matrices as long as the higher order effects are not necessary to be considered. Using second order matrices during an optimization with `Elegant` makes the process measurably slower and using third order matrices can only be suggested if the corresponding effects have to be included at all costs and if the fundamental framework of the lattice layout was already obtained using matrices of a lower order. During the optimization of the FLASH2 arc, it became clear that the second order horizontal dispersion has to be closed using sextupole magnets. This was done after all other optimization processes were completed and only the sextupole magnet's strengths were part of the optimization. This minimization of variables and conditions allows still an acceptable optimization speed. A comparable situation occurs with the use of collective effects, like the calculation of coherent synchrotron radiation, in the simulations. Again, it is recommended to start with a minimum of additional effects and switch them on step-by-step if their use is necessary.

At the end of the optimization process when a solution including all demands has been found, one can start a last simulation including all variables and all constraints used during the optimization process with the aim to squeeze out even the last optimization possibilities. In these last runs one can try to reduce, for example, the strength of the strongest quadrupole magnets, which is an advantage for the beam quality. Or one can try to close the second order dispersion with smaller values for the sextupole magnets in order to reduce their impact on the beam. This approach was described at the beginning of the chapter as the brute force method and no chance to succeed was granted to it if one tries this at the start of the optimization process. But it was also mentioned that it is a possibility to use this method at the end of the process in order to refine the solution. A flowchart including the most important steps of the FLASH2 optimization process is presented in figure 5.3.

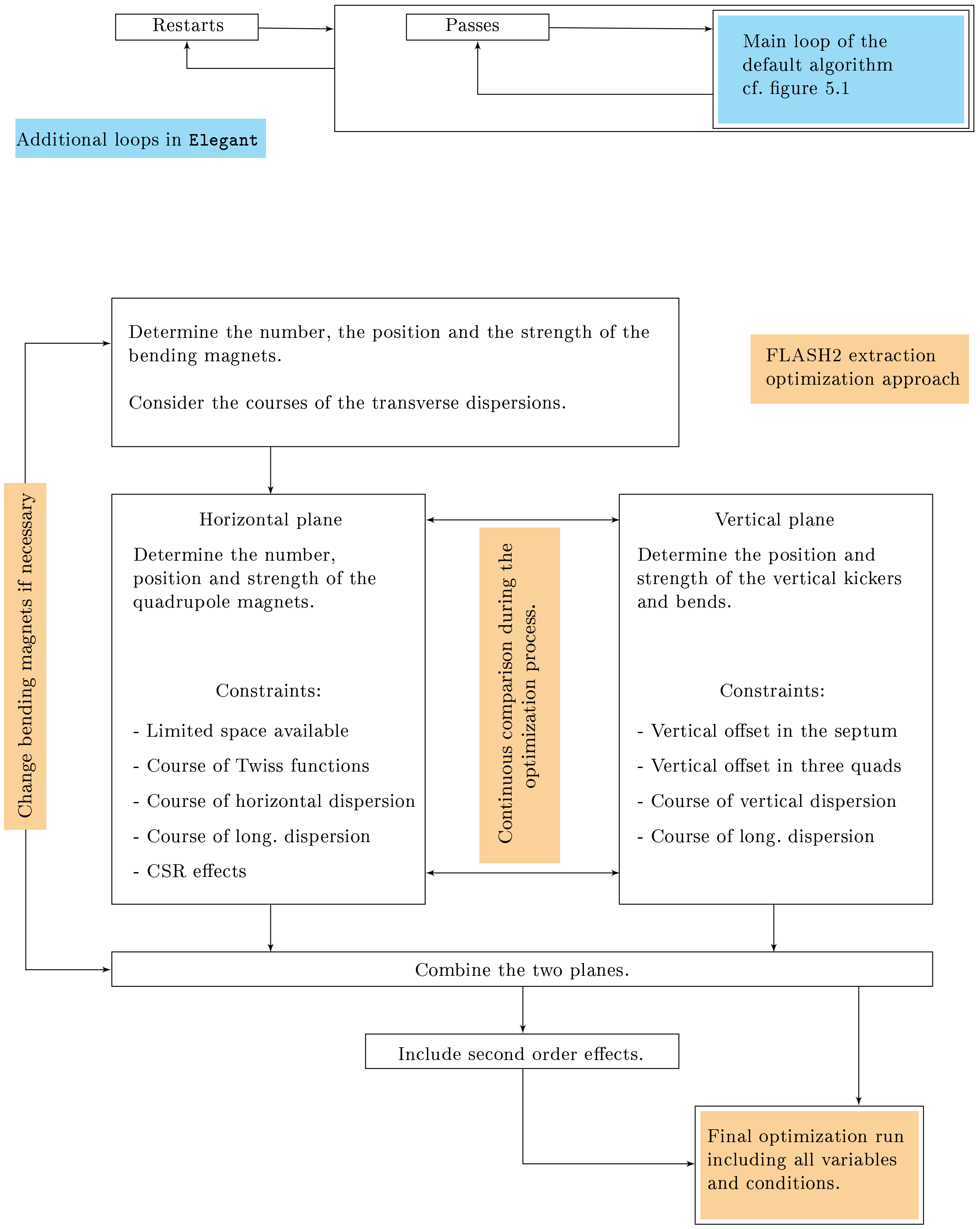

Figure 5.3.: Flowchart of the extraction procedure for FLASH2. The upper part shows the additional loops for the number of passes respectively the number of restarts as implemented in `Elegant`. The second part describes the optimization process of the extraction arc.

In order to give an idea about how many optimization variables and constraints were considered in the optimization of FLASH2, they will be listed here briefly. There are three vertical kickers[6] in the beam line, four horizontal and two vertical bending magnets. The total number of quadrupole magnets in the extraction arc and in the following seeding section, which was partially used to match the beam into the undulators, is 21 and there are three sextupole magnets in the extraction arc. Each magnet adds at least two variables to the optimization, its strength and its position. Taking the number of 33 elements as enumerated above, this leads to at least 66 variables for the optimization. In fact, this is only the number of elements implemented to the final beam line after the optimization. At the beginning of the procedure, the number of quadrupole magnets was larger and in addition, neither their positions nor their sorting was determined and had to be worked out step-by-step.

During the optimization, one has to obtain all mentioned requirements necessary for a successful FEL operation like closed dispersion in both transverse and in the longitudinal direction. The importance of the CSR effects mitigation was mentioned several times and this leads to constraints for the horizontal Twiss functions at the strong horizontal bending magnets (cf. chapter 3 and section 6.4). The strengths of the sextupole and quadrupole magnets are limited, on the one hand by their design limit, but also due to the chromatic aberrations which are induced by these elements if high magnetic field are applied. This fact impeded an earlier solution for the extraction arc. The maximum values of the optics functions have to be considered which is a weighty restriction during the optimization. This includes the Twiss functions, the transverse dispersion and also the longitudinal dispersion. The latter is necessary because the more the bunch is compressed the higher are the CSR effects in the following bending magnet and space charge effects can become relevant if the temporary compression is too strong. Finally, many drift spaces must be kept free for beam diagnostic, vacuum and safety elements. In the final extraction including the seeding section of FLASH2 there are now four beam valves, several beam shutters, six screens, three toroids, more than 20 ion pumps, more than 20 steerers as well as three collimators.

These large numbers of variables and constraints make it necessary to follow an optimization procedure as described above or a comparable solution. But it is evident that just the brute force method cannot be used for this task.

---

[6] All elements of the final FLASH2 beam line layout which are listed here are described in chapter 6.

6. FLASH2 Beam Line Layout

6.1. Introduction

This chapter introduces the layout of the extraction arc for FLASH2 including the associated beam line elements. It is divided in three sections describing the beam distribution to FLASH2, the longitudinal and the transverse phase space. The applied program for the optimization of the beam line was the tracking and optimization code `Elegant` [27] using the simplex downhill algorithm as described in chapter 5. The programs csrtrack [29] and Genesis [30] were used for particle tracking respectively for FEL simulations, both in order to test and assess the beam line layouts during the development.

6.2. Beam Distribution to the New Beam Line

The beam distribution between the existing beam line and the extraction arc will be realized with three kickers and a Lambertson septum [31]. The requirements on the septum are to provide a high magnetic field quality and to be robust against electron impact. A Lambertson septum is operated with a DC current which allows to obtain a stable magnetic field. The uniform spacial distribution of the field is achieved with an appropriate shape of the magnet yoke. In this septum type, the electron bunches in both beam lines are not close to crucial components of the septum, thus, a high reliability can be ensured.

However, using a Lambertson septum, the kickers have to deflect the beam not in the plane of the extraction arc but perpendicular to it, thus, they induce a vertical dispersion in addition to the horizontal dispersion caused by the bending magnets of the extraction arc.

In a current sheet septum, which could provide the same field quality as a Lambertson septum, are the positions of the straight beam and the deflected beam separated by a metal sheet which is used as the outer coil of the septum. The high current density in this sheet requires a water cooling system which is close to the beams and can eventually be damaged by electron impact.

A schematic plot of the field in a Lambertson septum is shown in 6.1 [32]. The septum core is pictured as a shaded area and the field lines are presented as black curves. The coils are pictured as black rectangles including the signs for the direction of the current. Different colors from blue to red indicate the strength of the magnetic field as shown in the color bar on the right hand side. The position of the straight beam is shown as an orange dot in a recess of the septum core and the position of the deflected beam is presented as a red dot in the septum above. The light-blue area represents a part of the volume used for the calculation of the magnetic field distribution.

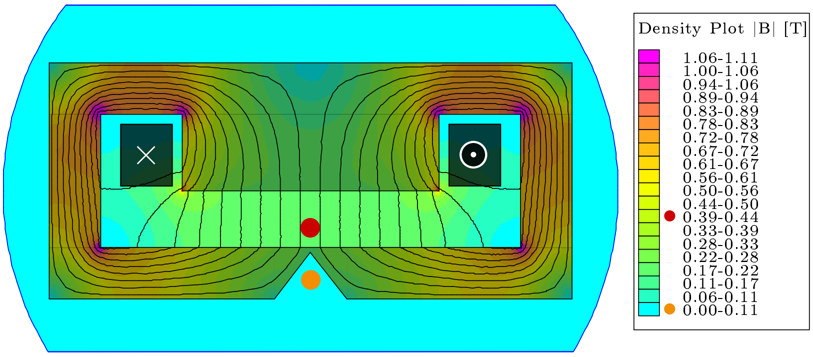

Figure 6.1.: Schematic plot of the magnetic field in a Lambertson septum. The two beam positions are indicated with dots in orange (straight beam) and red (deflected beam). The magnetic field strength in the deflecting volume complies with the required field for a 1 GeV beam in the FLASH2 septum.

The demands on small emittance and energy spread growth require a horizontal beam waist in the septum (cf. chapter 3, chapter 4 and section 6.4). To achieve this, three quadrupole magnets are installed between the kickers and the septum. The beam for FLASH2 will pass these quadrupoles with a vertical offset and thus the bunches will obtain additional vertical kicks. It was necessary to find a setting for the quadrupoles which fulfills the requirements given by the beam optics at the extraction position and which leads also the bunches to the deflecting volume of the septum. Both requirements are accomplished with the solution for the extraction arc in which the first two quadrupoles increase the kick and the last quadrupole steers the beam back to zero deflection at 2 cm offset as necessary for the extraction. A technical drawing of the kicker section and the course of the vertical beam center offset is depicted in figure 6.2.

The beam distribution to a proposed third beam line was also considered during the planning and the required elements can be installed at the end of the extraction arc of

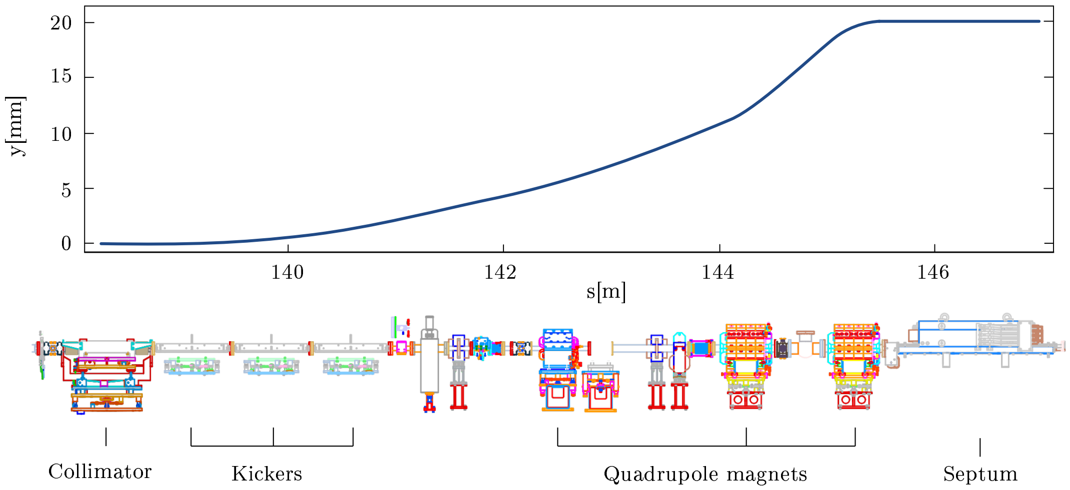

Figure 6.2.: The kicker section of FLASH2 contains of three fast vertical kickers, three quadrupole magnets and a Lambertson septum. The quadrupole magnets are necessary to obtain the required Twiss parameters in the septum and they are also used to amplify the deflection induced by the kickers. The last quadrupole is vertically focusing and bends the beam back to zero deflection.

FLASH2. Since there is not enough space to implement an additional kicker-septum-assembly, it is considered to extract the bunches with a pulsed bending magnet with a deflection angle of 8 °. The compromise which had to be made due to the restricted free space is a lower pulse repetition rate in the third beam line.

6.3. Optimization of the Longitudinal Phase Space Evolution

The extraction angle for FLASH2 is fixed by the building environment and will be 12 °. Many simulations were carried out to find a suitable distribution of bending magnets in the presence of further boundary conditions which will be discussed in the following sections.

A major demand on the arc was not to change the compression of the bunches. The bunch length can be adjusted with the bunch compressors installed in the linac and it is unwanted to get an additional modification during the extraction. The decisive parameter for the bunch compression is the longitudinal dispersion or R_{56}, the arc's transfer matrix element in the fifth line and the sixth column, relating the longitudinal particle positions and the relative energy momentum $\delta = \Delta p/p_0$:

$$\Delta s = R_{56}\,\delta. \tag{6.1}$$

In combination with an energy chirp where the particles in the bunch tail have a positive and those in the bunch head a negative energy deviation, a positive R_{56} leads to a compression of the bunches and a negative R_{56} accordingly to a decompression (cf. figure 2.1). As an element of the transfer matrix, the R_{56} is defined between a start position s_1 and an end position s_2. The relation between the R_{56}, the dispersion (R_{16}) and the bending radius of the dipole magnets in the arc (ρ) can be described by the following formula [33]:

$$R_{56}(s_1, s_2) = \int\limits_{s_1}^{s_2} \frac{R_{16}(s)}{\rho(s)}\, ds \tag{6.2}$$

To achieve zero R_{56} over the extraction arc, either the dispersion in one of the bends or the bending radius has to be negative in a part of the beam line. These two approaches are depicted in figure 6.3 and 6.4 on the basis of a simplified model. The approach using a sign change of the dispersion between the first and the second bend requires strong quadrupole magnets downstream the first bend which leads to strong beam perturbations due to chromatic aberrations. For this reason, I proposed the second variant, that means to install a weak reverse bend in the FLASH2 extraction arc.

A distribution of bends was developed in simulations which provides, in combination with a set of quadrupole magnets (cf. section 6.4), a closed dispersion in horizontal and longitudinal direction. It is also possible to adjust the R_{56} in a range of $\pm\,0.5\,\mathrm{mm}$ by small modifications of the focusing. Figure 6.5 shows the horizontal and longitudinal dispersion including the adjustment range. The positions of all magnets in the extraction arc are also depicted schematically. The element colors are: Orange for the kickers, blue for the quadrupoles, green for the bends and red for the sextupole magnets. These color assignments will be the same in all further plots.

The deflection angle of the septum is $6.5\,^\circ$, constrained by the requirements on the field quality in the deflecting volume, the demands on the shielding of the magnetic field in the area of the FLASH1 beam and the maximum possible septum length. The large deflection angle is necessary in order to separate the two beam lines as fast as possible to be able to install the next optics elements as close as possible to the septum.

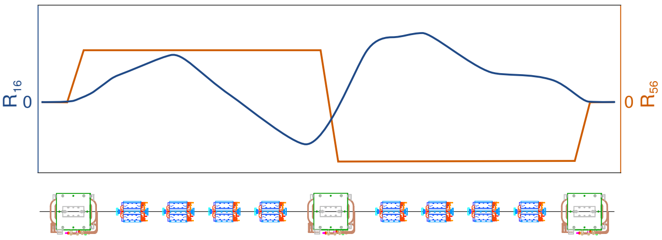

Figure 6.3.: In an arc with three equal bending magnets, a closed dispersion and zero R_{56} at the end of the arc can be achieved with a negative dispersion in the second bend.

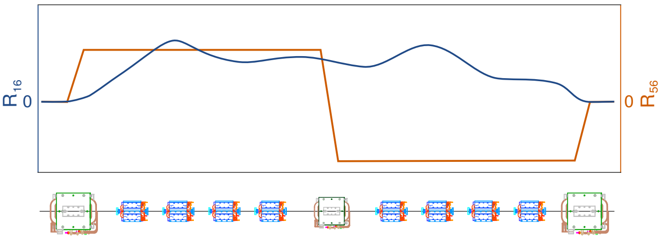

Figure 6.4.: Installing a small reverse bend in the middle of the arc allows to achieve zero R_{56} and a closed dispersion at the end of the arc without a sign change of the dispersion between the first and the second bend.

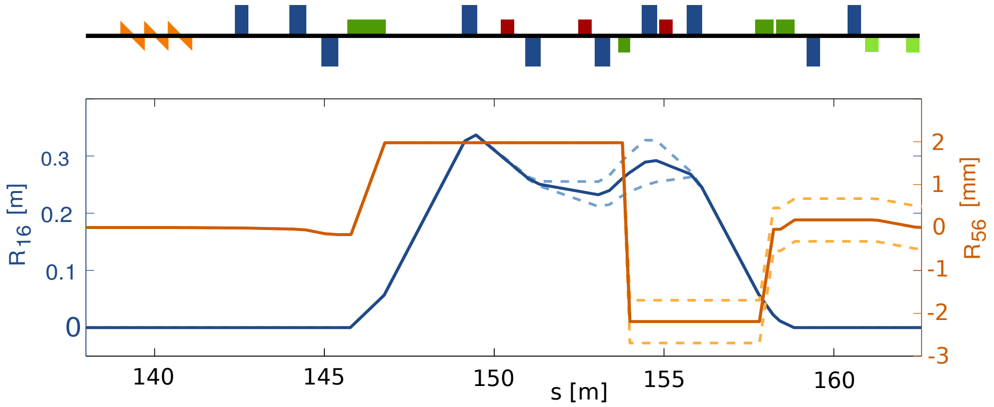

Figure 6.5.: The horizontal and the longitudinal dispersion (R_{16} and R_{56}) in the extraction arc. As required, the R_{16} is closed and the R_{56} is zero at the end of the arc. The possible adjustment range for the R_{56} is also presented. The positions of all magnets in this section can be found in the outline above the graph. The color code is: orange for the kickers, blue for the quadrupoles, green for the horizontal bends and light green for the two vertical bends.

The reverse bending magnet will deflect the beam by -0.9° which is, in combination with a large dispersion, sufficient to achieve a zero R_{56} over the extraction arc. The last two bends of the arc will have a total deflection angle of 6.4°. These magnets are no longer required spare magnets and they are as close together as possible to substitute a larger bending magnet.

Besides the fact that the R_{56} has to be zero at the end of the extraction arc, it had to be considered that its maximum along the arc is as small as possible in order to avoid emittance growth due to space charge effects caused by a strong temporary compression of the bunches. In the beam line for FLASH2, the maximum R_{56} of the extraction arc is below 2 mm and only caused by the strength and the length of the septum.

In order to find out if the optimization of the first order longitudinal dispersion is sufficient to prevent unwanted compression, the T_{566} was investigated as well and figure 6.6 shows the course of this parameter over the extraction arc. The maximum T_{566}, which is also the value at the end of the extraction, is about 35 mm. With an estimated relative momentum deviation in the order of $\delta = 10^{-3}$ (cf. appendix B) the maximum Δs caused by the second order longitudinal dispersion is:

$$\Delta s \;=\; T_{566}\,\delta^2 \;\approx\; 35\,\mathrm{mm}\;\left(10^{-3}\right)^2 \approx 35\,\mathrm{nm}. \tag{6.3}$$

The typical FLASH bunch length is in the order of $100\,\mu$m. Comparing the calculated Δs in the range of a few 10 nm with the bunch length, leads to the conclusion that the impact from the second order longitudinal dispersion on the bunch compression is negligible. Considering the zero R_{56} and the negligible contribution from the T_{566}, no impact from the longitudinal dispersion on the bunch length is expected. Thus, the current distribution of the bunches will not be changed by these parameters. But, there are other effects which can still modify the bunch form such as CSR. To investigate the impact of these effects on the particle distribution, a 250 pC bunch from a start-to-end simulation[1] was tracked from the last accelerating module to the start of the undulator section. The 250 pC bunch was chosen because it represents a typical particle distribution for FLASH. The results of the simulation are presented in figure 6.7. The first two plots on the left hand side represent the longitudinal phase space (a) and the current distribution (b) of the bunch before passing the arc. The wake field of the coherent synchrotron radiation

---

[1] The compression of this particle distribution was optimized for the existing beam line (Courtesy of I. Zagorodnov). It was a first test if the same compression scheme can be used for FLASH1 and FLASH2.

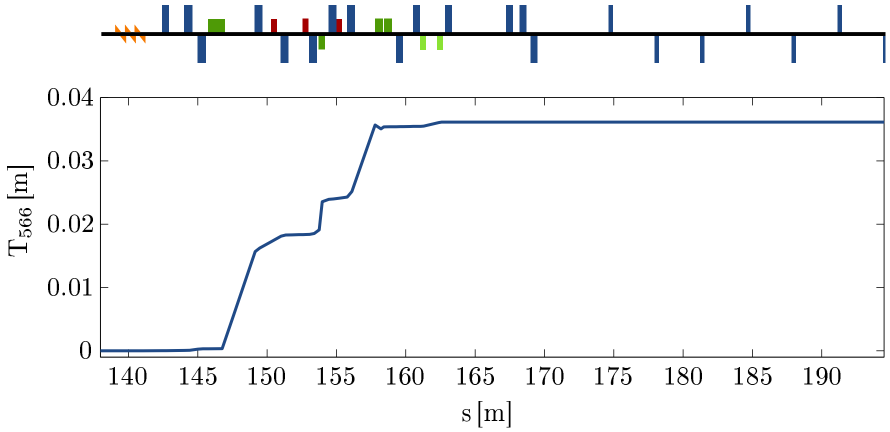

Figure 6.6.: Course of the second order longitudinal dispersion in the extraction arc for FLASH2.

causes an energy reduction around the bunch center as shown in plot c). The modification of the charge distribution (plot d) is also related to CSR and its origin will be explained below. To verify that the modifications are caused by CSR, a second simulation was carried out using the same setting except for the fact that the CSR effects were switched off. The longitudinal phase space and the current distribution at the end of the extraction arc from this simulation are shown in plot e) respectively in plot f). Both, the shape of the bunch in longitudinal phase space and the current distribution are changed very little in comparison with the bunch at the start position, which is in accordance with the assumption that the modifications of the longitudinal phase space are caused by CSR effects.

The CSR wake field changes the energy of the particles but it does not have a direct influence on the longitudinal positions of the electrons in the bunch. However, the assumption that a zero R_{56} over the arc will preserve the relative longitudinal positions of the particles, is only true if the particles energy is constant within this section. The energy change in the arc due to CSR disturbs the compensation of the compressing and decompressing effects in the bends and leads to the modified current distribution.

This interaction is illustrated using a simplified diagram in figure 6.8. The plots show in three steps how CSR, in combination with a dispersive section, changes the current distribution. All plots in the upper row show the longitudinal phase space and the plots in the row below the related current distributions. In the first step (plots a and b), one

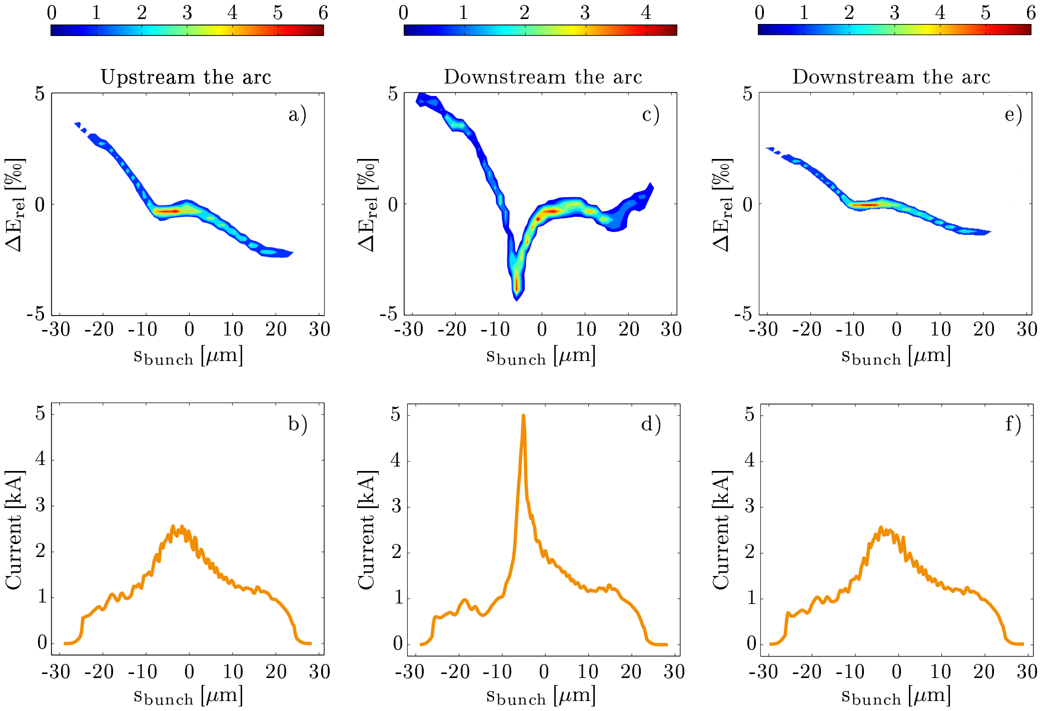

Figure 6.7.: These plots show the impact from CSR on a particle distribution in longitudinal phase space. The plots a) and b) show the distribution before passing the arc. Plot c) and d) present the same distribution behind the extraction. The CSR impact causes energy loss in the bunch center and a partially compression indicated by the high peak current. The last plots (e and f) show the same distribution at the end of the arc but tracked without CSR effects. The minor modification shown in these plots confirm the assumption that the modifications in plot c) and d) are caused by CSR.

can see a rectangular particle distribution[2] and the corresponding current distribution at the start. In the plots c) and d) one can see the situation after the impact of the CSR wake field recognizable by the reduced energy around the bunch center. The current distribution (plot d) is not affected by the modification of the energy. The last plots (e and f) show the situation when the distribution presented in c) traveled through the following section with a non-zero dispersion, e.g. a further bend, where the particles' positions are shifted longitudinally depending on their relative energy deviation δ. As shown in plot f) this causes the modification of the current distribution and a much higher peak current.

---

[2] This particle distribution has the same particle density at all longitudinal positions and no expansions in both transverse phase spaces.

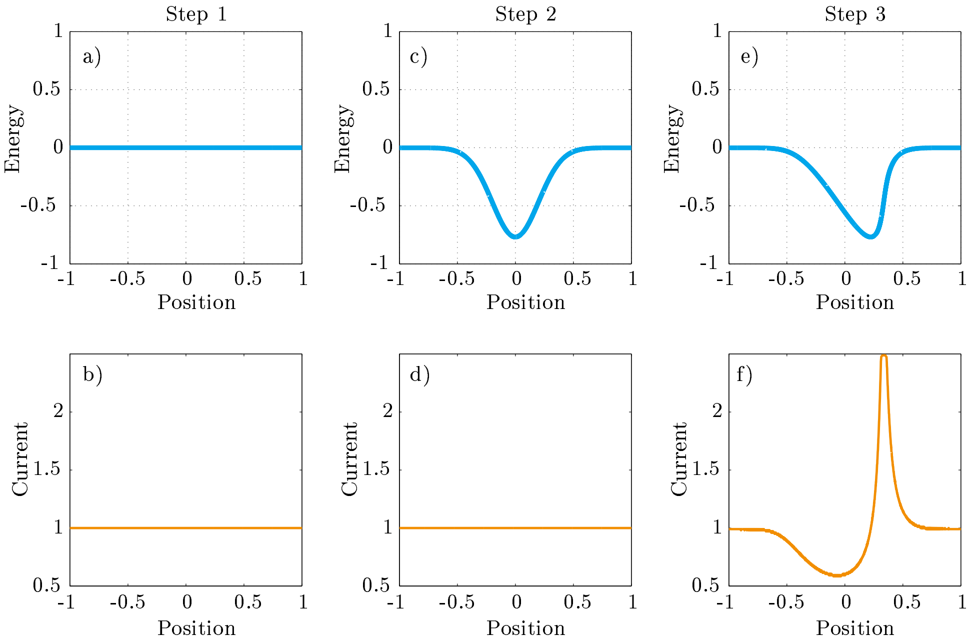

Figure 6.8.: Schematic drawings showing the modification of the longitudinal phase space and the current distribution of a rectangular distribution due to the CSR wake field and longitudinal dispersion. In step one (plots a and b) the particle distribution and the related current distribution are depicted. Step two (plots c and d) shows the same distribution after the modifications due to CSR and step three (plots e and f) presents the situation after the longitudinal displacement of the particles due to longitudinal dispersion. This leads to a modified current distribution as shown in plot f).

The conclusion of the simulations presented in figure 6.7 and 6.8 is that the mitigation of CSR effects is not only important to reduce the emittance growth in the bend plane, as it was mentioned before and as it will be discussed in the following section, but also to avoid or reduce the compression of the bunches in the extraction arc. Since the layouts of the two future beam lines FLASH1 and FLASH2 differ considerably (in FLASH1 there is just the chicane for the energy collimation and in FLASH2 there is the extraction arc with an overall deflection angle of 13.8 °), the bunch compression schemes have to be adapted accordingly.

6.4. Optimization of the Transverse Phase Space Evolution

A major requirement on the beam line layout of the extraction arc was to preserve the transverse emittances and beam sizes in order to provide the optimum electron beam quality for FEL operation. This implies several requirements on the beam optics which had to be achieved and which will be discussed in this section. It is a necessary condition for small beam sizes to have closed dispersions in both transverse planes and, for FLASH2, it is necessary to consider the dispersion up to the second order to obtain a good beam quality as it will be described below. Furthermore, it is essential to take appropriate measures to mitigate CSR and its impact on the horizontal phase space which will be described in the following.

The energy modification of the particles caused by CSR leads in the bending magnets to a transverse shift due to different deflections of the particles with different energies. This effect is demonstrated in figure 6.9 and this process is very similar to the compression of the bunches as presented in figure 6.8. The plots show the longitudinal phase space in the upper row and a top view of the particle's positions in the row below. Plot a) and b) represent the particle distribution before the impact of the CSR. The modification due to these effects are included in the plots c) and d) and one can see that the energy modification does not change the particle's positions. However, after passing a dispersive section, the energy modification causes a transverse translation of the particles. This process increases the projected emittance and beam size of a particle distribution.

Two different methods to mitigate CSR effects were mentioned in the chapters 3 and 4, the -I transfer matrix and the defined courses of the horizontal Twiss functions in the bending magnets. The former solution is widely used for extraction arcs in FELs, however, it turned out not to be practical for FLASH2. The spacial conditions require a tailor-made solution for the extraction arc and additional conditions given by demands on the transfer matrices or on the symmetry of the arc cannot be accomplished. For this reason, the expected CSR effects in the FLASH2 extraction arc will be mitigated using the method of the defined horizontal Twiss functions in the bends.

A large contribution to the CSR induced emittance growth is expected from the septum and the two bends at the end of the extraction arc because of their small bending radii. Consequently, the next paragraphs will describe these magnets. The impact from the weak reverse bend, the kickers and from the vertical bends is small and will be considered separately.

To investigate the dependence of the horizontal emittance growth due to CSR on the initial Twiss functions $\alpha_{x,in}$ and $\beta_{x,in}$ at the start of the bend, several simulations were

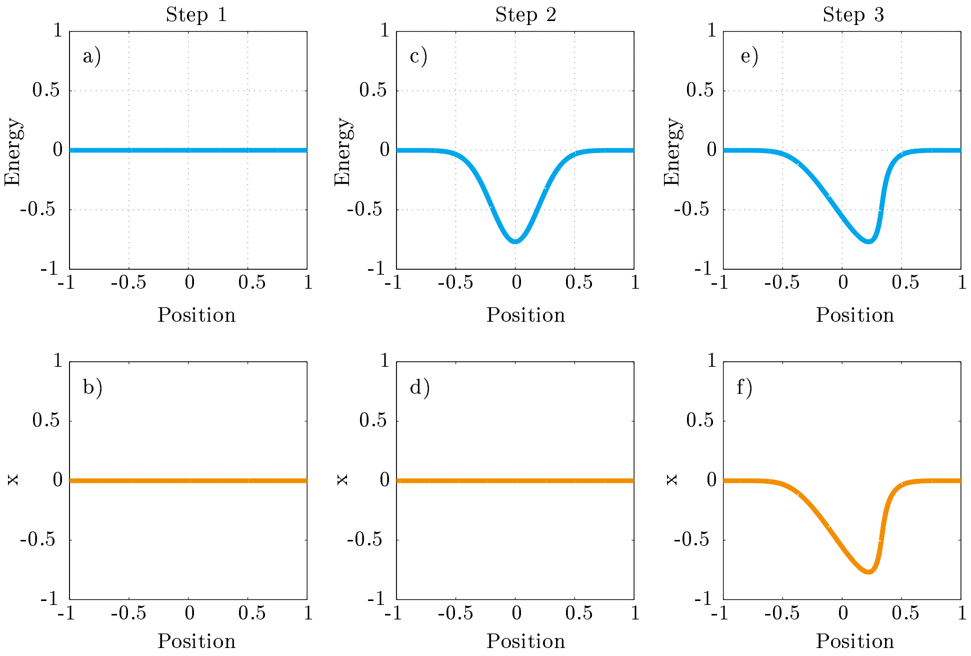

Figure 6.9.: Schematic drawings of the horizontal phase space's modifications due to CSR. Plot a) and b) show a rectangular particle distribution in the longitudinal phase space and a top view of these particles. The same distributions is presented in the plots c) and d) after the impact from CSR which changes the particle's energy but not their position. The last plots (e and f) represent the situation after a dispersive section where the horizontal positions are changed in accordance to the relative energy deviation of the particles.

carried out with different Twiss functions in order to find the best solution. The results of these simulations are presented in figure 6.10 where the normalized projected emittance behind the bending magnet is plotted as a function of $\alpha_{x,in}$ and $\beta_{x,in}$. These simulations were completed for the septum and for the two strong bends at the end of the arc. The applied bunch charges were 250 pC and 1 nC in order to cover the typical range of bunch charges in FLASH. Before the emittance size was calculated, the contributions from dispersion to the particle's positions and to their angles were calculated and subtracted.

Since the modifications due to CSR are not terminated at the end of the bending magnets, the emittances are analyzed at a position 1 m behind the bends where the wake field is reduced to approximately 10% of its maximum value (cf. chapter 3 and appendix A). The particle distributions used for these simulations were Gaussian shaped in both transverse and in the longitudinal plane and the parameters meet those of the bunches from start-to-end simulations. More information about the employed particle distributions is provided in section B.2.

With these simulation results, it is possible to determine the best setting of $\alpha_{x,in}$ and $\beta_{x,in}$ for the related magnets in order to minimize the emittance growth. However, the actual Twiss functions in the septum could not be achieved at the optimum position because further requirements had to be taken into account. Especially the position of the septum and the maximum strength of the surrounding quadrupoles prevented a better solution. Thus, the actual setting of the Twiss functions was a compromise between the named boundary conditions and the smallest possible emittance growth due to CSR. The feasibility of this setting will be presented in the following chapter dealing with the start-to-end simulations of FLASH2. In the case of the final horizontal bends, an optimum set of Twiss parameters could be achieved in spite of the fact that the course of the horizontal beta function is also constraint by the demands on a closed horizontal dispersion, which defines the strength of the upstream quadrupole magnets.

The orange marks in the plots show the positions of the actually set of Twiss functions at the start of the respective magnet as used in the FLASH2 arc. The ellipses around these marks represent the area with an mismatch of $m_p = \{1.1,\ 1.5,\ 2.0\}$ distinguished by the colors white, orange and red. The mismatch parameter describes the deviation of the Twiss parameters of the beam compared to the design Twiss parameters of the machine at the corresponding position in the beam line. Its definition and the derivation of the mismatch ellipses in the transverse phase space are presented in appendix D respectively in appendix E.

The demands on the course of the dispersion in the arc in order to achieve zero R_{56} prevented optimized Twiss functions in the reverse bend. Simulations were carried out for the reverse bend and no dependency between the initial Twiss functions and the projected emittance size could be found. This is also the case for the vertical kickers and for the vertical bending magnets which have both larger bending radii than the reverse bend.

The actual lattice of the extraction arc consists, among other elements, of a set of 21 quadrupole magnets of four different types positioned between the fast kickers and the undulator section. The chosen quadrupole distribution and the strength of these magnets fulfills all constrains given by the requirements on the beam quality and leaves enough

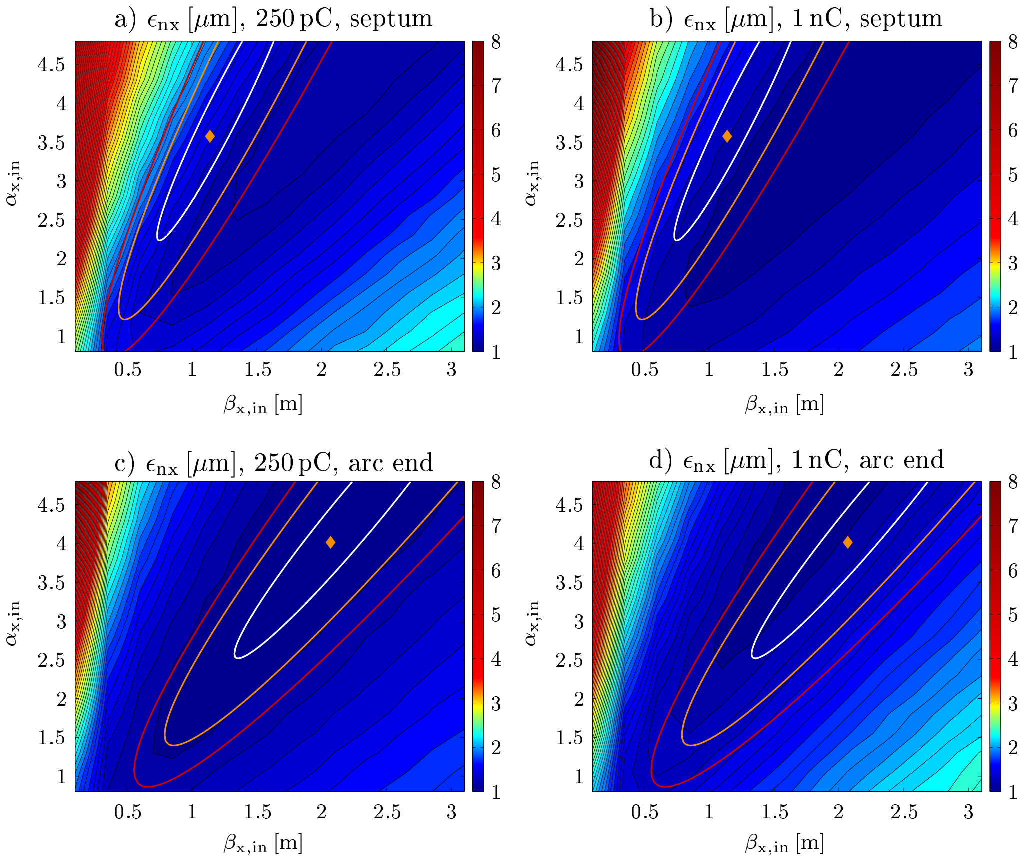

Figure 6.10.: This plots show the projected normalized emittance growth in the horizontal plane due to CSR effects in the septum (plot a and b) respectively in the final horizontal bends of the extraction arc (plots c and d) as a function of the initial Twiss parameters $\alpha_{x,in}$ and $\beta_{x,in}$ at the bend's entrance. The simulations were carried out for two different bunch charges, 250 pC presented in the plots a) and c) as well as for 1 nC shown in the plots b) and d). The orange marks show the actual Twiss functions in the particular magnets and the ellipses represent the areas with an mismatch parameter m_p of 1.1 (white), 1.5 (orange) and 2.0 (red).

space to implement further elements like diagnostic and vacuum components. The positions of all magnets are shown in figure 6.11. This top view of the extraction section shows the existing beam line (FLASH1), the extraction arc for FLASH2 and a possible extraction position and layout for a proposed third beam line (FLASH3). The grey lines represent the walls of the existing tunnel and of the new buildings housing the extraction arc respectively the new undulator beam line. A technical drawing of the extraction area is presented in figure F.1.

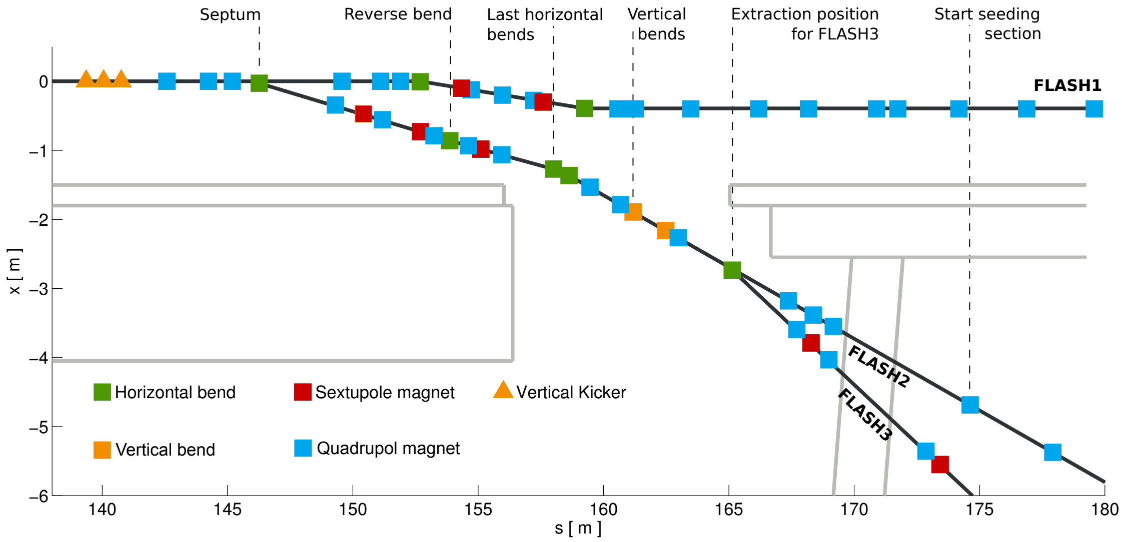

Figure 6.11.: Top view of the extraction arc for FLASH2 including the existing beam line (FLASH1) and a possible extraction solution for the proposed third beam line (FLASH3). The plot shows the section between the vertical kickers and the start of the seeding section in the FLASH2 beam line.

The related optics functions to this layout are presented in figure 6.12. All presented functions effect each other which will be briefly examined below. The beta functions are depicted in plot a), the transverse dispersion functions in plot b), plot c) shows the longitudinal dispersion and plot d) the vertical beam center offset. With an exception for the beta functions, those have been presented before but as mentioned above, they will be discussed again in order to show the interactions between them. The crucial positions along the extraction arc are marked with numbers S1-S9 facilitating the explanation.

- Position S1 shows the vertical kickers necessary for the beam offset in the Lambertson septum. In plot b) one can see that the vertical dispersion emerges at this position and the vertical beam center offset, presented in plot d), shows an increasing vertical offset also starting at this point.
- S2 marks the first quadrupole magnet out of three needed for the required Twiss functions in the septum. These quadrupoles are passed with an offset which causes a vertical deflection and changes the vertical and longitudinal dispersion (plots b and c) as well as the vertical beam center offset (plot d). The last quadrupole deflects the beam to a horizontal trajectory.
- The septum is located at S3 were a horizontal beam waist is required for CSR mitigation (plot a). The horizontal dispersion increases in the septum (plot b) and

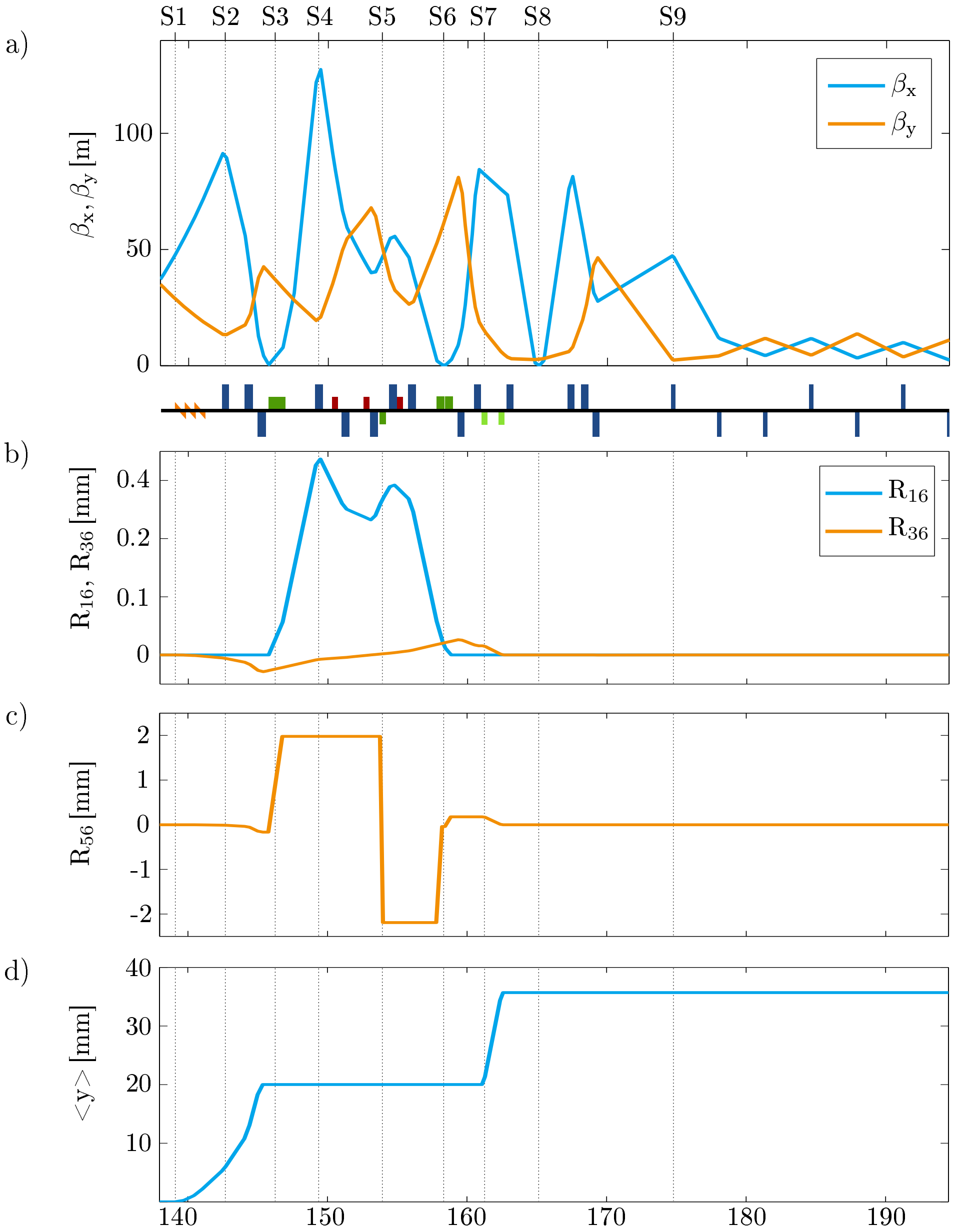

Figure 6.12.: The optics functions of the FLASH2 extraction arc. The beta functions are presented in plot a), plot b) shows both transverse dispersion functions, the longitudinal dispersion is presented in plot c) and the vertical beam center offset is presented in plot d). The crucial positions in the extraction arc are marked with numbers S1-S9. The color code used for the beam line elements is the same as before: orange for the kickers, blue for the quadrupoles, green for the bending magnets and the sextupole magnets are depicted in red.

this changes also the R_{56} as one can see in plot c). The vertical beam center offset is 2 cm as required for the extraction.

- The large horizontal beta function at S4 is a result of the beam waist in the septum and the fact that a certain drift space is necessary to separate the two beam lines of FLASH1 and FLASH2 before the next quadrupole can be installed.
- S5 represents the position of the reverse bend. The horizontal dispersion function was chosen as large as possible at this position (plot b) in order to increase the effect on the R_{56} (plot c).
- The course of the horizontal beta function at position S6 is optimized for CSR mitigation (plot a) and the two horizontal bending magnets at this position close the respective dispersion (plot b).
- The vertical dispersion (plot b) is closed by two vertical bending magnets shown at position S7. These magnets have also an impact on the R_{56} which is zero behind the second bend (plot c). In plot d) one can see that the overall vertical offset of the beam center is around 36 mm at the end of the extraction.
- The extraction position for the proposed third beam line was also considered during the development of the arc. At position S8 in plot a) one can find the horizontal beam waist which is necessary for CSR mitigation in this beam line.
- In plot a) at position S9 the start of the FODO structure of the FLASH2 seeding section is located. The first two quadrupoles are still used for the matching.

The overall beta functions starting at the electron gun's position are plotted in figure 6.13. The structure of the extraction arc (approximately between 140 m and 170 m) emerges clearly in comparison with the other parts of the machine. Especially the horizontal beta function is oscillating between very large and very small values to meet the given conditions.

The final layout of the extraction arc as presented above was chosen out of many different settings. The decision in favor of the presented layout was made on the basis of simulations with so called 3-σ-ellipses which are an indicator for the beam quality. More information about the 3-σ-ellipses will be presented in the following. As the name suggests, the particle distributions used for these simulations are ellipsoidal and envelop 3-σ of a particle distribution at the start position. The coordinates of the particles in

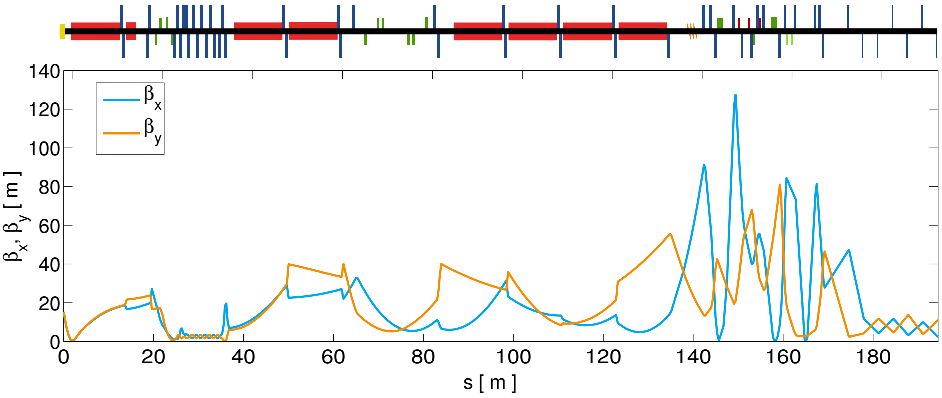

Figure 6.13.: The beta functions of FLASH2 starting at the electron gun and ending with the position of the first undulator. In this plot one can clearly see that the optics in the extraction section differs from the optics in the rest of the beam line. Especially the maximum horizontal beta function behind the septum stands out but it could not be avoided considering all boundary conditions. The schematic plot of the beam line uses the color code mentioned before. The accelerating modules, which are presented for the first time, are depicted in red.

the ellipses are calculated using the corresponding emittances of the beam and the Twiss functions of the machine:

$$\vec{x_0} = 3\sqrt{\epsilon_x\ \beta_{x,0}}\ \cos(\vec{n}) \tag{6.4}$$

$$\vec{x_0'} = -3\sqrt{\frac{\epsilon_x}{\beta_{x,0}}}\ (\alpha_{x,0}\cos(\vec{n}) + \sin(\vec{n})) \tag{6.5}$$

$$\vec{y_0} = 3\sqrt{\epsilon_y\ \beta_{y,0}}\ \cos(\vec{n}) \tag{6.6}$$

$$\vec{y_0'} = -3\sqrt{\frac{\epsilon_y}{\beta_{y,0}}}\ (\alpha_{y,0}\cos(\vec{n}) + \sin(\vec{n})) \tag{6.7}$$

With the physical emittance ϵ_i $(i = x, y)$, the related Twiss parameters α_i and β_i and with a vector $\vec{n}$ of evenly distributed numbers $n_j \in [0, 2\pi)$.

For a simulation with the 3-σ-ellipses as used for the beam quality tests, one needs six different particle distributions described in the six-dimensional phase space. In the first three distributions, the values for x and x' describe an ellipse in the horizontal plane whereas y and y' are zero. The longitudinal positions of all particles are the same and usually zero at the start. The differences between these three distributions is the momentum. The particles in the first ellipse have all the design momentum of the beam line p_0, the momenta of the two other ellipses deviate with a relative momentum deviation Δp, thus, they can be described with $p_0 \pm \Delta p$. The momentum variations are necessary to investigate chromatic effects and Δp is usually in the range of 1 %. The remaining three distributions are similar to those described above but now with the ellipses in the vertical plane given by the coordinates y and y'.

The plots of the ellipses are usually shown in a normalized phase space which is calculated using the machine's Twiss functions at the corresponding position. The following matrix equation shows how to calculate the particle's positions in the normalized phase space (η_j and η'_j) from the initial positions (j and j'). The Twiss parameters α_m and β_m are labeled with the index m to remind that these are the parameters of the machine and not of the particle distribution.

$$\begin{pmatrix} \eta \\ \eta' \end{pmatrix} = \begin{pmatrix} 1/\sqrt{\beta_m} & 0 \\ \alpha_m/\sqrt{\beta_m} & \sqrt{\beta_m} \end{pmatrix} \begin{pmatrix} j \\ j' \end{pmatrix} \tag{6.8}$$

In the normalized plots, a completely matched beam is shown as a perfect circle in the transverse phase space, thus, a mismatched distribution will be presented as an ellipse and the ratio of the ellipse's half-axes gives an indication of the mismatch described by the parameter m_p as defined in appendix D. Besides of beam mismatch, the 3-σ-ellipses simulations can also reveal a non closed dispersion. An ellipse with a momentum deviating from the design momentum will be shifted in x or x' (respectively in y or y') direction if that is the case. Depending on how the ellipses are shifted, it is possible to draw the conclusion what order of dispersion is causing this. Furthermore, any other form of distorted ellipses indicates usually a higher order effect caused by too strong magnets (collective effects are not used in these simulations) and has to be investigated.

The 3-σ-ellipses-simulations for FLASH2 started always behind the last accelerating module of the linac and ended at the beginning of the undulator section. The seeding section was included because the first quadrupoles in this FODO lattice are still necessary for the matching to the periodic structure. The plots in figure 6.14 show the results of the first simulation with $\Delta p = 1\%$. This range was chosen because it is the maximum energy deviation within a bunch due to the energy chirp (cf. the typical bunches in FLASH2 as presented in appendix B).

What becomes immediately apparent assessing the results from the first simulation is the

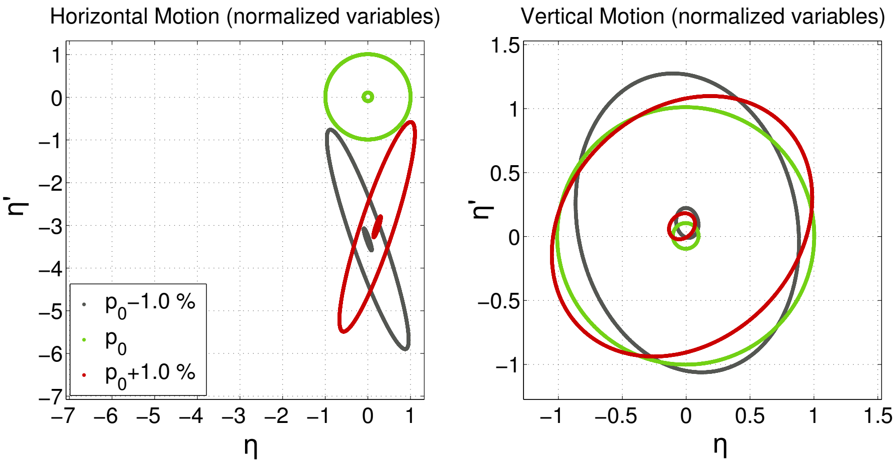

Figure 6.14.: The results from the first simulations with 3-σ-ellipses and $\Delta p = \pm 1\,\%$. In the left plot one can find the results for the horizontal plane and in the right plot those for the vertical plane. The green ellipses represent the distribution with design momentum, the dark-grey ellipses show the particles with $\Delta p = -1\,\%$ and the red ellipses the distribution with $\Delta p = +1\,\%$. The small ellipses in the center represent the 0.3-σ-ellipses which help to indicate centroid shifts.

massive centroid shift of the ellipses with energy deviations in the horizontal plane. Considering the fact that the first order dispersion is closed in this section (cf. figure. 6.12) and that the ellipses with positive and negative Δp are shifted in the same direction, this indicates a none closed second order dispersion. To verify this, the course of the second order dispersion is plotted in figure 6.15.

As presumed, the T_{166} (or second order dispersion) is not closed over the extraction arc. Three sextupole magnets were installed in the beam line to close the T_{166} at the end of the beam line. Due to the fact that the centroid shift only appears in the horizontal plane, the sextupole magnets are at positions with large horizontal dispersion to strengthen the effect on that plane. The positions and strengths of the sextupole magnets were optimized using `Elegant`. The second order dispersion after the correction with the three sextupole magnets is presented in figure 6.16. After the correction of the T_{166}, a second simulation using 3-σ-ellipses was carried out and the results are presented in figure 6.17.

The centroid shift in the horizontal plane is suppressed almost completely and also the deformations in both planes caused by chromatic aberrations are less than before. The stronger modification in the horizontal plane, in comparison with the vertical plane, can be explained with the strong horizontal focusing quadrupole magnets at positions with

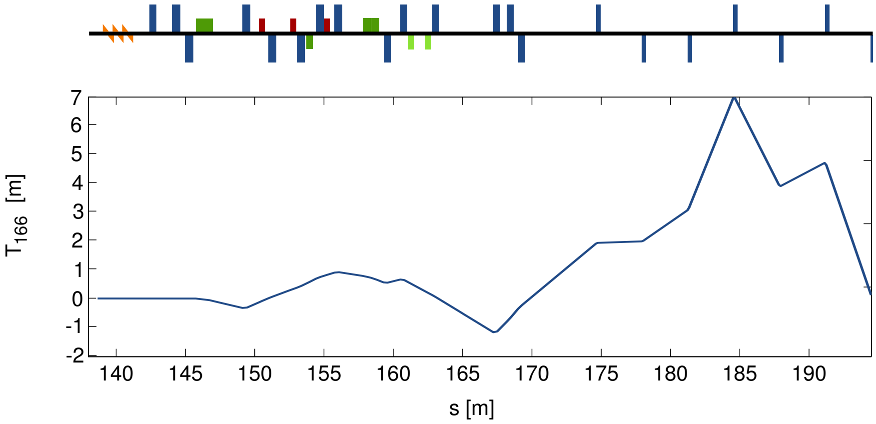

Figure 6.15.: The horizontal second order dispersion in the extraction arc was not closed at this juncture of the lattice development.

large horizontal beta functions like the quadrupole behind the septum. As mentioned before, the Twiss functions in the septum are fixed in order to mitigate CSR and in combination with the necessary drifts space between the septum and the following elements to separate the beam lines, this leads to the large beta function, thus, the larger impact from the strong quadrupoles on the horizontal plane cannot be reduced without increasing the effects caused by CSR. However, it will be shown in chapter 7 on the basis of start-to-end simulations that this beam quality is sufficient for FEL operation in FLASH2. The mismatch parameters m_p for all ellipses used in these simulations are listed in table. 6.1.

Table 6.1.: The mismatch parameters for the 3-σ-ellipses simulation in the FLASH2 extraction arc with $\Delta p = 1\,\%$ and including sextupole magnets to close the second order dispersion.

m_p	p_0	$p_0 + \Delta p$	$p_0 - \Delta p$
Horizontal plane	1.0	2.4	2.5
Vertical plane	1.0	1.1	1.1

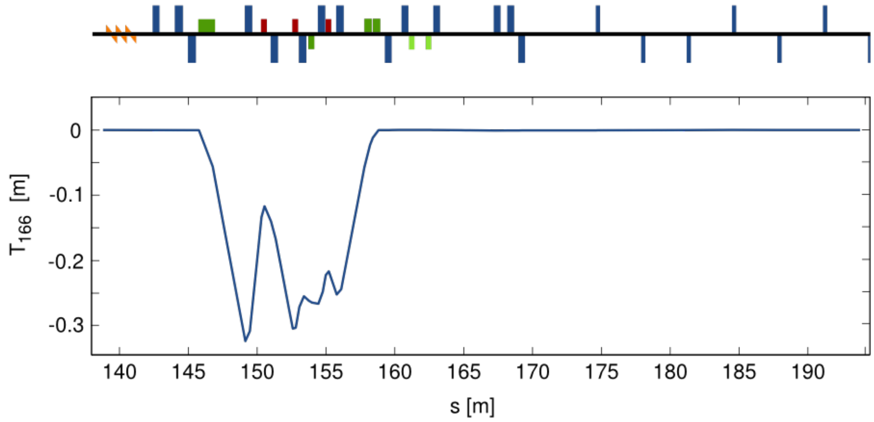

Figure 6.16.: The second order dispersion after the correction with three sextupole magnets in the extraction arc.

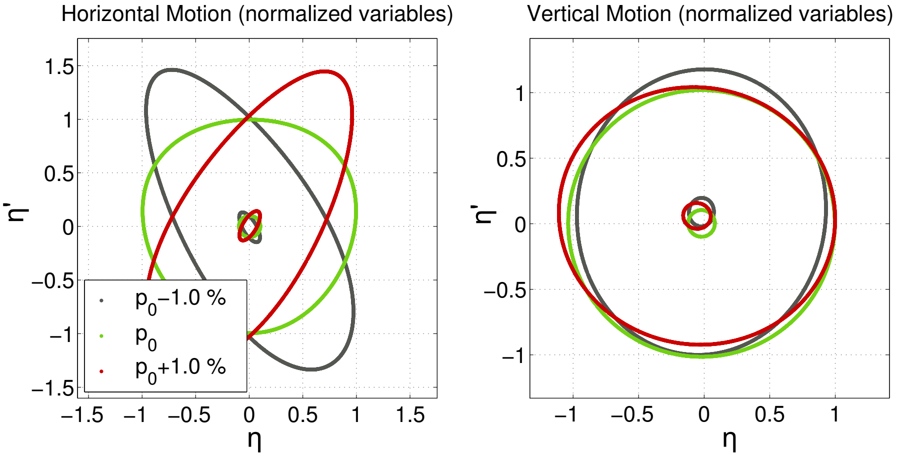

Figure 6.17.: The results from simulations with 3-σ-ellipses and ±1 % energy deviation. In the left plot one can find the results for the horizontal plane and in the right plot those for the vertical plane. These simulation results were obtained after the correction of the second order dispersion in the FLASH2 extraction arc. The sextupole magnets did also reduce the chromatic aberrations which results in smaller deformations of the ellipses. The green ellipses represent the distribution with the design energy of the arc, the dark-grey ellipses show the distribution with −1 % and the red ellipses the distribution with +1 % energy deviation. The small ellipses in the center show the 0.3-σ-ellipses which help to evaluate centroid shifts.

So far, the FLASH2 beam line layout was designed under consideration of the extraction to the proposed third beam line (FLASH3). For this reason, there is an additional horizontal beam waist between the vertical bending magnets and the seeding section of FLASH2 (cf. figure 6.12, plot a), position S8). Since the FEL will start in 2014 without this additional beam line and since the strong quadrupole magnet necessary for this beam waist causes further impairment of the beam quality, a beam optics solution was developed neglecting the FLASH3 extraction. The magnet positions for this solution are the same as presented before but the magnetic fields are smaller in order to improve the beam quality in the undulator beam line of FLASH2. This solution is presented in figure 6.18.

The 3-σ-ellipses simulations for this setting are presented in figure 6.19. As one can see, the optics without the additional beam waist has much less impact on the horizontal ellipses and in spite of the fact that the mismatch in the vertical plane is a little larger, the overall result is better than before. For this reason, it is conceivable to start FLASH2 with this optics until the additional extraction position is required. The related mismatch parameter for these ellipses are presented in table 6.2.

The beam optics for this solution is the same up to the last quadrupole magnet upstream the extraction position of FLASH3 and this quadrupole is the only necessary element to obtain the beam waist for the CSR mitigation in FLASH3. The additional beam optics was designed such that this quadrupole can be set to zero for the FLASH2 operation. For this reason, there is now also the possibility to install (if requested) a pulsed quadrupole magnet for the FLASH3 operation at this position which can then be switched between the necessary strength for the extraction to FLASH3 and an off-setting for the FLASH2 beam line preserving the good beam quality as represented in figure 6.19. If the pulsed quadrupole can provide a sufficient field quality, this solution would not have any disadvantages for the third beam line but it would improve the beam quality in FLASH2 significantly.

Table 6.2.: The mismatch parameters for the 3-σ-ellipses simulation in the FLASH2 extraction arc with $\Delta p = 1\,\%$ using the beam optics without a beam waist for the extraction of the proposed third beam line.

m_p	p_0	$p_0 + \Delta p$	$p_0 - \Delta p$
Horizontal plane	1.00	1.20	1.22
Vertical plane	1.00	1.47	1.38

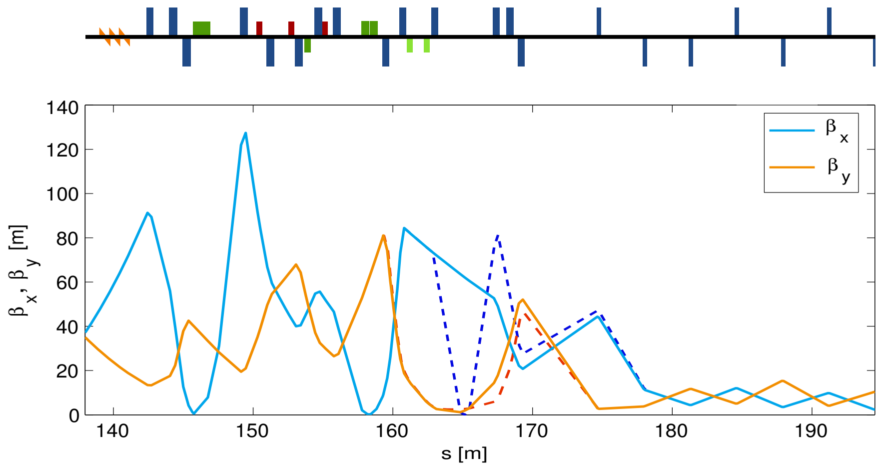

Figure 6.18.: The courses of the beta functions of a beam optics solution without the additional beam waist at the extraction position for the proposed third beam line. The optics is the same as before up to the extraction of FLASH3 and all magnets have the same positions. The dashed lines represent the beta functions as presented before including the beam waist at the additional extraction point. In the following seeding section, the courses of the beta functions of both optics solutions are the same.

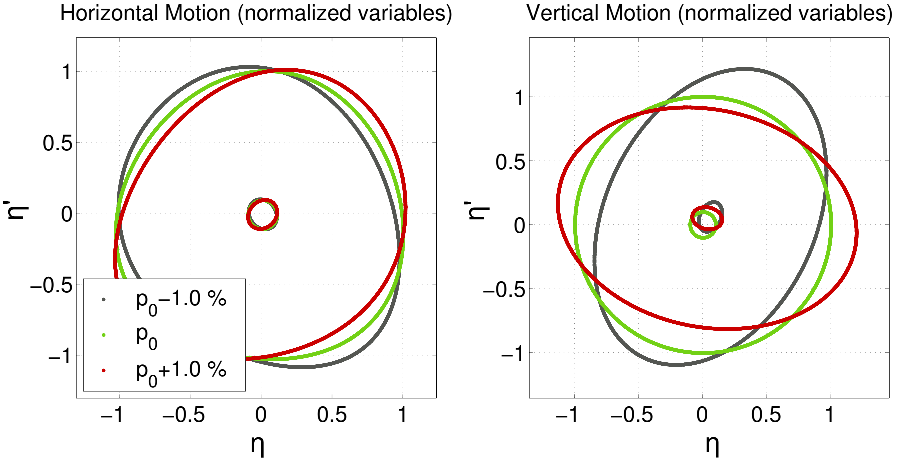

Figure 6.19.: The 3-σ-ellipses for the beam optics without a beam waist for the proposed third beam line. The mismatch due to chromatic aberrations of the particle distributions with an energy deviation of 1 % is smaller for this optics solution compared with the standard solution including the FLASH3 extraction. The values of the associated mismatch parameters are presented in table 6.2.

A mismatch of the particle distribution at any position in the lattice leads to a perturbed beta function $\tilde{\beta}_s$ in the following beam line which oscillates around the unperturbed beta function β_s. The amplitude of the oscillation is called the mismatch amplitude (cf. equation D.20)

$$\lambda_{\mathrm{mp}} = m_p + \sqrt{m_p^2 - 1}. \tag{6.9}$$

The following inequation describes the oscillation range of the deteriorated beta function $\tilde{\beta}_s$ (cf. equation D.21):

$$\frac{1}{\lambda_{\mathrm{mp}}} \beta_s \;\leq\; \tilde{\beta}_s \;\leq\; \lambda_{\mathrm{mp}} \beta_s. \tag{6.10}$$

Figure 6.10 presented the areas for mismatched Twiss functions for three different mismatch parameters $m_p = \{1.1,\ 1.5,\ 2.0\}$ and one can see how small these areas are. During the operation of the machine, it cannot be guaranteed that the design Twiss parameters can always be matched, especially at crucial positions e.g. at the entrance of the septum where a small beta function is required. A mismatch of $m_p = 1.1$ or even higher cannot be excluded completely. It was explained that this will lead to an increased horizontal emittance due to CSR effects in the septum, but in addition, the mismatch will be propagated along the lattice where it will potentially deteriorate the electron beam further. The plots in figure 6.20 show the possible propagation range along the extraction arc of a mismatched beam with $m_p = 1.1$. One can see that the maximum beta function can grow up to 200 m at the position of the first quadrupole downstream the septum. This quadrupole is one of the strongest in the lattice which will lead, in combination with the much higher beta function, to more chromatic aberrations and thus to further deterioration of the beam quality. Furthermore, the changed average beta function in the undulator will also lead to limitations for the FEL operation (cf. chapter 2). This investigations make clear that a matched beam, especially at the crucial positions, is important for the operation of the new beam line FLASH2. For this reason, there will be the possibility to measure the beam parameters in the FLASH2 beam line.

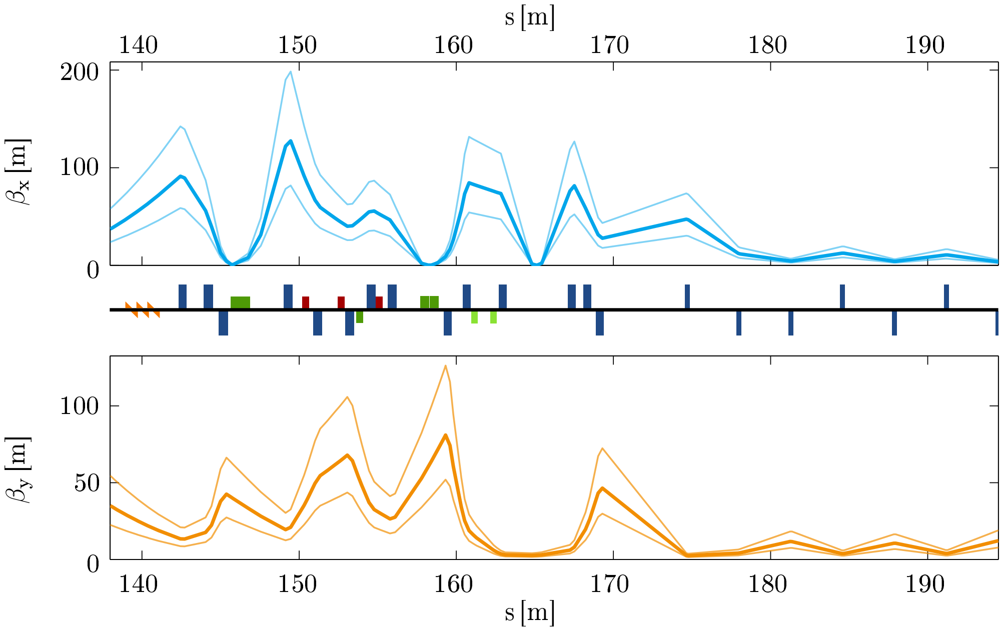

Figure 6.20.: The range of the mismatch amplitude for a mismatch parameter $m_p = 1.1$ along the extraction arc. A small deviation in at least one of the two Twiss parameters can lead to large deviations of the beta functions at a following positions. The upper plot shows the mismatch amplitude for the horizontal plane and the lower plot for the vertical plane.

7. FLASH2 Start to End Simulations

7.1. Introduction

In this chapter, the results from start-to-end simulations for FLASH2 will be presented for four different particle distributions with charges of 100 pC, 250 pC, 500 pC and 1 nC with an energy of 1 GeV (cf. appendix B). The applied programs for the particle tracking in the linac were CSRtrack [29], used for the two bunch compressors and Astra [34], used for all straight sections. These particle distributions, especially their shape in the longitudinal phase space, are optimized for the FLASH2 beam line and the impact from the extraction arc on the particle distributions was considered.[1] However, a perfect adaption of the bunches with 100 pC and 250 pC could not be achieved because the gradient of the third harmonic acceleration module reached its maximum. The resulting consequences will be discussed in the respective sections.

The start-to-end simulation for each bunch charge will be presented in two stages: firstly the results from the particle tracking through the extraction arc and secondly, the results from the FEL simulations. The particle tracking through the extraction arc was carried out with CSRtrack in order to describe the occurring CSR effects comprehensively. The resulting particle distributions were used for SASE FEL simulations with Genesis [30]. These simulations were performed in order to assess if the design of the FLASH2 extraction arc is sufficient for FEL operation or not. For all bunch charges, the Genesis simulations were carried out 150 times and each run with a different seed for the simulation of the SASE process. This makes it possible to study the power fluctuations and it allows to calculate an average power distribution along the bunches which is more realistic than the distribution from a single shot simulation. The same applies for the radiated wavelength.

It was mentioned in chapter 4 that about one third of the experiments at FLASH use a photon wavelength around 13.5 nm and for this reason, the main focus of the FEL simulations was on this wavelength. In order to obtain this wavelength with a 1 GeV

---

[1] Courtesy of G. Feng who provided the particle distributions.

beam, the rms undulator parameter has to be $K_{\mathrm{rms}} = 1.51$ which corresponds in FLASH2 with an undulator gap of approximately 11.3 mm. One additional set of simulations was carried out using the maximum FLASH2 undulator gap size of 18 mm (corresponding to a rms undulator parameter of $K_{\mathrm{rms}} \approx 0.69$.) in order to verify the usability of the extraction arc also for smaller wavelength. This simulation was executed for the 250 pC bunch with a beam energy of 1 GeV. This undulator setting and the named beam parameters lead to a photon wavelength of about 6.1 nm.

7.2. Start-to-End Simulations Using a 100 pC Bunch

7.2.1. Particle Tracking Through the Extraction Arc

The 100 pC bunch is one of the smallest bunches in FLASH and its strong compression, which is necessary to obtain a peak current above 2 kA as required for SASE operation, leads to a high charge density and thus to strong space charge effects. The short bunch length leads also to stronger CSR effects in the extraction arc, thus, extracting the 100 pC bunch is expected to be more demanding than extracting bunches with higher charges.

Figure 7.1 shows plots of the 100 pC bunch at the end of the linac (on the left hand side) and at the start of the FLASH2 undulator section (on the right hand side). Plot a) and b) represent the longitudinal phase space, in plot c) and d), one can find the current distribution and in plot e) and f), the normalized transverse slice emittances are presented. It is apparent that the impact from the extraction arc changes the particle distribution in the longitudinal phase space, especially the energy spread increases strongly (plot b). It was mentioned in the introduction that the compression of the 100 pC bunches could not be adapted perfectly to the demands of the FLASH2 beam line and this leads to a peak current of about 4 kA at the position of the first undulator (plot d). The cause of this compression was described in chapter 6.3. In plot f), showing the normalized emittances at the end of the extraction arc, one can see that the vertical emittance grows only partially in the bunch head but the horizontal emittance increases over the complete bunch length and reaches a maximum value of approximately 2.3 μm. These results are mirrored in the results for the normalized projected emittances, calculated for the bunch core containing 90 % of the particles. The projected horizontal emittance grows by approximately 51 %, starting at 0.87 μm rad and the vertical counterpart is stable around 0.7 μm rad (cf. figure B.1 and B.2).

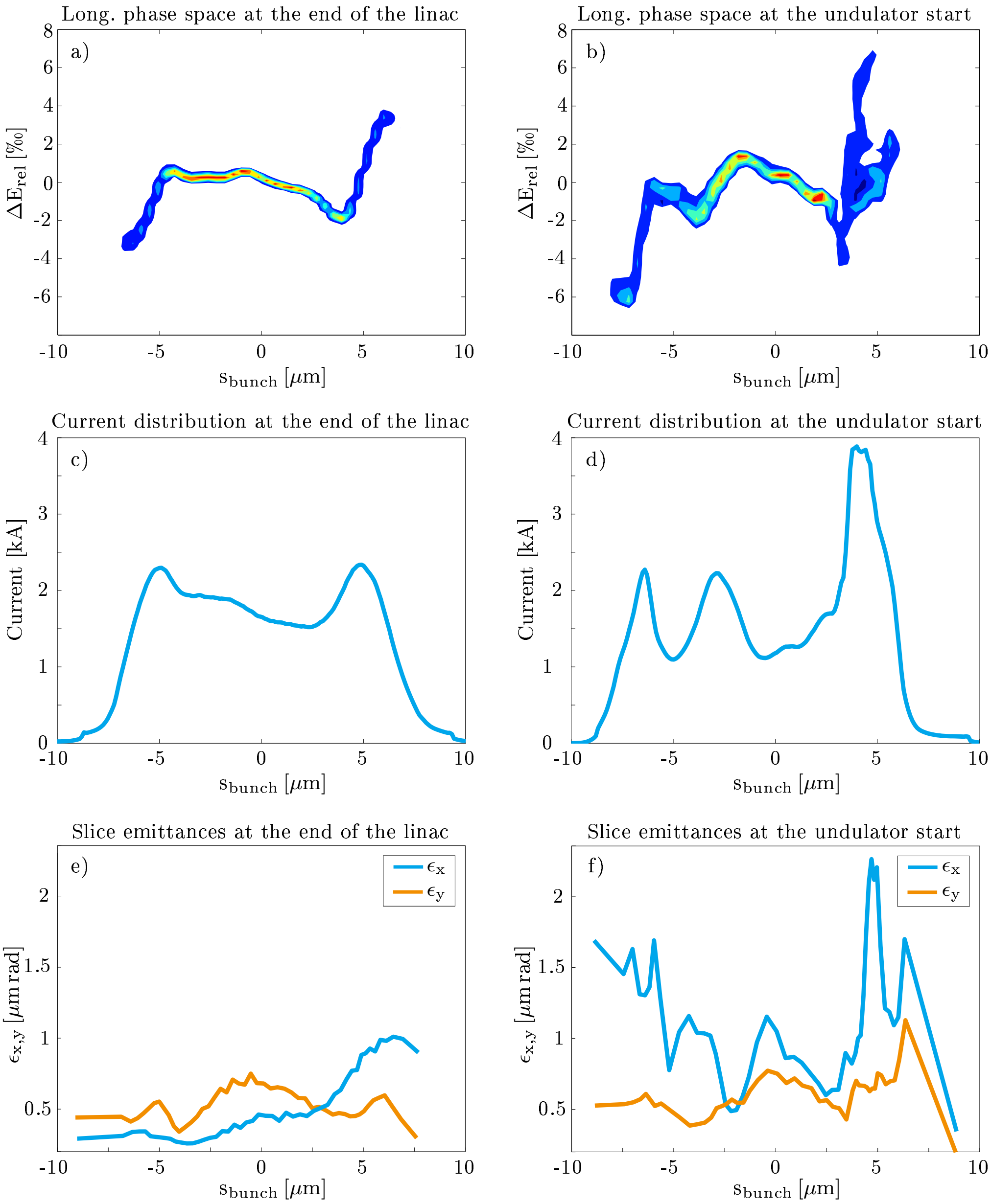

Figure 7.1.: The plots on the left hand side describe the 100 pC bunch at the end of the FLASH linac and the plots on the right hand side represent the same parameters at the end of the extraction arc. Plot a) and b) show the longitudinal phase space, plot c) and d) the current distribution and plot e) and f) show the normalized transverse emittances.

The short length and the high current density makes it difficult to transport this particle distribution through the extraction arc to the undulators of FLASH2. A strong impact from CSR was expected and the results presented in figure 7.1 confirm these assumptions. FEL simulations will now have to show whether this bunch can be used for FEL operation or not.

7.2.2. FEL Simulations

In figure 7.2 on can find the FEL simulation results for the 100 pC bunch. Plot a) shows the particle distribution in the longitudinal phase space and plot b) presents the development of the radiation power along the undulator.[2] The blue line shows the average value of the 150 seeds and the orange area represents the total power spread at the corresponding undulator positions. The saturation power of around 15 GW is reached after the first half of the 38.3 m long undulator section and the data for the following plots were taken at approximately this position. Plot c) shows the radiation power distribution of the bunch after 22.14 m in the undulator section. What becomes immediately apparent is that the bunch radiates at two different positions, a first peak appears in the center of the presented range and the second peak appears at about 5 μm. The distance between these peaks is in accordance with the distance between the second and third peak of the current distribution. The FWHM of the radiation peak in the center is approximately 3.3 μm and the FWHM of the peak on the right hand side is around 1 μm. In plot d), one can see the spectrum of the emitted radiation. The peak of the average power (represented by the blue line) is localized at a wavelength of 13.40 nm as expected and the FWHM of the spectrum is about 0.1 nm (this corresponds roughly to a relative spectral width of 0.75 %).

The conclusions concerning the start-to-end simulation using the 100 pC bunch are, that, in spite of the bunch's modifications due to CSR in the extraction arc, the electron beam quality is sufficient for SASE FEL operation and the obtained saturation power is within the bounds of the expected range. However, the double peak of the power distribution, originated by the various peaks of the current distribution differs from the ideal case. Eventually a further optimization of the compression scheme can reduce or prevent this effect.

---

[2] This plot shows the maximum radiation power at the concerning undulator position, regardless of its position in the bunch. For this reason, the values for the radiation power are larger than those presented in plot c).

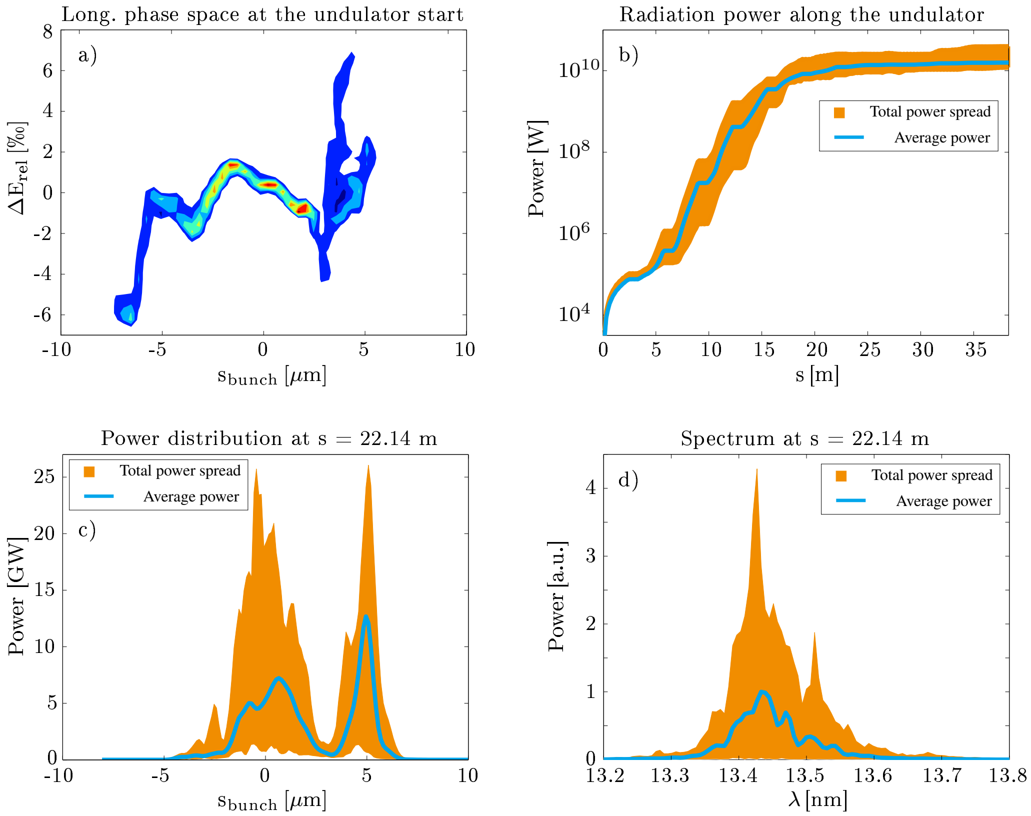

Figure 7.2.: These plots show the results from the FLASH2 SASE FEL simulations using the 100 pC bunch. In addition, the longitudinal phase space of the applied particle distribution is presented in plot a). In plot b), one can find the development of the radiation power along the undulator and plot c) shows the radiation power distribution over the bunch at an undulator position of 22.1 m. Plot d) presents the spectrum of the emitted radiation with a peak around 13.45 nm.

7.3. Start-to-End Simulations Using a 250 pC Bunch

7.3.1. Particle Tracking Through the Extraction Arc

For the 250 pC bunch, the impact from CSR is expected to be smaller than for the 100 pC bunch but due to the fact that this bunch is also very short, (the FWHM is approximately 24 μm, cf. figure B.3) there will be as well significant modifications. The results of the particle tracking simulation through the FLASH2 extraction arc are presented in figure 7.3. The arrangement of these plots in this figure is the same as in the corresponding figure for the 100 pC bunch and the plots on the left hand side represent the longitudinal phase space (plot a), the current distribution (plot c) and the normalized transverse slice emittances (plot e) at the end of the FLASH linac. The plots on the right hand side show the same parameters but for the particle distribution at the start of the undulator section.

The distribution in the longitudinal phase space shows on the one hand the typical energy chirp of the FLASH bunches but one can also see a deviation from the linear chirp in the bunch center which indicates the impact from space charge effects in the linac. The bunch modification due to CSR in the extraction arc, as presented in the longitudinal phase space in plot b), is much more apparent. The expected reduced energy in the bunch center is clearly visible and the slightly increased particle's energy in the bunch head (cf. figure 3.3) is also shown.

The unfavorable interaction between the energy modification due to CSR and the dispersion of the extraction arc was already addressed while discussing the modifications of the 100 pC bunch's current distribution. The same effect appears also in the results of the 250 pC bunch. The peak current, as presented in plot d), raises up to almost 4 kA which involves increased space charge effects at this position.

The impact of the extraction arc on the slice emittances is smaller than for the last bunch. The vertical slice emittance does change hardly and the main modification of the horizontal slice emittance is limited to the bunch center. The projected vertical emittance is stable around 0.74 μm rad and the horizontal projected emittance growth moderately by 9.2 % starting at 0.87 μm rad (cf. figure B.3 and B.4).

Summarizing the results from the particle tracking simulation of the 250 pC bunch through the extraction arc, one can say that the impact on the bunch is, especially in the longitudinal phase space and in the current plot, clearly visible but the small slice emittances and the belonging projected parameters look promising for the FEL simulations.

7.3.2. FEL Simulations

The 250 pC bunch was used for SASE FEL simulations with two different wavelengths of 6 nm and 13.5 nm whereof the latter one will be discussed first. The results of this FEL simulations are presented in figure 7.4. In plot a), one can find the longitudinal phase space of the related particle distribution which was also presented in the last figure. Plot b) shows the evolution of the radiation power along the undulator. The maximum value

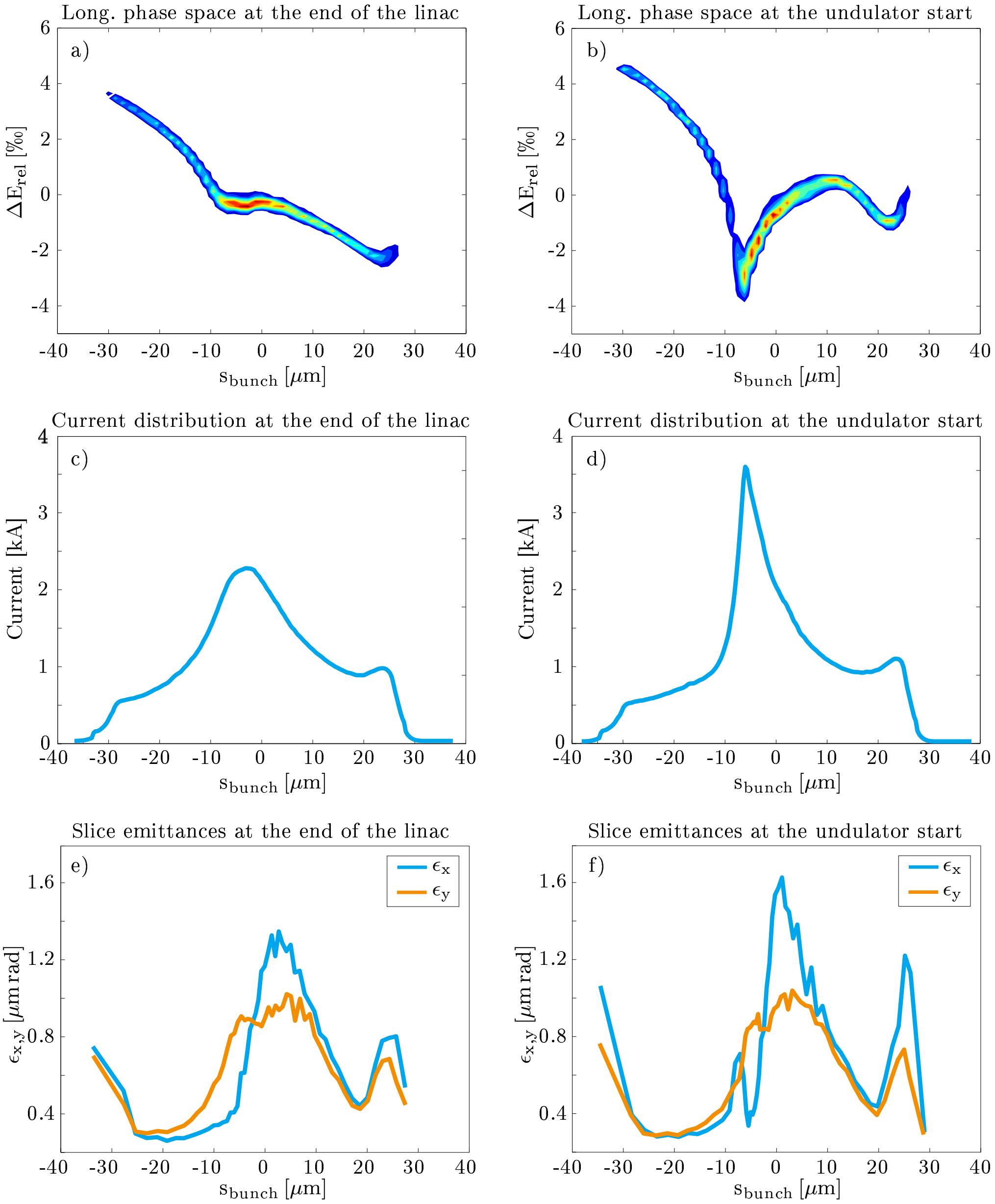

Figure 7.3.: The plots on the left hand side represent the 250 pC particle distribution at the end of the linac and the plots on the right hand side represent the same bunch at the end of the extraction arc. Plot a) and b) show the longitudinal phase space where one can see the impact of the CSR effects in the arc on the particle's energy. In plot c) and d), one can find the current distributions and the last plots, e) and f), show the normalized slice emittances.

of the blue line, representing the average for all simulations with different seeds, at the end of the undulator section is 50 GW. Saturation is reached after approximately one third of the undulator section's length. The data for plot c), showing the radiation power distribution along the bunch and plot d), where one can find the spectrum of the emitted radiation, was taken at an undulator position of 20.10 m.

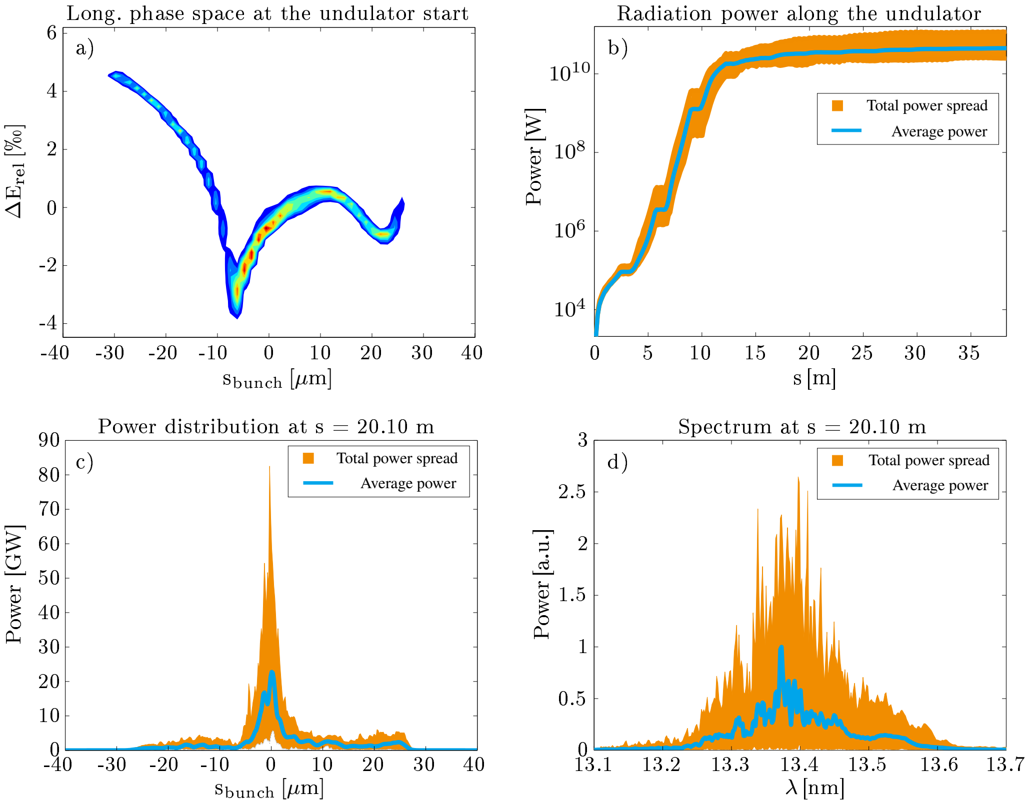

Figure 7.4.: In this figure, the results of the FEL simulations with a photon wavelength of 13.5 nm emitted by the 250 pC bunch are presented. Plot a) shows the longitudinal phase space of the particle distribution. Plot b) represents the evolution of the radiation power along the undulator and plot c) shows the distribution of the radiation power along the bunch. In plot d) one can find the spectrum of the emitted radiation.

The radiation power distribution along the bunch shows a single peak with a FWHM of approximately 3 μm located in the center of the presented range. The slippage length[3]

---

[3] Since the photons travel on a direct trajectory through the undulator and the electrons follow their sinusoidal path due to the alternating magnetic field, the longitudinal velocity of the electrons is noticeably smaller than the speed of light. This leads to a growing distance between the photons and

at this undulator position is about 8.8 μm, thus the peak of the radiation distribution matches with the peak of the current distribution as presented in figure 7.3, plot d). It is also apparent that only this bunch area radiates. The spectrum of the simulation is presented in plot d) and shows a peak close to 13.4 nm and a FWHM of almost 0.1 nm (this corresponds roughly to a relative spectral width of 0.75 %).[4]

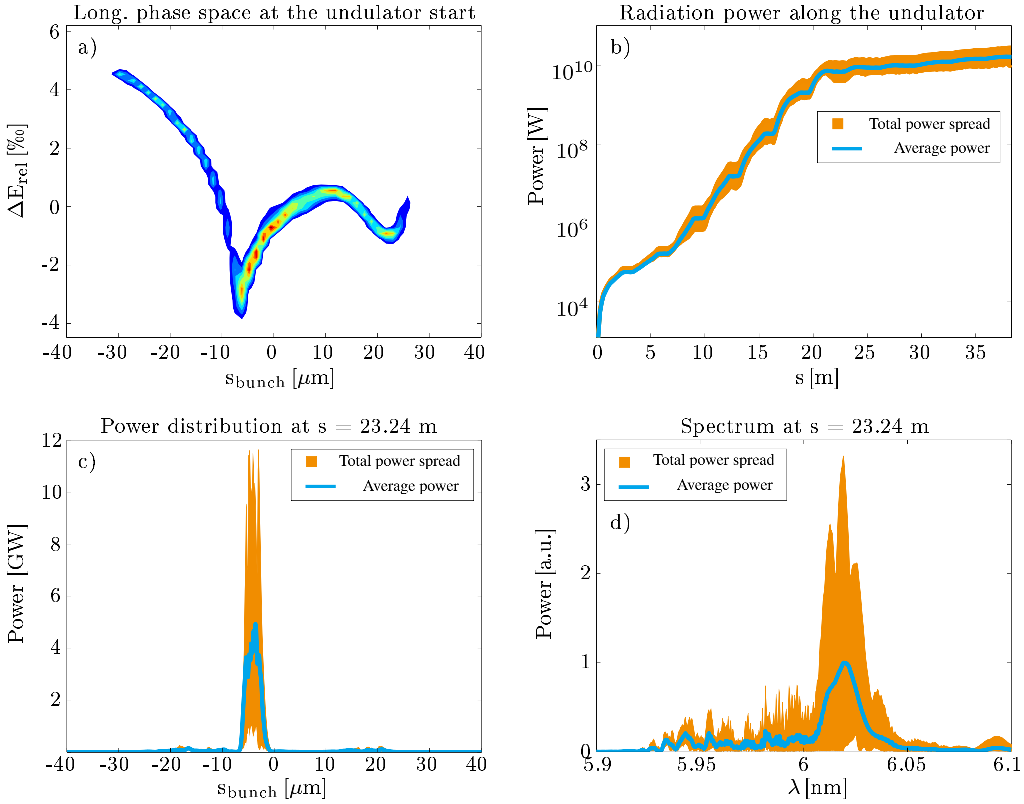

Figure 7.5.: This plots show also FEL simulation results obtained with the 250 pC bunch but at a wavelength of 6 nm. Plot a) represents the longitudinal phase space of the bunch, plot b) shows the evolution of the radiation power in the undulators. Plot c) and d) present the power distribution along the bunch respectively the spectrum of the FEL radiation.

---

the electrons which emitted them. The distance grows with each undulator period by one photon wavelength.

[4] This spectrum shows a greater fluctuation than the spectrum in figure 7.2. The deviation can be explained with the different simulation settings. The relative resolution of the 100 pC simulation was smaller than the relative resolution for the 250 pC simulation. This was necessary to limit the required computing time. For a processes like this, with 150 individual seeds, the computing time plays a large role even when 100 - 200 CPUs are used in parallel.

The results from this FEL simulation at 13.5 nm fulfills the expectations. The radiation power reaches saturation very early and its maximum is larger than expected. The bunch radiates only at the position of the high peak current and the spectrum is as expected for these simulations.

We will continue with the same particle distribution but with a different rms undulator parameter $K_{\mathrm{rms}} = 0.69$ and thus with a different wavelength of the emitted radiation of 6.1 nm. The belonging results from this simulation are presented in figure 7.5.

The arrangement of the plots is the same as in the FEL simulation figures before. The longitudinal phase space is presented in plot a) and the evolution of the radiation power in the undulator section is presented in plot b), where one can see clearly that it takes a longer distance, in comparison with the simulation at 13.5 nm presented in figure 7.4, until the radiation power reaches saturation. As it was discussed in chapter 2 using the one dimensional FEL theory the proportionality between the gain length and the undulator parameter is

$$L_{\mathrm{g0}} \propto K^{-\frac{2}{3}}, \tag{7.1}$$

thus, the ratio of the required distances in the undulator to achieve saturation power for the 6 nm and the 13.5 nm case can be calculated as follows:

$$\frac{L_{\mathrm{s}\ 6\,\mathrm{nm}}}{L_{\mathrm{s}\ 13.5\,\mathrm{nm}}} = \left(\frac{K_{6\,\mathrm{nm}}}{K_{13.5\,\mathrm{nm}}}\right)^{-\frac{2}{3}} = \left(\frac{1.51}{0.69}\right)^{-\frac{2}{3}} \approx 1.7. \tag{7.2}$$

According to the one dimensional FEL theory, the required length to reach saturation at 6 nm has to be about 1.7 times longer than the required length at a wavelength of 13.5 nm. This calculation is in accordance with the results presented in plot b) in figure 7.4 respectively in figure 7.5. The required distances to reach saturation presented in the plots are approximately $L_{\mathrm{s}\ 13.5\,\mathrm{nm}} = 12\,\mathrm{m}$ for the 13.5 nm case and $L_{\mathrm{s}\ 6\,\mathrm{nm}} = 21\,\mathrm{m}$ for the 6 nm case, thus, their ratio is 1.75.

We continue with the results presented in 7.5, plot c), where one can find the radiation power distribution along the 250 pC bunch. It shows a narrow peak at $-3\,\mu$m with a FWHM of about $3\,\mu$m. In plot f), showing the spectrum of the simulation, one can see that the peak is at a wavelength of almost 6 nm and the FWHM of this plot is 0.02 nm which corresponds approximately to a relative spectral width of 0.33 %.

The comparison of the two simulations with a wavelength of 13.5 nm respectively with a wavelength of 6 nm is in accordance with the FEL theory. The distribution of the radiation power shows that only the particles at the position of the peak current radiate. The spectrum obtained in the simulation meets the expectations.

7.4. Start-to-End Simulations Using a 500 pC Bunch

7.4.1. Particle Tracking Through the Extraction Arc

It is expected that the simulations with a higher bunch charge, like the 500 pC bunch which is of concern in this section, show less impact due to the CSR and space charge effects. These assumptions are confirmed by the particle tracking simulation results as presented in figure 7.6. All plots on the left hand side show the bunch parameters at the end of the linac and the the plot on the right hand side the same particle distribution at the end of the extraction arc, which is also the position where the first undulator starts. Plot a) shows the longitudinal phase space and it is obvious that the modification of the bunch in the FLASH linac is much smaller than it was for the other bunches presented so far. However, the CSR effects in the extraction arc have change also this particle distribution as one can observe in plot b). The characteristically modification of the particle's energy in the bunch center is clearly depicted.

The peak current downstream the extraction arc of FLASH2, presented in plot d) is slightly increased but the maximum value is small compared with the modifications of the bunches with smaller charges. That indicates on the one hand that this longer bunch suffers less from CSR and on the other hand it shows that the adaption of the compression scheme in the linac was successful for this particle distribution.

The normalized transverse slice emittances as presented in plot e) and f) are barely changing during the passage of the extraction arc. The same applies for the transverse projected emittances (cf. figure B.5 and B.6), whereof the vertical is stable at approximately 1.34 μm rad and the horizontal grows by approximately 17 % starting at 1.27 μm rad. These small emittance growth values confirm the successful optimization of the FLASH2 extraction arc as discussed in chapter 6 (cf. figure 6.10).

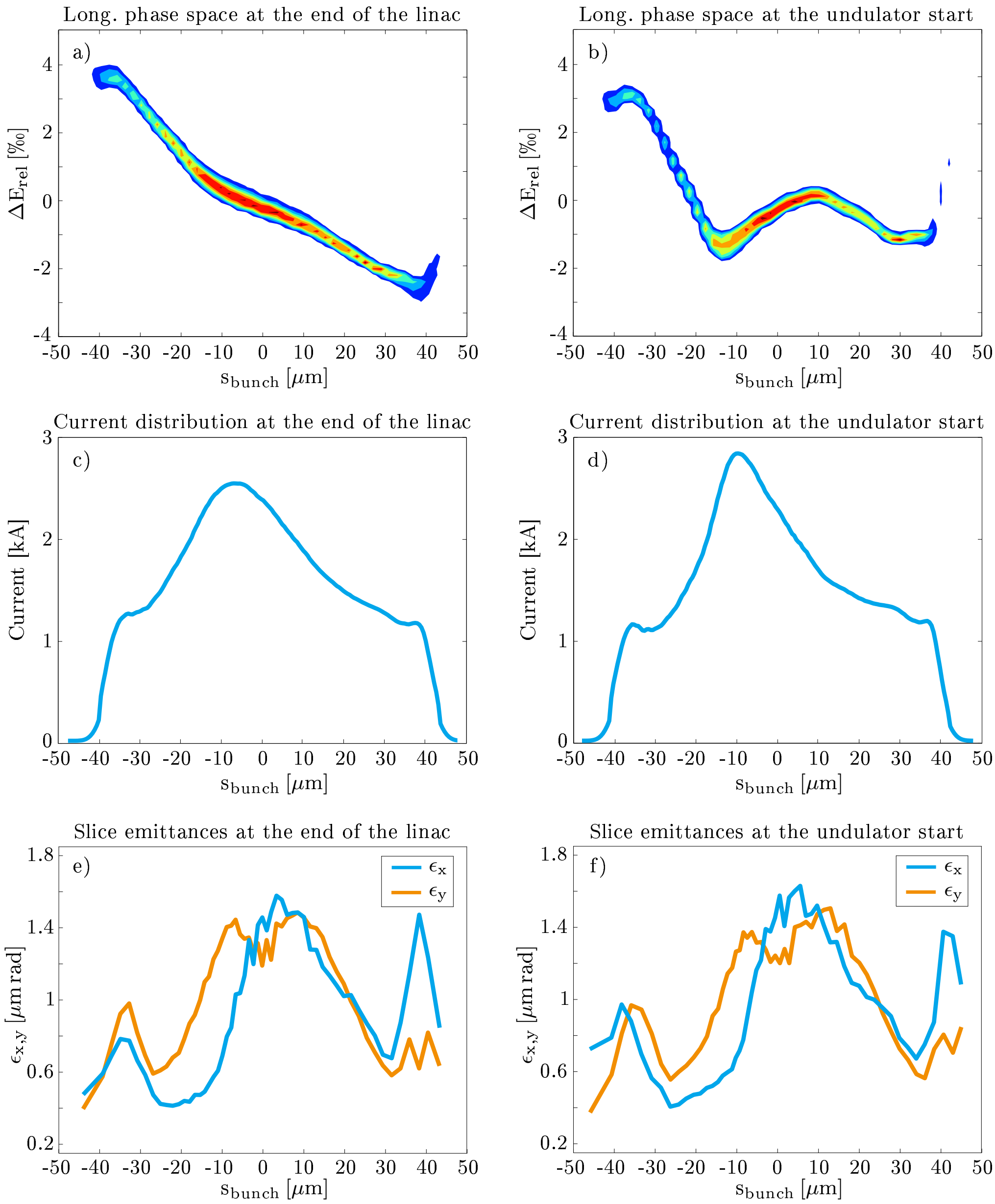

Figure 7.6.: These plots show the longitudinal phase space of the 500 pC bunch in plot a) and plot b), the current distribution of this bunch in plot c) and plot d) as well as the normalized transverse slice emittances in plot e) and f). All plots on the left hand side present the particle distribution at the end of the FLASH linac and the plots on the right hand side show the same particle distribution after the passage of the extraction arc for FLASH2.

7.4.2. FEL Simulations

The plots in figure 7.7 show the FEL simulation results for the 500 pC bunch and the longitudinal phase space of the related particle distribution in plot a). The evolution of the radiation power, as presented in plot b), reaches saturation at about 20 m in the undulator section and the radiation power at the end of the last undulator is approximately 30 GW. It can be observed that the total power spread in the first undulators, where saturation is not yet reached, is smaller in comparison with the bunches discussed so far. The peak of the radiation power distribution in plot c) is, after 20.1 m in the undulator section, approximately at $-8\,\mu$m which correspond roughly with the peak of the current distribution if the slippage of $8.8\,\mu$m is taken into account.

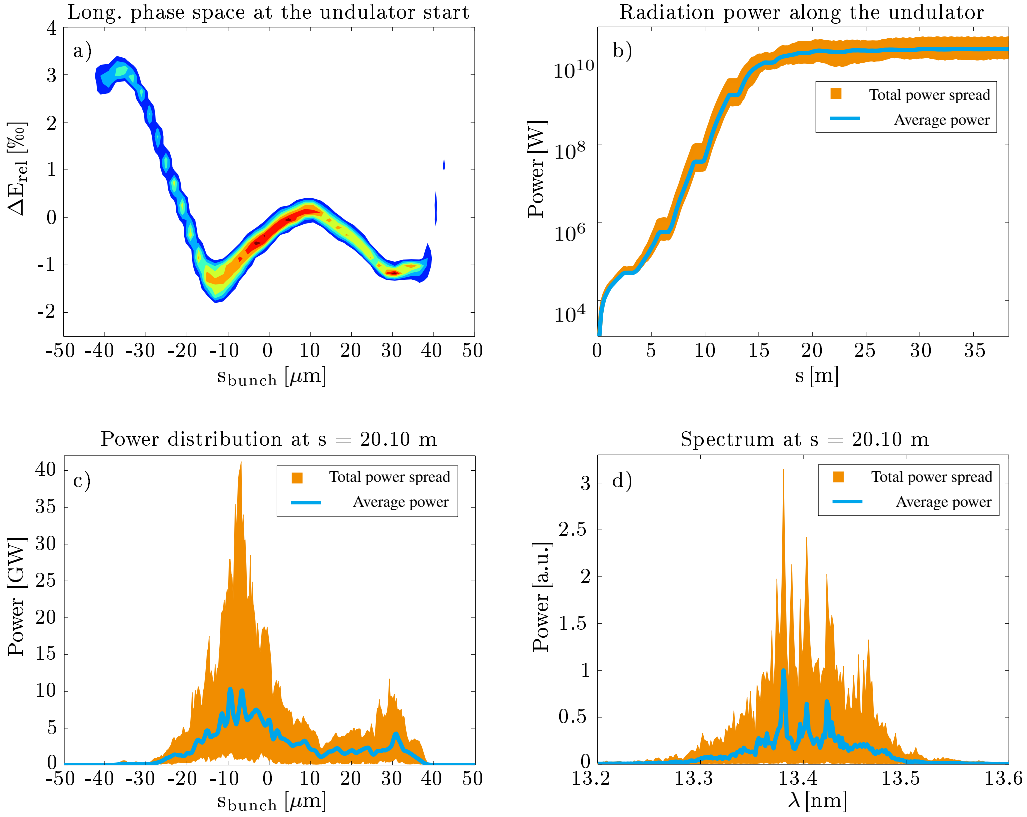

Figure 7.7.: Plot a) shows the longitudinal phase space of the 500 pC particle distribution at the undulator entrance. Plot b) and c) show the radiation power, the first one the evolution along the undulator section and the second the distribution over the bunch. Plot d) presents the spectrum of the emitted radiation.

The power distribution plot shows that some particles in the bunch head are also radiating. The FWHM of the blue curve, representing the average of the 150 seeds, is 13.8 μm. The spectrum, shown in plot d), shows a peak around 13.4 nm and a FWHM of 0.05 nm, thus the relative spectral width is about 0.37 %.

The summery of this simulation is that one can still see a minor impact from CSR in the plots of the longitudinal phase space and of the current distribution, however, the results from SASE simulations are promising. The small additional peak in the power distribution along the bunch due to radiating particles in the bunch's head can be eventually suppressed with a further optimization of the bunch compression in the linac. This simulation showed also that the bunches with higher charges are relatively unproblematic in the FLASH2 beam line.

7.5. Start-to-End Simulations Using a 1 nC Bunch

7.5.1. Particle Tracking Through the Extraction Arc

The 1 nC bunch is the largest bunch used in FLASH and its simulation results are presented in figure 7.8. Plot a) shows the longitudinal phase space at the end of the linac and one can see that the bunch shape is almost perfect. Due to the bunch's length, the CSR effects are very small and there is almost no impact on the 1 nC bunch during the passage through the extraction arc as one can observe in plot b). The current distribution at the end of the linac (plot c) and at the end of the extraction arc (plot d) can hardly be distinguished. The same applies also for the normalized transverse slice emittances as presented in plot e) and f). The projected vertical emittance is approximately 1.77 μm rad at the end of the linac and it increases slightly to 1.82 μm rad at the end of the extraction arc. The projected horizontal emittance grows in the arc by approximately 12 % starting at 2.09 μm rad (cf. figure B.7 and B.8).

It is expected that this bunch shows no problems in the FEL simulation because its hardly modified by the extraction arc for FLASH2 and it reaches the undulators in an optimum condition.

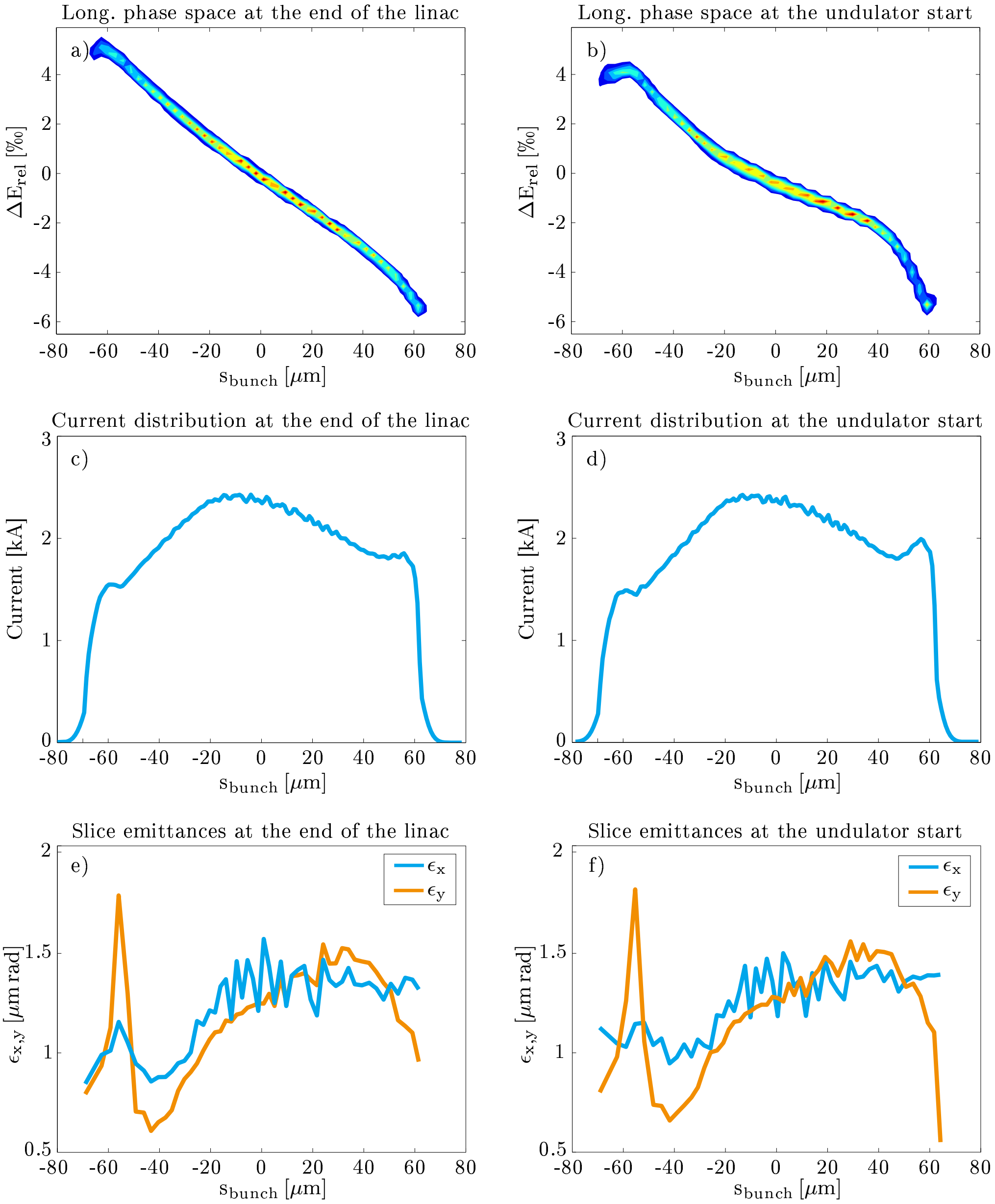

Figure 7.8.: One can find in this figure the longitudinal phase space of the 1 nC bunch at the end of the linac (plot a) and at the end of the extraction arc (plot b). The plots c) and d) represent the current distribution of the same bunch at the same positions as the plots above. Plot e) shows the normalized transverse slice emittances at the end of the linac and plot f) shows also the emittances but at the end of the extraction arc for FLASH2.

7.5.2. FEL Simulations

The FEL simulations using the almost unperturbed 1 nC bunch as shown above, will be presented in the following. The results of the simulation are presented in figure 7.9. Plot a) shows again the longitudinal phase space of the applied particle distribution where almost no impact from CSR or from other effects are visible. The development of the radiation power along the undulator of FLASH2 is presented in plot b) and its maximum at the end of the undulator section is approximately 20 GW. Saturation is reached after the first half of the undulator section's length and this is also the position where the data for the following plots were taken. The exact position used for these evaluations is 20.1 nm as it was for the 500 pC simulation as well as for the simulation using the 250 pC bunch at a wavelength of 13.5 nm. The radiation power distribution is presented in plot c) and one can see that almost all slices of the bunch emit radiation. This is comprehensible

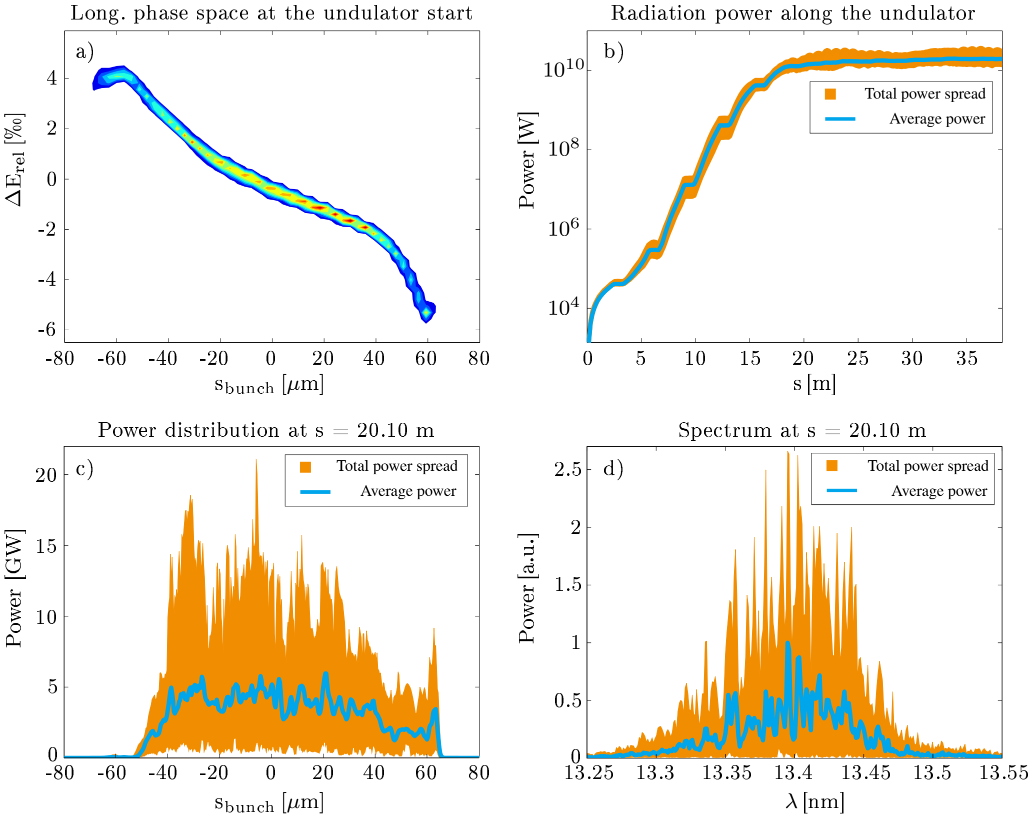

Figure 7.9.: The longitudinal phase space of the 1 nC bunch, which was applied for this FEL simulation is presented in plot a). The evolution of the radiation power along the undulator section is shown in plot b) and the distribution of the radiation power along the bunch can be observed in plot c). Plot d) shows the spectrum obtained with simulations using the 1 nC bunch.

because the current distribution of this bunch (cf. figure 7.8, plot d) is over a wide range above 2 kA. However, the radiating particles at the end and at the head of the bunch have different energies due to the bunch's energy chirp, thus, a broader spectrum was expected as presented in plot d). The peak of the spectrum is around 13.4 nm and the FWHM is approximately 0.1 nm. This leads to a relative spread of 0.74 % which is twice the size observed for the 500 pC bunch.

We can conclude that the CSR impact on the 1 nC bunch is very small and almost no impact can be observed. The required undulator length for saturation and the maximum saturation power are within the bounds of the expected range. The fact that all particles of the bunch radiate, independently of their position in the bunch, in combination with the energy chirp leads to an increased wavelength range. But on the other hand, the integrated radiation power increases if all slice of the bunch radiate.

7.6. Conclusions of the Start-to-End Simulations

The results presented in this chapter showed that the design of the extraction arc of FLASH2 is sufficient for FEL operation and that the applied method for CSR effects mitigation in the bending magnets of the arc was successful.

The small bunches with 100 pC and 250 pC are modified by CSR in the extraction arc but the particle distributions which arrive at the undulator section are still good enough for SASE operation. Eventually, another compression scheme in the FLASH linac can be found in order to achieve particle distributions with only one current peak. However, this seems to be constrained by technical restrictions of the third harmonic accelerating module as it was mentioned before.

The two particle distributions with larger charges showed less impact from CSR and the 1 nC bunch was almost unimpressed by the bending magnets in the extraction arc respectively by the CSR effects. However, this is also a result of the optimized extraction arc and can not be achieved with an arbitrary beam line layout.

8. Summary and Conclusions

The demands on more experimental stations in the VUV-range for FEL synchrotron light users led to the decision to build a second undulator beam line for the existing FEL FLASH, called FLASH2, using the same linear accelerator. The FLASH2 undulators will be equipped with variable gaps, thus, the photon wavelength in FLASH2 will be, within limits, independent of the used wavelength in FLASH1. Both beam lines will cover the same total wavelength range in SASE operation and FLASH2 will provide in addition the possibility to be operated as a seeded FEL.

The building environment and the beam line design of FLASH necessitated a very short extraction arc to the second beam line in order maintain the required space for the undulator section. Due to the fact that the electron bunches are fully compressed at the end of the linac and due to the strong bending magnets required to build the extraction arc on the available space, the modifications of the particle distributions caused by coherent synchrotron radiation effects had to be taken into account during the designing process of the arc.

The optimizations were carried out applying the particle tracking and optimization program `Elegant` using the implemented downhill simplex algorithm. Due to the large number of optimization variables and constraints, the optimization process had to be carried out step by step and under the consideration of beam optics knowledge.

As described in this thesis, the development of the extraction arc for the 2$^{\mathrm{nd}}$ beam line of FLASH considering all given demands was successfully accomplished. The final length of the arc is about 20 m which leaves enough space for the implementation of the planned seeding laser, the undulators and the required vacuum technique as well as for diagnostic elements. The usability of the FLASH2 extraction was shown in start-to-end simulations for different bunches covering the range of the typical particle distributions used at FLASH.

At the time of writing, the construction work on the new tunnel is almost completed, however, the new experimental hall is still under construction. The modifications of the existing beam line around the extraction position is finished and the most of the beam line elements of FLASH2 in the extraction arc are installed. The undulator beam line of FLASH2, which is housed in the new tunnel, is still under construction. The commissioning of FLASH1 will start in October 2013 and the first beam in FLASH2 is expected to be realized in 2014.

A. Calculations of FEL Quantities and CSR Parameters

A.1. FEL Quantities

In this chapter, the parameters presented in chapter 2 will be calculated for the new beam line of FLASH. All calculations will be carried out for an example case with an electron energy of $E = 1\,\mathrm{GeV}$ ($\gamma_{1\mathrm{GeV}} = 1957$), an energy spread of $\Delta_E = 0.5\,\mathrm{MeV}$, an undulator parameter $K = 1$ and an average beta function in the undulator of $\beta_{\mathrm{av}} = 6\,\mathrm{m}$. The period of the FLASH2 undulators is $\lambda_u = 31.4\,\mathrm{mm}$. Furthermore, the normalized transverse emittances are $\epsilon_x = \epsilon_y = 1\,\mu\mathrm{m\,rad}$ which leads to physical emittances of approximately $\epsilon_{px} = \epsilon_{py} \approx 0.5\ \mathrm{nm\,rad}$.

The wave length of the spontaneous undulator radiation as described in equation 2.3 is, assuming $\Theta = 0$,

$$\begin{aligned}\lambda_l &= \frac{\lambda_u}{2\,\gamma_r^2}\left(1 + \frac{K^2}{2} + \gamma_r^2\Theta^2\right) = \frac{0.0314\,\mathrm{m}}{2 * 1957^2}\left(1 + \frac{1}{2}\right)\\ &\approx 6.15\,\mathrm{nm}.\end{aligned}$$

For the calculation of the gain parameter Γ, we need the modified undulator parameter as presented in equation 2.9:

$$\begin{aligned}\hat{K} &= K\left[J_0\left(\frac{K^2}{4 + 2K^2}\right) - J_1\left(\frac{K^2}{4 + 2K^2}\right)\right] = 1\left[J_0\left(\frac{1}{6}\right) - J_1\left(\frac{1}{6}\right)\right]\\ &\approx 0.91.\end{aligned}$$

The electron density, which is also necessary for the calculation of Γ, can be calculated on the basis of a round beam approximation with an average beam size of

$$\sigma_{\mathrm{av}} = \sqrt{\epsilon_p\ \beta_{\mathrm{av}}} \approx \sqrt{3.1\,\mathrm{nm}} \approx 55\,\mu\mathrm{m}$$

and with a peak current $I_p = 2.5\,\mathrm{kA}$ as usual for particle distributions in FLASH. The electron density can be approximated as follows:

$$n_e \approx \frac{I_p}{e\,c\,\pi\,\sigma_{\mathrm{av}}^2} \approx 5.4 \cdot 10^{21}\ \mathrm{m}^{-3}.$$

Following the description in equation 2.11, the gain parameter is

$$\begin{aligned}\Gamma = \left[\frac{\mu_0 \hat{K}^2 e^2 k_u n_e}{4\gamma_r^3 m_e}\right]^{1/3} &\approx \left[\frac{2\,\pi\,1.26\cdot 10^{-6}\frac{\mathrm{N}}{\mathrm{A}^2}\ 0.91^2\ (1.602\cdot 10^{-19}\mathrm{C})^2\ 5.4\cdot 10^{21}\frac{1}{\mathrm{m}^3}}{4\ 1957^3\ 9.11\cdot 10^{-31}\mathrm{kg}\cdot 31,4\mathrm{mm}}\right]^{1/3}\\ &\approx 1.019\ \mathrm{m}^{-1}.\end{aligned}$$

Now we can calculate the FEL parameter and the idealized gain length as shown in the equations 2.14 respectively 2.16:

$$\rho_{\mathrm{FEL}} = \frac{\Gamma}{2k_u} \approx \frac{1.019\ \mathrm{m}^{-1}}{2\cdot 0.0314\ \mathrm{m}} \approx 2.55\cdot 10^{-3} \qquad \text{and}$$

$$L_{\mathrm{g0}} = 1/(\sqrt{3}\Gamma) \approx 1/(\sqrt{3}\ 1.019\ \mathrm{m}^{-1}) \approx 0.57\ \mathrm{m}.$$

The relative energy spread can be written in untis of the FEL parameter:

$$\sigma_\eta = \frac{0.5\,\mathrm{MeV}}{1\,\mathrm{GeV}} \approx 0.20\,\rho_{\mathrm{FEL}}.$$

The plasma frequence for FLASH2 is:

$$\begin{aligned}\omega_p^* = \sqrt{\frac{\eta_e\, e^2}{\gamma_r\,\epsilon_0\, m_e}} &\approx \sqrt{\frac{5.4\cdot 10^{-21}\frac{1}{\mathrm{m}^3}\cdot(1.602\cdot 10^{-19}\,\mathrm{C})^2}{1957\ 8.85\cdot 10^{-12}\frac{\mathrm{As}}{\mathrm{Vm}}\ 9.11\cdot 10^{-31}\,\mathrm{kg}}}\\ &\approx 9,36\cdot 10^{10}\ \frac{1}{\mathrm{s}}\end{aligned}$$

and the space charge parameter can be calculated as follows:

$$\begin{aligned}k_p = \sqrt{\frac{2\,\lambda_l}{\lambda_u}}\,\frac{\omega_p^*}{c} &\approx \sqrt{\frac{2\cdot 6.15\cdot 10^{-9}\,\mathrm{m}}{31.4\cdot 10^{-3}\,\mathrm{m}}}\ \frac{9.36\cdot 10^{-11}\,\frac{1}{\mathrm{s}}}{3\cdot 10^{8}\,\frac{\mathrm{m}}{\mathrm{s}}}\\ &\approx 0.195\\ &\approx 0.19\ \Gamma.\end{aligned}$$

According to equation 2.18, the saturation power of the example case calculated with the one-dimensional theory is:

$$\begin{aligned}P_{\mathrm{sat}} \approx \rho_{\mathrm{FEL}}\ \frac{\gamma_r m_e c^2 I_0}{e} &\approx 2.55\cdot 10^{-3}\frac{1957\ 9.11\cdot 10^{-31}\,\mathrm{kg}\ (3.0\cdot 10^{8}\,\frac{\mathrm{m}}{\mathrm{s}})^2\ 2.5\mathrm{kA}}{1.602\cdot 10^{-19}\mathrm{C}}\\ &\approx 6.36\,\mathrm{GW}\end{aligned}$$

The next step will be to calculate the parameter Λ as introduced by M. Xie in order to be able to get a more precise approximation of the gain length and the saturation power. More information about the calculation of Λ can be found in [14, 19].

$$\begin{aligned}\Lambda =& a_1\,\chi_d^{a_2} + a_3\,\chi_\epsilon^{a_4} + a_5\,\chi_\gamma^{a_6} + a_7\,\chi_\epsilon^{a_8}\,\chi_\gamma^{a_9} + a_{10}\,\chi_d^{a_{11}}\,\chi_\gamma^{a_{12}}\\ &+ a_{13}\,\chi_d^{a_{14}}\,\chi_\epsilon^{a_{15}} + a_{16}\,\chi_d^{a_{17}}\,\chi_\epsilon^{a_{18}}\,\chi_\gamma^{a_{19}}\end{aligned}$$

with the energy spread parameter χ_γ, the diffraction parameter χ_d and the angular spread parameter χ_ϵ [14, 19]:

$$\begin{aligned}
\chi_\gamma &= \tfrac{L_{\mathrm{g0}} 4\pi\sigma_E}{\lambda_u} &&\approx \frac{0.57\,\mathrm{m}\ 4\ \pi\ 5\cdot 10^{-4}}{0.0314\,\mathrm{m}} \approx 0.1134\\
\chi_d &= \tfrac{L_{\mathrm{g0}}\lambda_l}{4\pi\sigma_r^2} &&\approx \frac{0.57\,\mathrm{m}\ 6.15\,\mathrm{nm}}{4\ \pi\ 0.511\,\mathrm{nm\,rad}} \approx 0.0904\\
\chi_\epsilon &= \tfrac{L_{\mathrm{g0}} 4\pi\epsilon}{\beta_{\mathrm{av}}\lambda_l} &&\approx \frac{0.57\,\mathrm{m}\ 4\ \pi\ 0.511\,\mathrm{nm\,rad}}{6\,\mathrm{m}\ 6.15\,\mathrm{nm}} \approx 0.0986,
\end{aligned}$$

and with the fitted coefficients [14, 19]:

$$\begin{aligned}
&a_1 = 0.45,\ a_2 = 0.57,\ a_3 = 0.55,\ a_4 = 1.6,\ a_5 = 3.0,\\
&a_6 = 2.0,\ a_7 = 0.35,\ a_8 = 2.9,\ a_9 = 2.4,\ a_{10} = 51,\\
&a_{11} = 0.95,\ a_{12} = 3.0,\ a_{13} = 5.4,\ a_{14} = 0.7,\ a_{15} = 1.9,\\
&a_{16} = 1140,\ a_{17} = 2.2,\ a_{18} = 2.9,\ a_{19} = 3.2.
\end{aligned}$$

This parameters and coefficients lead to $\Lambda \approx 0.165$ as used in chapter 2. Now we are also able to calculate

$$L_{\mathrm{g,xie}} = L_{\mathrm{g0}}\ (1+\Lambda) \approx 0.57\ \mathrm{m}(1+0.165) \approx 0.664\,\mathrm{m}.$$

The more accurate calculation of the saturation power is (cf. equation 2.22):

$$\begin{aligned}
P_{\text{sat, xie}} &\approx 1.6\ \rho_{\mathrm{FEL}}\ P_{\mathrm{Beam}} \left(\frac{L_{\mathrm{g0}}}{L_{\mathrm{g,xie}}}\right)^2\\
&\approx 1.6\cdot 2.55\cdot 10^{-3}\ \frac{1957\cdot 9.11\cdot 10^{-31}\,\mathrm{kg}\ (3.0\cdot 10^8\ \frac{\mathrm{m}}{\mathrm{s}})^2\ 2.5\mathrm{kA}}{1.602\cdot 10^{-19}\mathrm{C}} \left(\frac{0.57\,\mathrm{m}}{0.664\,\mathrm{m}}\right)^2\\
&\approx 4.69\,GW.
\end{aligned}$$

Finally, the restrictions on the physical emittances will be calculated for the example case. The restriction as presented in inequation 2.19 is

$$\epsilon_x < \frac{\beta_{\mathrm{av}}}{2\sqrt{2}\gamma_r^2}\,\rho_{\mathrm{FEL}} \approx \frac{6\,\mathrm{m}}{2\sqrt{2}\ 1957^2}\,2.55\cdot 10^{-3} \approx 1.41\,\mathrm{nm\,rad}.$$

The restriction as presented in inequation 2.20 is

$$\epsilon_x \le \frac{\lambda_l}{4\pi} \approx \frac{6.15\,\mathrm{nm}}{4\pi} \approx 0.49\,\mathrm{nm\,rad}.$$

A summary of all parameters calculated above is given in table A.1.

Table A.1.: Summary of all parameters introduced in chapter 2 for the example case as described above.

$\lambda_u \approx 31.4\,\mathrm{mm}$	$\beta_{\mathrm{av}} = 6\,\mathrm{m}$	$K = 1$	$\hat{K} \approx 0.91$
$E = 1\,\mathrm{GeV}$	$\sigma_E = 5 \cdot 10^{-4}$	$n_e \approx 5.4 \cdot 10^{21}\ \mathrm{m}^{-3}$	$\sigma_{av} \approx 3.1\mathrm{nm}$
$\epsilon_n = 1\,\mu\mathrm{m\,rad}$	$\epsilon_p \approx 0.51\,\mathrm{nm\,rad}$	$\epsilon_{m1} \approx 1.41\,\mathrm{nm\,rad}$	$\epsilon_{m2} \approx 0.49\,\mathrm{nm\,rad}$
$\lambda_l \approx 6.15\,\mathrm{nm}$	$\Gamma \approx 1.019\ \mathrm{m}^{-1}$	$\rho_{\mathrm{FEL}} \approx 2.55 \cdot 10^{-3}$	$L_{\mathrm{g0}} \approx 0.57\ \mathrm{m}$
$\chi_\gamma \approx 0.1134$	$\chi_d \approx 0.0904$	$\chi_\epsilon \approx 0.0986$	$\Lambda \approx 0.165$
$P_{\mathrm{sat}} \approx 6.36\,\mathrm{GW}$	$L_{\mathrm{g,xie}} \approx 0.664\,\mathrm{m}$	$P_{\mathrm{sat,\ xie}} \approx 4.69\,GW$	$\omega_p^* \approx 9.36 \cdot 10^{10}\mathrm{s}^{-1}$

A.2. CSR Parameters

In this section, the CSR parameters as described in chapter 3 will be calculated for a Gaussian distributed bunch with a charge of 100 pC, a one-sigma length of $\sigma_z = 5\,\mu\mathrm{m}$ and a particle energy of 1 GeV. The length of the used bending magnet is 1 m and the bending radius is $\rho = 8.8\,\mathrm{m}$. That corresponds to the parameters of the septum as used in the FLASH2 extraction arc. The overtaking length as described in equation 3.1 is:

$$L_0 = \sqrt[3]{24\,\rho^2\sigma_z} \approx \sqrt[3]{24\ 8.8^2\ 5 \cdot 10^{-6}\,\mathrm{m}} \approx 0.21\,\mathrm{m}.$$

The distance between the electron and photon trajectory is:

$$w_0 = \sqrt[3]{\rho\ \sigma_z^2} \approx \sqrt[3]{8.8\ (5 \cdot 10^{-6})^2} \approx 6.04 \cdot 10^{-4}\,\mathrm{m}.$$

The approximated steady state field in the bending magnet, calculated with the values of the above mentioned example is:

$$E_c \approx \frac{1}{\pi}\frac{Z_0\,I_0}{L_0} \approx \frac{1}{\pi}\frac{376.73\,\Omega\ 2.5\,\mathrm{kA}}{0.21\,\mathrm{m}} \approx 1.43\,\mathrm{MV/m} \tag{A.1}$$

and the decay of the CSR wake field behind the bending magnet is

$$E_{\mathrm{dec}}(d) \approx -\frac{1}{2\pi}\frac{Z_0\,I_0}{0.5\,L_0 + d} \approx -\frac{1}{2\pi}\frac{376.73\,\Omega\ 2.5\,\mathrm{kA}}{0.5\ 0.21\,\mathrm{m} + d} \approx -\frac{149900\,\mathrm{V}}{0.105\,\mathrm{m} + d}\ , \tag{A.2}$$

with d indicating the wake's position in reference to the end of the bending magnet.

B. Particle Distributions

B.1. Start-to-End Simulations

In this section, five different particle distributions applied in the start-to-end simulations using the FLASH2 beam line are presented. The distributions cover the typical bunch charge range of FLASH between 100 pC and 1 nC. The plots show the course of the current distribution along the bunch, the longitudinal phase space, a top and a side view of the distribution, the slice emittances, the slice energy spread and the beam mismatch along the bunch. Furthermore, some beam parameters are presented as well. All plots show 90 % of the initial distribution. 10 % of the particles were cut off at the head and tail for the calculation of the projected emittances.

The plots are shown on the following pages in the figures B.1 - B.8 sorted by the bunch charge. On the left pages one can find the particle distributions at the end of the FLASH linac and on the right hand side the plots representing the particle distributions at the start of the undulator section. This arrangement allows to compare the two plots and to see the impact of the extraction arc on the bunches.

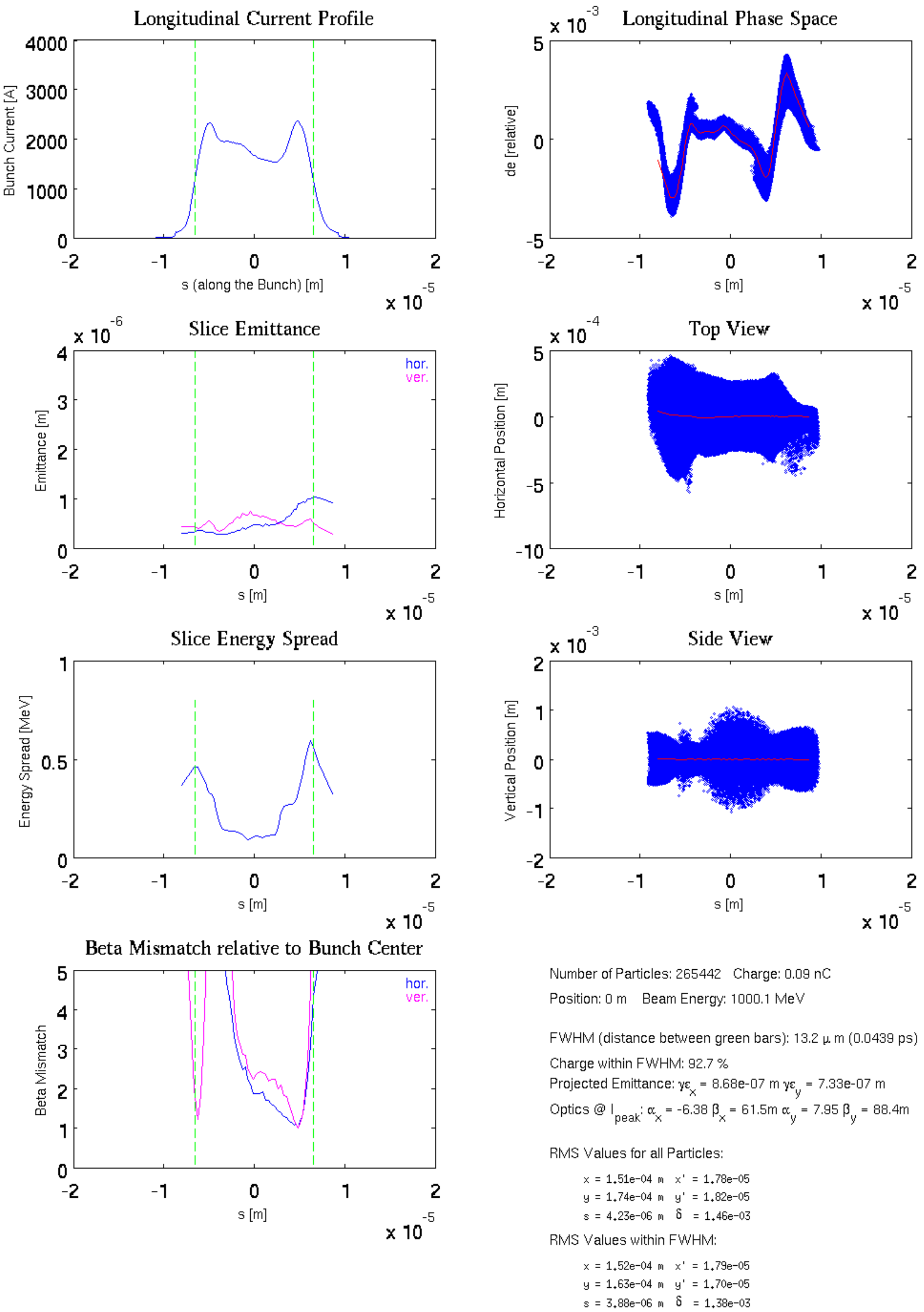

Number of Particles: 265442 Charge: 0.09 nC

Position: 0 m Beam Energy: 1000.1 MeV

FWHM (distance between green bars): 13.2 μ m (0.0439 ps)

Charge within FWHM: 92.7 %

Projected Emittance: $\gamma\epsilon_x$ = 8.68e-07 m $\gamma\epsilon_y$ = 7.33e-07 m

Optics @ I_{peak}: α_x = -6.38 β_x = 61.5m α_y = 7.95 β_y = 88.4m

RMS Values for all Particles:

```
x = 1.51e-04 m  x' = 1.78e-05
y = 1.74e-04 m  y' = 1.82e-05
s = 4.23e-06 m  δ  = 1.46e-03
```

RMS Values within FWHM:

```
x = 1.52e-04 m  x' = 1.79e-05
y = 1.63e-04 m  y' = 1.70e-05
s = 3.88e-06 m  δ  = 1.38e-03
```

Figure B.1.: The 100 pC bunch optimized for the new beam line FLASH2 at the end of the FLASH linac.

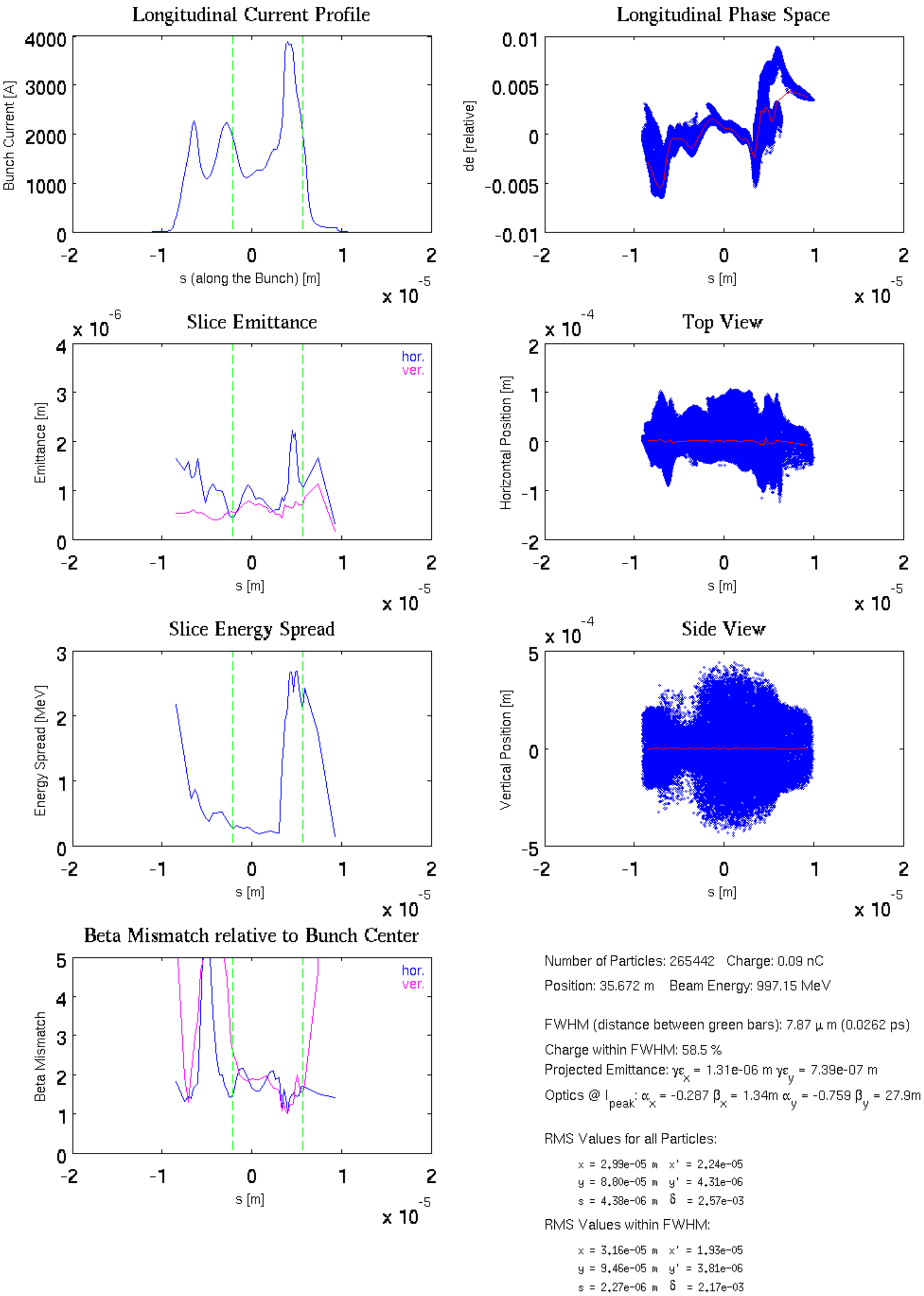

Number of Particles: 265442 Charge: 0.09 nC

Position: 35.672 m Beam Energy: 997.15 MeV

FWHM (distance between green bars): 7.87 µ m (0.0262 ps)

Charge within FWHM: 58.5 %

Projected Emittance: $\gamma\epsilon_x$ = 1.31e-06 m $\gamma\epsilon_y$ = 7.39e-07 m

Optics @ I_{peak}: α_x = -0.287 β_x = 1.34m α_y = -0.759 β_y = 27.9m

RMS Values for all Particles:

```
x = 2.99e-05 m  x' = 2.24e-05
y = 8.80e-05 m  y' = 4.31e-06
s = 4.38e-06 m  δ  = 2.57e-03
```

RMS Values within FWHM:

```
x = 3.16e-05 m  x' = 1.93e-05
y = 9.46e-05 m  y' = 3.81e-06
s = 2.27e-06 m  δ  = 2.17e-03
```

Figure B.2.: The 100 pC bunch at the start of the undulator section in the FLASH2 beam line.

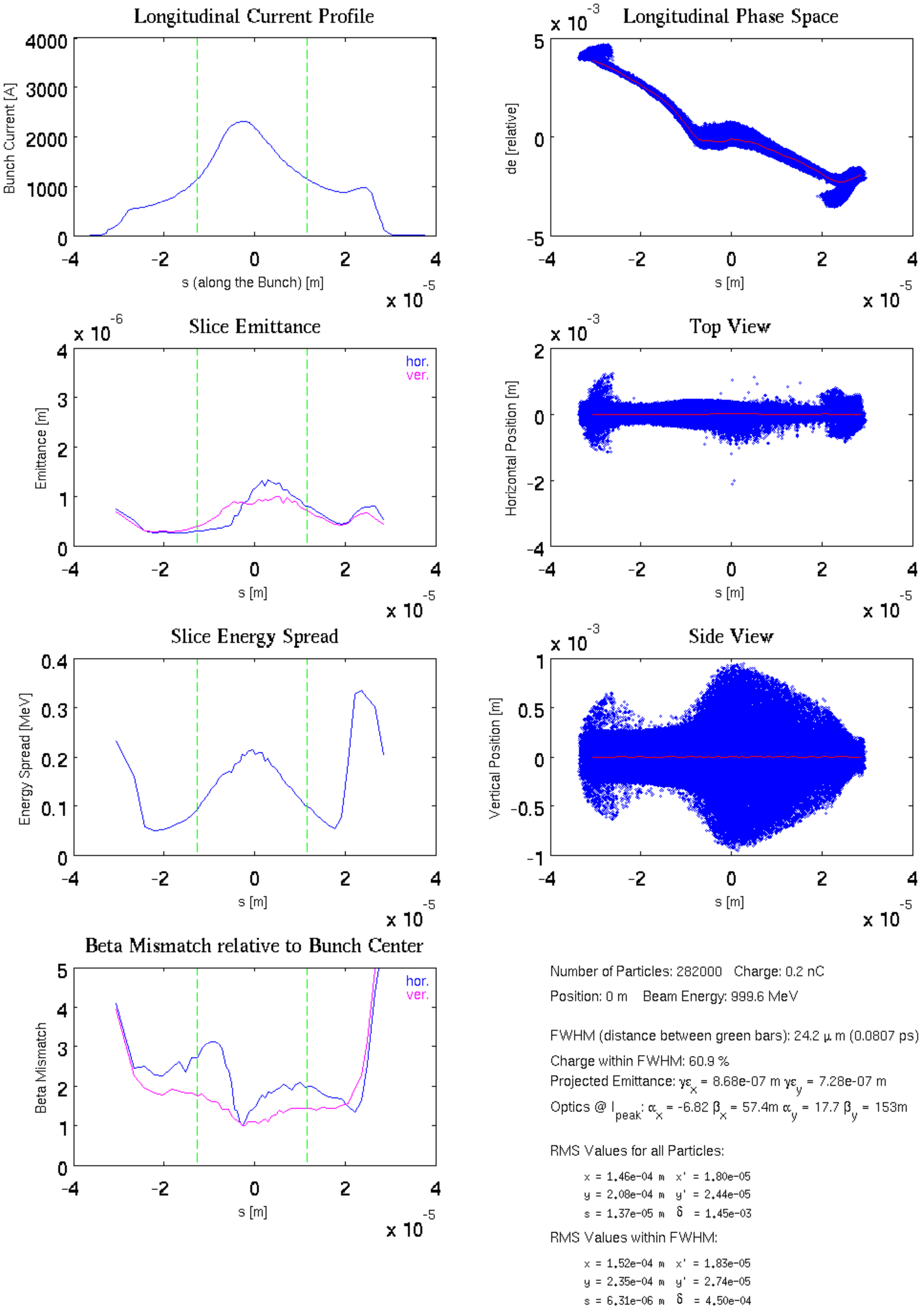

Number of Particles: 282000 Charge: 0.2 nC

Position: 0 m Beam Energy: 999.6 MeV

FWHM (distance between green bars): 24.2 μ m (0.0807 ps)

Charge within FWHM: 60.9 %

Projected Emittance: $\gamma\epsilon_x$ = 8.68e-07 m $\gamma\epsilon_y$ = 7.28e-07 m

Optics @ I_{peak}: α_x = -6.82 β_x = 57.4m α_y = 17.7 β_y = 153m

RMS Values for all Particles:

```
x = 1.46e-04 m  x' = 1.80e-05
y = 2.08e-04 m  y' = 2.44e-05
s = 1.37e-05 m  δ  = 1.45e-03
```

RMS Values within FWHM:

```
x = 1.52e-04 m  x' = 1.83e-05
y = 2.35e-04 m  y' = 2.74e-05
s = 6.31e-06 m  δ  = 4.50e-04
```

Figure B.3.: The 250 pC bunch optimized for the new beam line FLASH2 at the end of the FLASH linac.

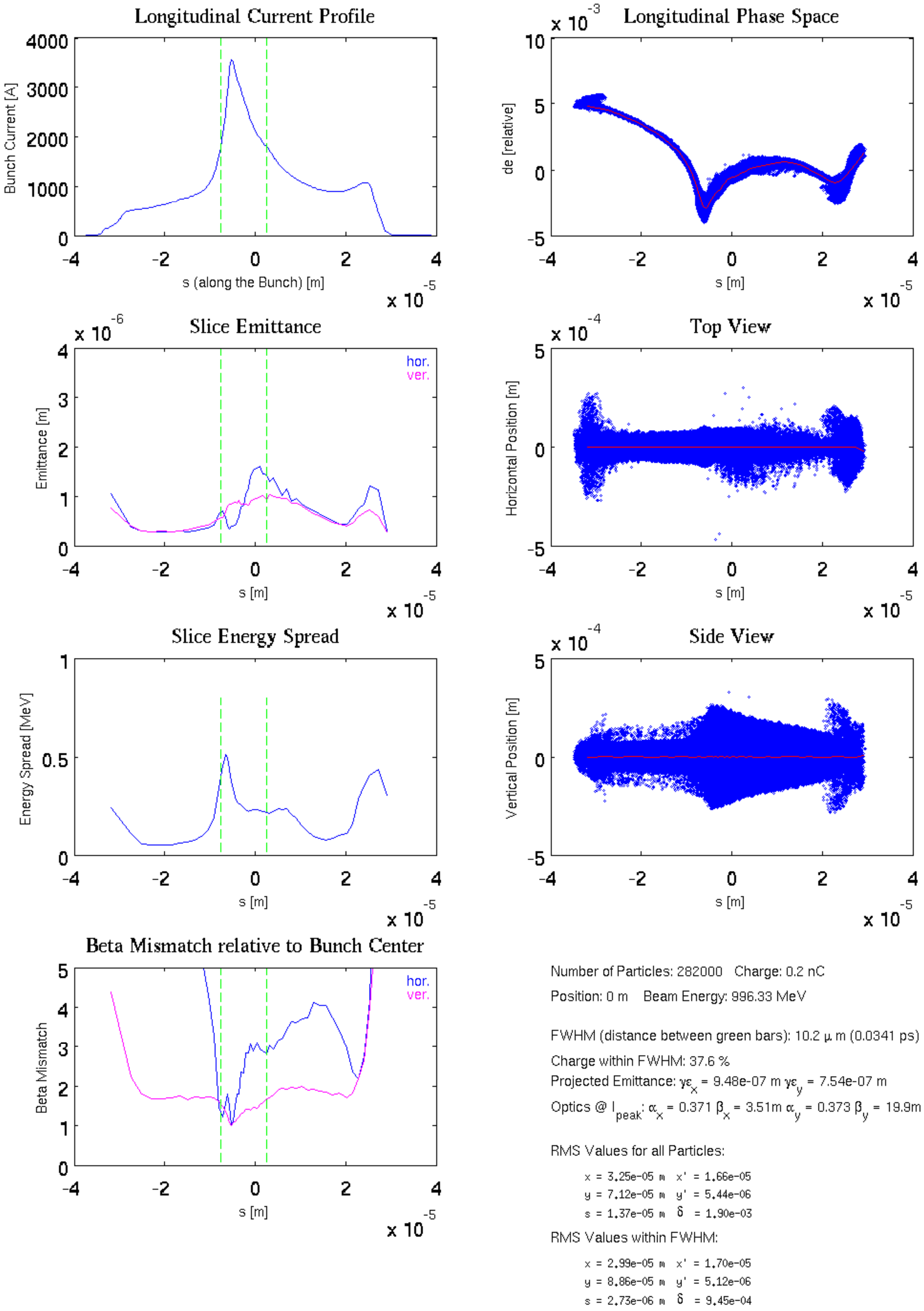

Number of Particles: 282000 Charge: 0.2 nC

Position: 0 m Beam Energy: 996.33 MeV

FWHM (distance between green bars): 10.2 μ m (0.0341 ps)

Charge within FWHM: 37.6 %

Projected Emittance: $\gamma\epsilon_x$ = 9.48e-07 m $\gamma\epsilon_y$ = 7.54e-07 m

Optics @ I_{peak}: α_x = 0.371 β_x = 3.51m α_y = 0.373 β_y = 19.9m

RMS Values for all Particles:

x = 3.25e-05 m x' = 1.66e-05
y = 7.12e-05 m y' = 5.44e-06
s = 1.37e-05 m δ = 1.90e-03

RMS Values within FWHM:

x = 2.99e-05 m x' = 1.70e-05
y = 8.86e-05 m y' = 5.12e-06
s = 2.73e-06 m δ = 9.45e-04

Figure B.4.: The 250 pC bunch at the start of the undulator section in the FLASH2 beam line.

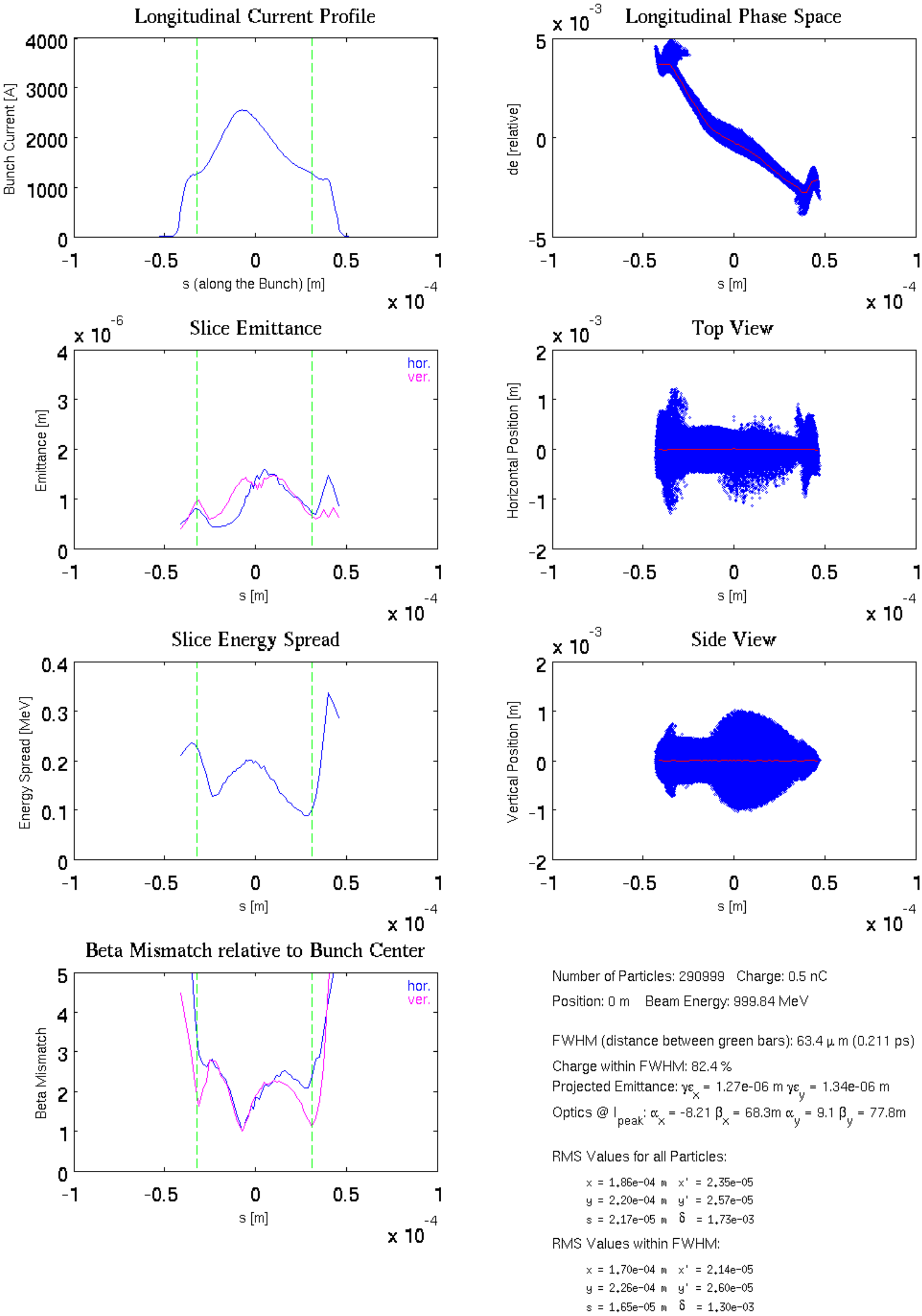

Number of Particles: 290999   Charge: 0.5 nC

Position: 0 m   Beam Energy: 999.84 MeV

FWHM (distance between green bars): 63.4 μ m (0.211 ps)

Charge within FWHM: 82.4 %

Projected Emittance: $\gamma\epsilon_x$ = 1.27e-06 m $\gamma\epsilon_y$ = 1.34e-06 m

Optics @ I_{peak}: α_x = -8.21 β_x = 68.3m α_y = 9.1 β_y = 77.8m

RMS Values for all Particles:

x = 1.86e-04 m   x' = 2.35e-05
y = 2.20e-04 m   y' = 2.57e-05
s = 2.17e-05 m δ = 1.73e-03

RMS Values within FWHM:

x = 1.70e-04 m   x' = 2.14e-05
y = 2.26e-04 m   y' = 2.60e-05
s = 1.65e-05 m δ = 1.30e-03

Figure B.5.: The 500 pC bunch optimized for the new beam line FLASH2 at the end of the FLASH linac.

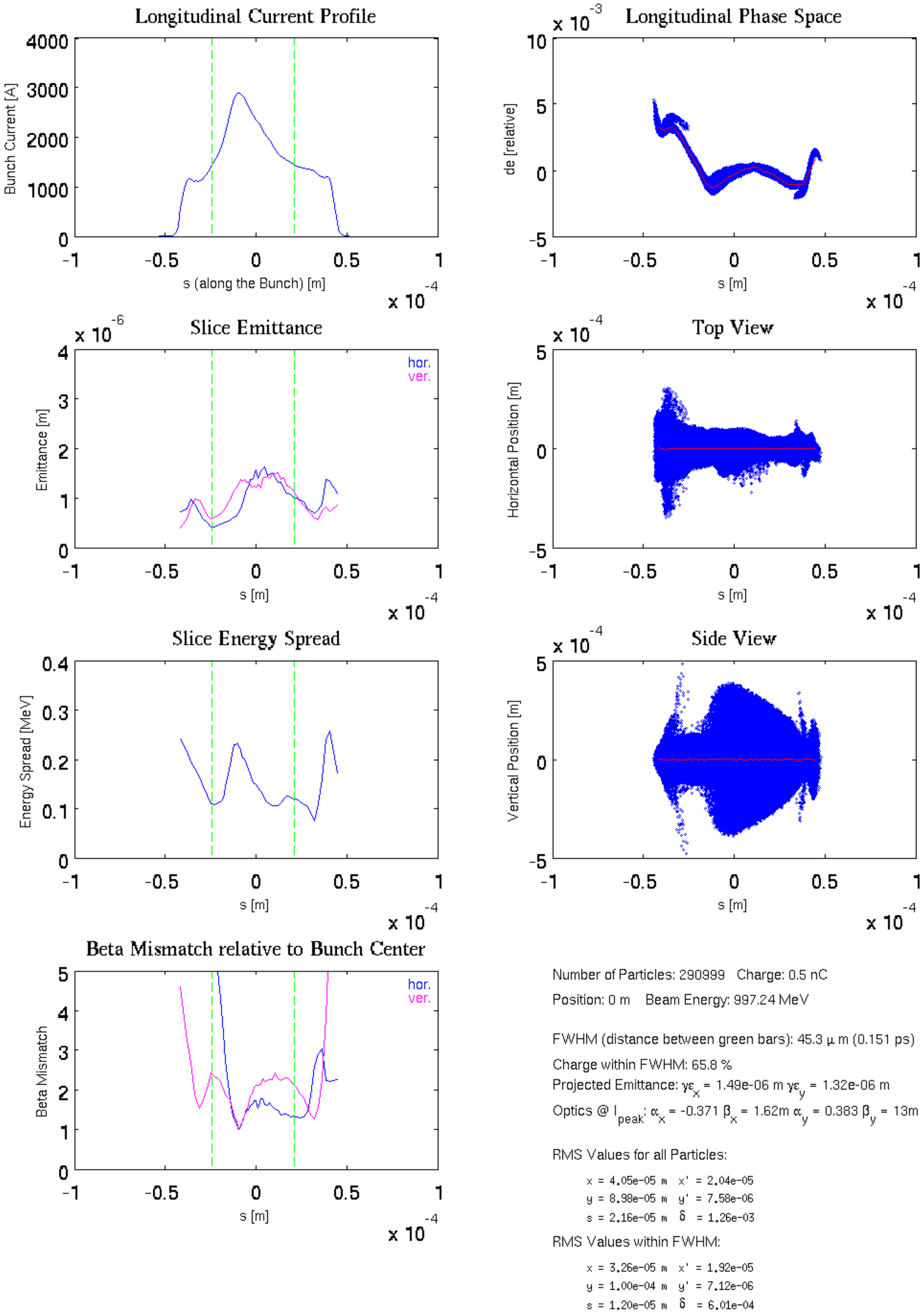

Number of Particles: 290999   Charge: 0.5 nC

Position: 0 m   Beam Energy: 997.24 MeV

FWHM (distance between green bars): 45.3 μ m (0.151 ps)

Charge within FWHM: 65.8 %

Projected Emittance: $\gamma\epsilon_x$ = 1.49e-06 m $\gamma\epsilon_y$ = 1.32e-06 m

Optics @ I_{peak}: α_x = -0.371 β_x = 1.62m α_y = 0.383 β_y = 13m

RMS Values for all Particles:

x = 4.05e-05 m x' = 2.04e-05
y = 8.98e-05 m y' = 7.58e-06
s = 2.16e-05 m δ = 1.26e-03

RMS Values within FWHM:

x = 3.26e-05 m x' = 1.92e-05
y = 1.00e-04 m y' = 7.12e-06
s = 1.20e-05 m δ = 6.01e-04

Figure B.6.: The 500 pC bunch at the start of the undulator section in the FLASH2 beam line.

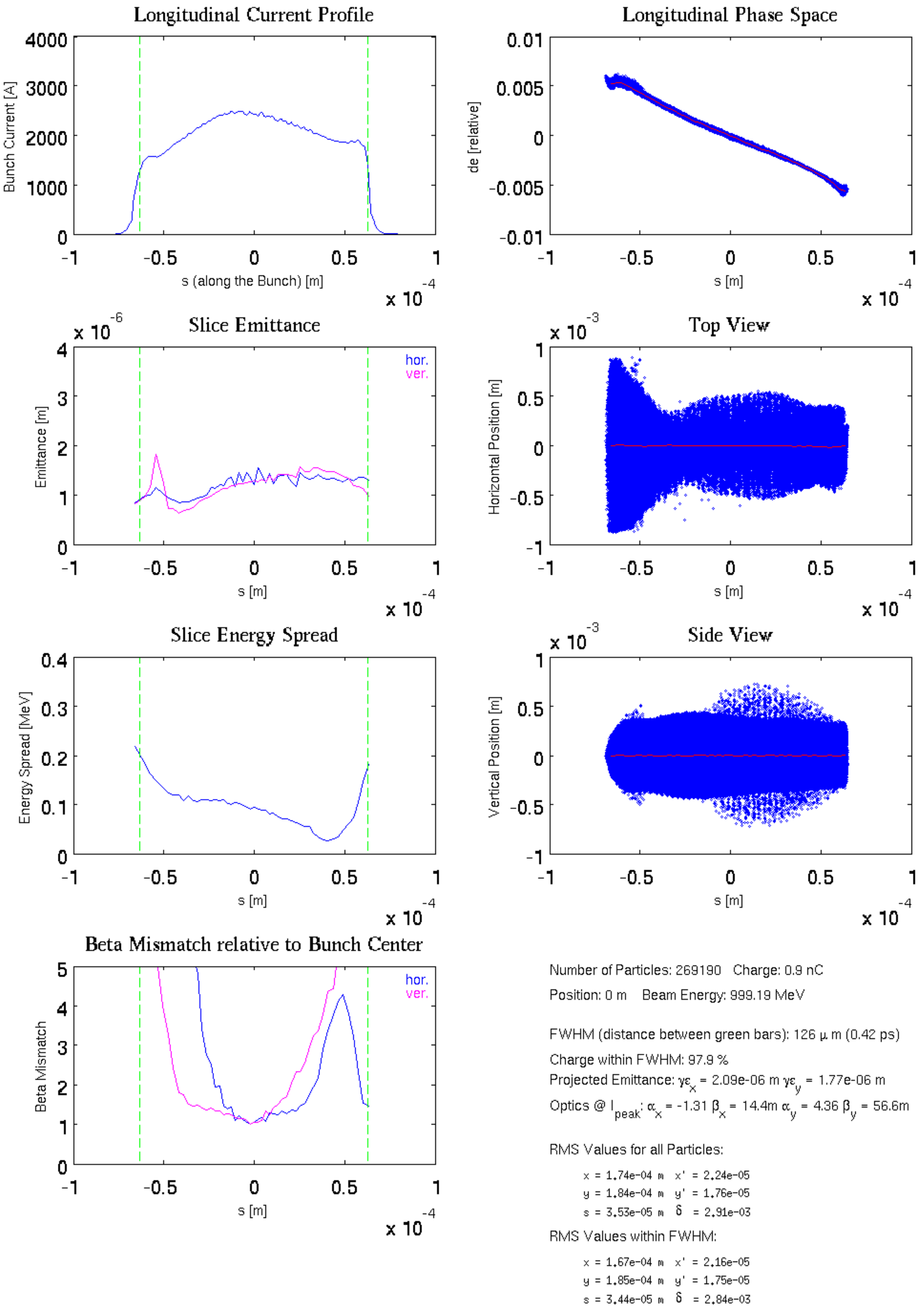

Number of Particles: 269190   Charge: 0.9 nC

Position: 0 m   Beam Energy: 999.19 MeV

FWHM (distance between green bars): 126 μ m (0.42 ps)

Charge within FWHM: 97.9 %

Projected Emittance: $\gamma\varepsilon_x$ = 2.09e-06 m $\gamma\varepsilon_y$ = 1.77e-06 m

Optics @ I_{peak}: α_x = -1.31 β_x = 14.4m α_y = 4.36 β_y = 56.6m

RMS Values for all Particles:

```
x = 1.74e-04 m  x' = 2.24e-05
y = 1.84e-04 m  y' = 1.76e-05
s = 3.53e-05 m  δ  = 2.91e-03
```

RMS Values within FWHM:

```
x = 1.67e-04 m  x' = 2.16e-05
y = 1.85e-04 m  y' = 1.75e-05
s = 3.44e-05 m  δ  = 2.84e-03
```

Figure B.7.: The 1 nC bunch optimized for the new beam line FLASH2 at the end of the FLASH linac.

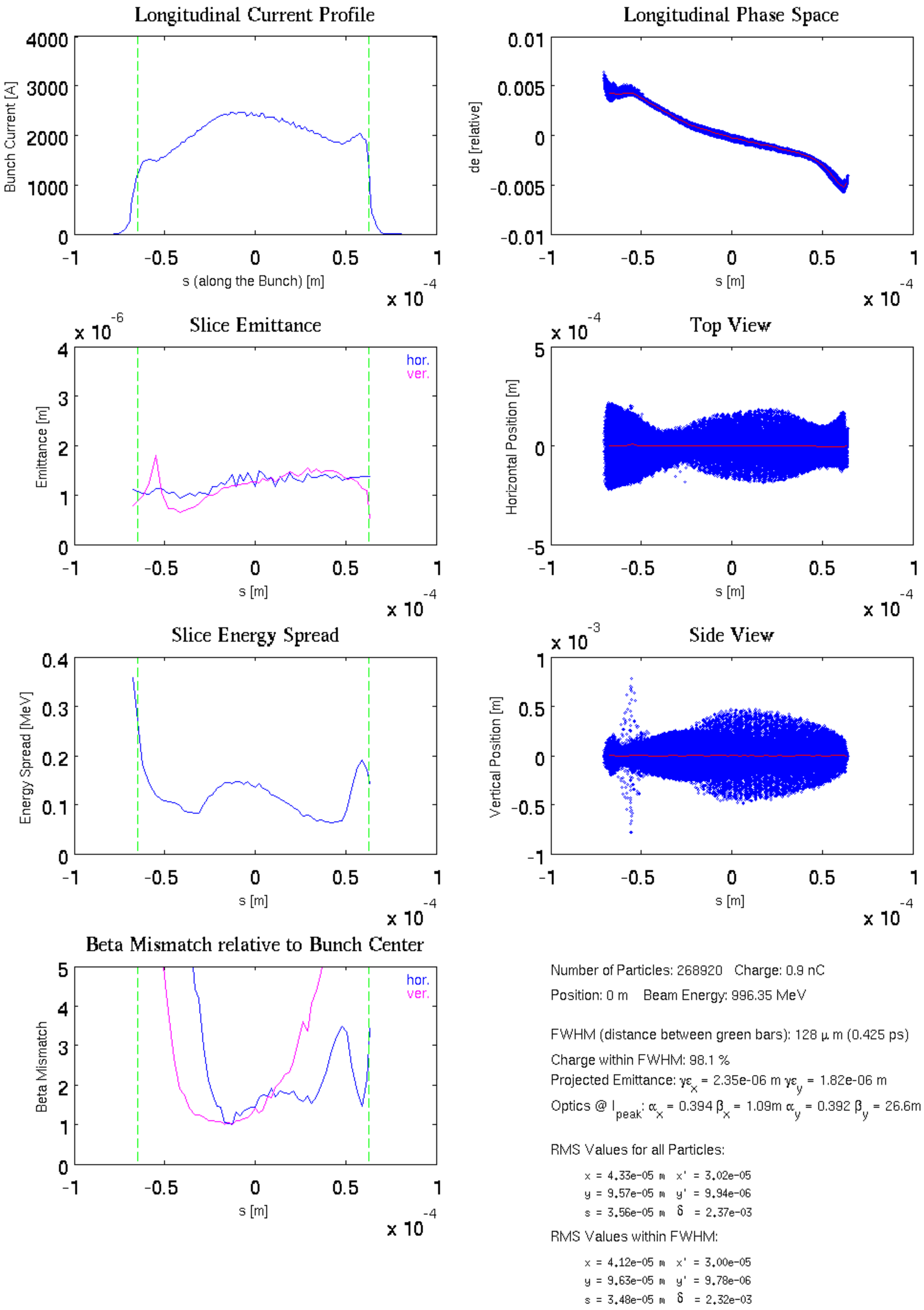

Number of Particles: 268920   Charge: 0.9 nC

Position: 0 m   Beam Energy: 996.35 MeV

FWHM (distance between green bars): 128 µ m (0.425 ps)

Charge within FWHM: 98.1 %

Projected Emittance: $\gamma\epsilon_x$ = 2.35e-06 m $\gamma\epsilon_y$ = 1.82e-06 m

Optics @ I_{peak}: α_x = 0.394 β_x = 1.09m α_y = 0.392 β_y = 26.6m

RMS Values for all Particles:

```
x = 4.33e-05 m  x' = 3.02e-05
y = 9.57e-05 m  y' = 9.94e-06
s = 3.56e-05 m  δ  = 2.37e-03
```

RMS Values within FWHM:

```
x = 4.12e-05 m  x' = 3.00e-05
y = 9.63e-05 m  y' = 9.78e-06
s = 3.48e-05 m  δ  = 2.32e-03
```

Figure B.8.: The 1 nC bunch at the start of the undulator section in the FLASH2 beam line.

B.2. Gaussian Distributions

Two particle distributions as used for the simulations of CSR induced emittance growth, presented in section 6.4. The first distribution presented in figure B.9 has a bunch charge of 250 pC and the bunch charge of the second distribution, presented in figure B.10, is 1 nC. The peak current, the emittances and the energy spread comply with the corresponding parameters of the particle distributions as used for the start-to-end simulations (cf. section B.1).

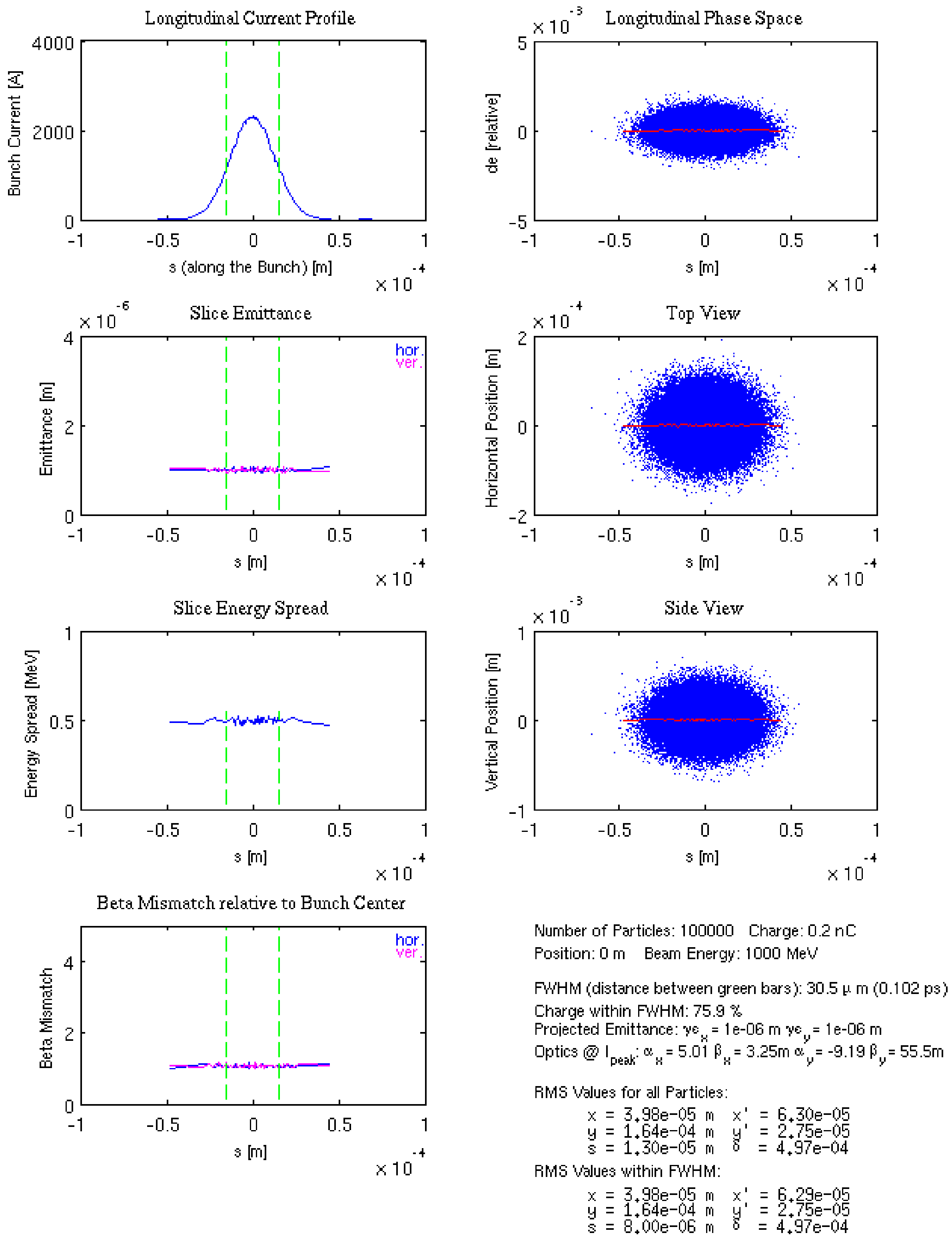

```
Number of Particles: 100000   Charge: 0.2 nC
Position: 0 m    Beam Energy: 1000 MeV

FWHM (distance between green bars): 30.5 μ m (0.102 ps)
Charge within FWHM: 75.9 %
Projected Emittance: γε_x = 1e-06 m γε_y = 1e-06 m
Optics @ I_peak: α_x = 5.01 β_x = 3.25m α_y = -9.19 β_y = 55.5m

RMS Values for all Particles:
        x = 3.98e-05 m   x' = 6.30e-05
        y = 1.64e-04 m   y' = 2.75e-05
        s = 1.30e-05 m   δ  = 4.97e-04
RMS Values within FWHM:
        x = 3.98e-05 m   x' = 6.29e-05
        y = 1.64e-04 m   y' = 2.75e-05
        s = 8.00e-06 m   δ  = 4.97e-04
```

Figure B.9.: The 250 pC Gaussian distributed bunch as used for the simulations of the CSR induced emittance growth.

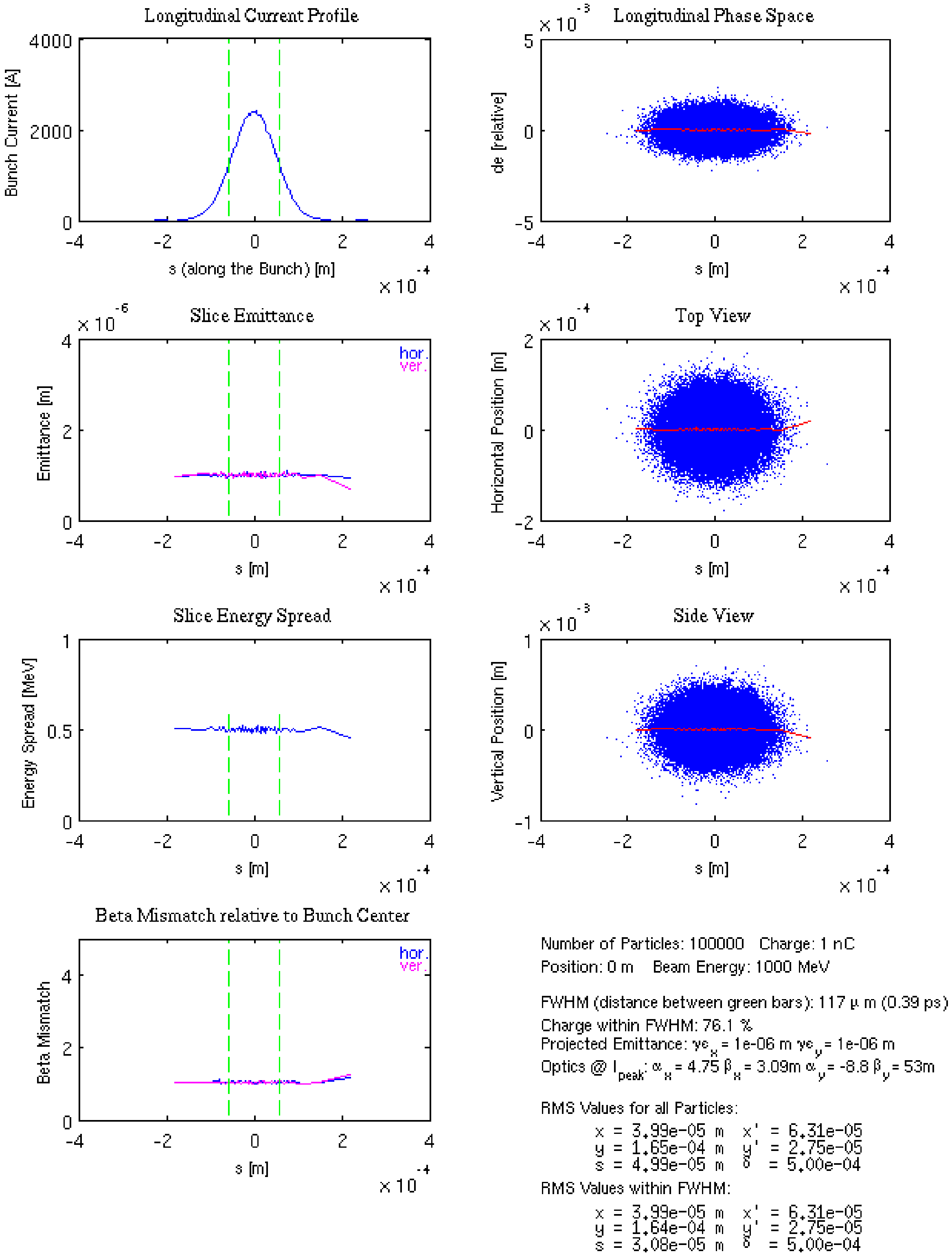

```
Number of Particles: 100000   Charge: 1 nC
Position: 0 m    Beam Energy: 1000 MeV

FWHM (distance between green bars): 117 μ m (0.39 ps)
Charge within FWHM: 76.1 %
Projected Emittance: γε_x = 1e-06 m γε_y = 1e-06 m
Optics @ I_peak: α_x = 4.75 β_x = 3.09m α_y = -8.8 β_y = 53m

RMS Values for all Particles:
        x = 3.99e-05 m   x' = 6.31e-05
        y = 1.65e-04 m   y' = 2.75e-05
        s = 4.99e-05 m   δ  = 5.00e-04
RMS Values within FWHM:
        x = 3.99e-05 m   x' = 6.31e-05
        y = 1.64e-04 m   y' = 2.75e-05
        s = 3.08e-05 m   δ  = 5.00e-04
```

Figure B.10.: The 1 nC Gaussian distributed bunch as used for the simulations of the CSR induced emittance growth.

C. Simplex Optimization Code

The MATLAB script for a simple example of the downhill simplex algorithm as described in chapter 5. The plots produced with this script are presented in figure 5.2.

```
global xrange yrange

tolerance = 1e-3;

xrange = -2.5:.1:2.5;
yrange = -1.5:.1:3.5;

plotpicture

alpha =  1.0;    % reflection coefficient
gamma =  2.0;    % expansion coefficient
rho   = -0.5;    % contraction coefficient
sigma =  0.5;    % reduction  coefficient

counter = 0;
matrix = zeros(2+1,3);

%% get the first n+1 positions

while (counter == 0);
    randomx = min(xrange) + (max(xrange)-min(xrange)).*rand(3,1);
    randomy = min(yrange) + (max(yrange)-min(yrange)).*rand(3,1);

    for i = 1:3
        matrix(i,1:2) = [randomx(i) randomy(i)];
        matrix(i,3) = testfunction(randomx(i), randomy(i));
    end

    if ((max(matrix(:,end))-min(matrix(:,end)))/min(matrix(:,end)) > ...
        tolerance)
        break
    end

    disp('bad random numbers... :-( I''l do it again')
end
```

```
[Y,I]=sort(matrix(:,3));
matrix=matrix(I,:);

triangle = [matrix(:,1:2); matrix(1,1:2)];
hold on
plot(triangle(:,1), triangle(:,2), 'k', 'linewidth',2)

%% start the loop here!

while ((max(matrix(:,end))-min(matrix(:,end)))/min(matrix(:,end)) > ...
    tolerance && counter < 2000) % stop criteria

    xmin = [matrix(1,1) matrix(1,2)];
    xmed = [matrix(2,1) matrix(2,2)];
    xmax = [matrix(3,1) matrix(3,2)];                         % x-values of ...
        the highest function value
    xg   = [sum(matrix(1:2,1)) sum(matrix(1:2,2))]/2;         % center of ...
        the 2 best positions
    xr   = xg + alpha * (xg -xmax);

    ymin = matrix(1,3);                                       % smallest ...
        function value
    ymed = matrix(2,3);
    ymax = matrix(3,3);
    yg   = testfunction(xg(1), xg(2));
    yr   = testfunction(xr(1), xr(2));                        % function ...
        value of the reflected position

    if (yr < ymed)
        if (yr < ymin)
            xe = xg + gamma * (xg-xmax);
            ye = testfunction(xe(1), xe(2));

            if (ye < yr)
                matrix(3,:) = [xe ye];
                disp('Expansion')
                triangle = [matrix(:,1:2); matrix(1,1:2)];
                plot(triangle(:,1), triangle(:,2),  'Color', [143 89 ...
                    2]/255, 'linewidth',3)
            else
                matrix(3,:) = [xr yr];
                disp('Reflection')
                triangle = [matrix(:,1:2); matrix(1,1:2)];
```

```
                plot(triangle(:,1), triangle(:,2),  'Color', [245 121 ...
                    0]/255, 'linewidth',3)
            end

        else
            matrix(3,:) = [xr yr];
            disp('Reflection')
            triangle = [matrix(:,1:2); matrix(1,1:2)];
            plot(triangle(:,1), triangle(:,2),  'Color', [245 121 0]/255, ...
                'linewidth',3)
        end

    else
        xc = xg + rho * (xg-xmax);
        yc = testfunction(xc(1), xc(2));

        if (yc < ymax)
            matrix(3,:) = [xc yc];
            disp('Contraction')
            triangle = [matrix(:,1:2); matrix(1,1:2)];
            plot(triangle(:,1), triangle(:,2),  'Color', [114 159 ...
                207]/255, 'linewidth',3)
        else
            xi1 = xmed - sigma * (xmed - xmin);
            xi2 = xmax - sigma * (xmax - xmin);

            yi1 = testfunction(xi1(1), xi1(2));
            yi2 = testfunction(xi2(1), xi2(2));

            matrix(2,:) = [xi1 yi1];
            matrix(3,:) = [xi2 yi2];
            disp('Reduction')
            triangle = [matrix(:,1:2); matrix(1,1:2)];
            plot(triangle(:,1), triangle(:,2), 'Color', [115 210 22]/255, ...
                'linewidth',3)
        end
    end

    [K,I] = sort(matrix(:,end));
    matrix = matrix(I,:);

    counter = counter + 1;
end
```

```
plot(triangle(:,1), triangle(:,2), 'r', 'linewidth',3)
scatter(matrix(1,1), matrix(2,1), 'Marker', 's', 'SizeData', 200, ...
    'MarkerFaceColor', [242 142 0 ]/255, 'MarkerEdgeColor', [242 142 0 ]/255)
display(['The number of iteration steps was ' num2str(counter)])
```

The plot function as used in the script above:

```
function plotpicture

global xrange yrange m

m = zeros(length(xrange), length(yrange));

for i = 1:length(xrange)
    for j = 1:length(yrange)
        m(i,j) = testfunction(xrange(j), yrange(i));
    end
end

figure
axes('FontSize',28);
contourf(xrange, yrange, m, 50)
xlabel('x','FontSize',30)
ylabel('y','FontSize',30)
colormap(jet)
colorbar('location','eastoutside','FontSize',30)
```

The different example functions for the optimization as used in the script above:

```
Function [f, x, y] = testfunction(x, y)
% f = (1/2 * exp(-(x - 5).^2/5) + exp(-(x + 2).^2/8)) * (-1/5 * exp(-(y + ...
    0).^2/13) - 1/8 * exp(-(y + 5).^2/5))+0.21;

%  Himmelblau function
% f = (x.^2+y-11).^2+(x+y.^2-7).^2;

% Rosenbrock function

f = (1-x)^2 + 100*(y-x^2)^2;
```

D. Mismatch Parameter and Mismatch Amplitude

A deviation of the beta function from the theoretical value at any position in the lattice will be transferred along the machine. The deviation and its development can be described with two parameters, the mismatch parameter and the mismatch amplitude which will be derived in this section.

The following calculations start with the solutions for $x(s)$ and $x'(s)$ from the Hill equation which can be found e.g. in [35]. The description of the transfer matrix's derivation as presented below is based on [36]. All calculations will be carried out for the horizontal plane but they can also be applied on the vertical plane. In order to simplify the formulas we define $x_0 = x(0)$, $x_s = x(s)$ and apply the same rule also on the Twiss parameters α, β, γ and on the phase advance ϕ.

$$x_s = \sqrt{\epsilon\beta_s}\cos\left(\phi_s + \phi_0\right) \tag{D.1}$$

$$x'_s = -\sqrt{\frac{\epsilon}{\beta_s}}\left[\alpha_s\,\cos\left(\phi_s + \phi_0\right) + \sin\left(\phi_s + \phi_0\right)\right] \tag{D.2}$$

In the next step, the solutions for the Hill equation can be written as:

$$x_s = \sqrt{\epsilon\beta_s}\left(\cos\phi_s\cos\phi_0 - \sin\phi_s\sin\phi_0\right) \tag{D.3}$$

$$x'_s = -\sqrt{\frac{\epsilon}{\beta_s}}\left(\alpha_s\cos\phi_s\cos\phi_0 - \alpha_s\sin\phi_s\sin\phi_0 + \sin\phi_s\cos\phi_0 + \cos\phi_s\sin\phi_0\right). \tag{D.4}$$

In order to determine $\sin\phi_0$ and $\cos\phi_0$, we consider the last two equations at the position $s = 0$ and we define $\phi_0 = 0$.

$$x_0 = \sqrt{\epsilon\beta_0}\cos\phi_0 \qquad \Leftrightarrow \qquad \cos\phi_0 = \frac{x_0}{\sqrt{\epsilon\beta_0}} \tag{D.5}$$

$$x'_0 = -\sqrt{\frac{\epsilon}{\beta_0}}\left(\alpha_0\cos\phi_0 + \sin\phi_0\right) \qquad \Leftrightarrow \qquad \sin\phi_0 = -\frac{1}{\sqrt{\epsilon}}\left(x'_0\sqrt{\beta_0} + \frac{\alpha_0 x_0}{\sqrt{\beta_0}}\right) \tag{D.6}$$

Insert $\cos\phi$ and $\sin\phi$ as calculated above in the solutions from the Hill equation like presented in equation D.3 and D.4:

$$x_0 = \sqrt{\frac{\beta_s}{\beta_0}}\,(\cos\phi_s + \alpha_0 \sin\phi_s)\ x_0 + \sqrt{\beta_s\beta_0}\sin\phi_s\ x_0' \tag{D.7}$$

$$x_0' = \frac{1}{\sqrt{\beta_0\beta_s}}\left[(\alpha_0-\alpha_s)\cos\phi_s - (1+\alpha_0\alpha_s)\sin\phi_s\right]\ x_0 + \sqrt{\frac{\beta_0}{\beta_s}}\,(\cos\phi_s - \alpha_s\sin\phi_s)\ x_0' \tag{D.8}$$

The last two equations can be written in matrix form:

$$\begin{pmatrix} x_s \\ x_s' \end{pmatrix} = \begin{pmatrix} \sqrt{\frac{\beta_s}{\beta_0}}\,(\cos\phi_s + \alpha_0\sin\phi_s) & \sqrt{\beta_s\beta_0}\sin\phi_s \\ \frac{(\alpha_0-\alpha_s)\cos\phi_s - (1+\alpha_0\alpha_s)\sin\phi_s}{\sqrt{\beta_0\beta_s}} & \sqrt{\frac{\beta_0}{\beta_s}}\,(\cos\phi_s - \alpha_s\sin\phi_s) \end{pmatrix} \begin{pmatrix} x_0 \\ x_0' \end{pmatrix} \tag{D.9}$$

This transfer matrix can be used when the Twiss functions at both positions, β_0, α_0 respectively β_s, α_s, and the corresponding phase advance ϕ_s are known.

The next step deriving the parameters for the β-beating is to investigate the course of the mismatched beta function along the beam line. For this reason, the functions $\tilde{\beta}_0$, $\tilde{\alpha}_0$ and $\tilde{\gamma}_0$ respectively $\tilde{\beta}_s$, $\tilde{\alpha}_s$ and $\tilde{\gamma}_s$ will be introduced. This functions describe the mismatched Twiss parameters at the start and at the end position.

If the elements of a transfer matrix for the particle's positions x and x' are indexed like shown in equation D.10:

$$\begin{pmatrix} x_s \\ x_s' \end{pmatrix} = \begin{pmatrix} m_{11} & m_{12} \\ m_{21} & m_{22} \end{pmatrix} \begin{pmatrix} x_0 \\ x_0' \end{pmatrix}, \tag{D.10}$$

then we can write the transfer matrix for the Twiss parameters β, α and γ as shown below in equation D.11 [35]:

$$\begin{pmatrix} \beta_s \\ \alpha_s \\ \gamma_s \end{pmatrix} = \begin{pmatrix} m_{11}^2 & -m_{11}m_{12} & m_{12}^2 \\ -m_{11}m_{21} & m_{12}m_{21} + m_{11}m_{22} & -m_{12}m_{22} \\ m_{12}^2 & -2m_{21}m_{22} & m_{22}^2 \end{pmatrix} \begin{pmatrix} \beta_0 \\ \alpha_0 \\ \gamma_0 \end{pmatrix} \tag{D.11}$$

If we take this transfer matrix and if we use the elements of the matrix as presented in equation D.9 we are able to calculate the ratio of the perturbed β-function divided by the unperturbed β-function at the end position. This ratio depends only on the Twiss functions at the start position and on the phase advance ϕ_s.

$$\Rightarrow \quad \tilde{\beta}_s = m_{11}^2 \tilde{\beta}_0 - 2\tilde{\alpha}_0 m_{11} m_{12} + m_{12}^2 \tilde{\gamma}_0 \tag{D.12}$$

$$\Leftrightarrow \quad \frac{\tilde{\beta}_s}{\beta_s} = \frac{\tilde{\beta}_0}{\beta_0} \left(\cos\phi_s + \alpha_0 \sin\phi_s\right)^2 - 2\left(\cos\phi_s + \alpha_0 \sin\phi_s\right) \tilde{\alpha}_0 \sin\phi_s + \beta_0 \tilde{\gamma}_0 \sin^2\phi_s \tag{D.13}$$

$$= \frac{\tilde{\beta}_0}{\beta_0} \cos^2\phi_s + \left(\frac{\tilde{\beta}_0}{\beta_0}\alpha_0^2 - 2\alpha_0\tilde{\alpha}_0 + \beta_0\tilde{\gamma}_0\right) \sin^2\phi_s + \left(\frac{\tilde{\beta}_0}{\beta_0}\alpha_0 - \tilde{\alpha}_0\right) 2\sin\phi_s\cos\phi_s, \tag{D.14}$$

The following formulas for trigonometric functions will be applied on equation D.14 in the next steps:

$$\begin{aligned} c_1\ \cos^2\theta + c_2\ \sin^2\theta &= \frac{c_1 + c_2}{2} + \frac{c_1 - c_2}{2}\cos 2\theta \\ c_3\ \sin 2\theta \cos\theta &= c_3\ \sin 2\theta \end{aligned} \tag{D.15}$$

$$\text{with} \quad c_1 = \frac{\tilde{\beta}_0}{\beta_0}, \qquad c_2 = \frac{\tilde{\beta}_0}{\beta_0}\alpha_0^2 - 2\alpha_0\tilde{\alpha}_0 + \beta_0\tilde{\gamma}_0, \qquad c_3 = \frac{\tilde{\beta}_0}{\beta_0}\alpha_0 - \tilde{\alpha}_0.$$

With this modifications, equation D.14 can be written as:

$$\begin{aligned} \Rightarrow \quad \frac{\tilde{\beta}_s}{\beta_s} &= \frac{1}{2}\left(\frac{\tilde{\beta}_0}{\beta_0} + \frac{\tilde{\beta}_0}{\beta_0}\alpha_0^2 - 2\alpha_0\tilde{\alpha}_0 + \beta_0\tilde{\gamma}_0\right) \\ &+ \frac{1}{2}\left(\frac{\tilde{\beta}_0}{\beta_0}\left(1 - \alpha_0^2\right) + 2\alpha_0\tilde{\alpha}_0 - \beta_0\tilde{\gamma}_0\right)\cos 2\phi_s + \left(\frac{\tilde{\beta}_0}{\beta_0}\alpha_0 - \tilde{\alpha}_0\right)\sin 2\phi_s. \end{aligned} \tag{D.16}$$

$$\begin{aligned} \text{Define the mismatch parameter} \quad & m_p := \frac{1}{2}\left(\tilde{\beta}_0\gamma_0 - 2\alpha_0\tilde{\alpha}_0 + \beta_0\tilde{\gamma}_0\right) \\ \text{and use} \quad & \frac{\tilde{\beta}_0}{\beta_0} + \frac{\tilde{\beta}_0}{\beta_0}\alpha_0^2 = \tilde{\beta}_0\left(\frac{1 + \alpha_0^2}{\beta_0}\right) = \tilde{\beta}_0\gamma_0 \end{aligned}$$

$$\Rightarrow \quad \frac{\tilde{\beta}_s}{\beta_s} = m_p + \left(\frac{\tilde{\beta}_0}{\beta_0} - m_p\right)\cos 2\phi_s + \left(\frac{\tilde{\beta}_0}{\beta_0}\alpha_0 - \tilde{\alpha}_0\right)\sin 2\phi_s \tag{D.17}$$

The last modification using operations on trigonometric functions will be carried out with the following rules and parameter definitions:

$$\begin{aligned} \text{Using} \quad & c_4\cos\theta + c_5\sin\theta = \sqrt{c_4^2 + c_5^2}\ \cos\left(\theta + \chi\right) \\ \text{with} \quad & c_4 = \frac{\tilde{\beta}_0}{\beta_0} - m_p, \qquad c_5 = \frac{\tilde{\beta}_0}{\beta_0}\alpha_0 - \tilde{\alpha}_0 \quad \text{and} \quad \chi = \arctan\frac{c_5}{c_4}. \end{aligned}$$

This changes the ratio of the beta functions to:

$$\Rightarrow \quad \frac{\tilde{\beta}_s}{\beta_s} = m_p + \sqrt{\left(\frac{\tilde{\beta}_0}{\beta_0} - m_p\right)^2 + \left(\frac{\tilde{\beta}_0}{\beta_0}\alpha_0 - \tilde{\alpha}_0\right)^2} \cos\left(2\phi_s + \chi\right). \tag{D.18}$$

Taking into account that

$$\left(\frac{\tilde{\beta}_0}{\beta_0} - m_p\right)^2 + \left(\frac{\tilde{\beta}_0}{\beta_0}\alpha_0 - \tilde{\alpha}_0\right)^2 = m_p^2 - 1,$$

we conclude that the ratio of the perturbed and the unperturbed β-function at the end position can be simplified to:

$$\Rightarrow \quad \frac{\tilde{\beta}_s}{\beta_s} = m_p + \sqrt{m_p^2 - 1}\ \cos\left(2\phi_s + \chi\right) \tag{D.19}$$

The mismatch parameter m_p is generally used to describe the mismatch between the theoretical Twiss parameters and the Twiss parameters of the beam at a certain position e.g. the entrance of the undulator section. Its range is given by:

$$1 \leq m_p \leq \infty$$

and $m_p = 1$ is given if there is no mismatch between the machine and the beam.

The amplitude of equation D.19 is called the mismatch amplitude

$$\lambda_{\mathrm{mp}} = m_p + \sqrt{m_p^2 - 1}. \tag{D.20}$$

It can be used to describe the envelope of a perturbed beta function $\tilde{\beta}_s$ around the unperturbed beta function β_s along the beam line. The amplitude of the oscillation can be described as follows:

$$\frac{1}{\lambda_{\mathrm{mp}}}\beta_s \ \leq \ \tilde{\beta}_s \ \leq \ \lambda_{\mathrm{mp}}\,\beta_s, \tag{D.21}$$

which was used in plot 6.20.

E. Mismatch Ellipses

In this chapter, the calculation of the mismatch ellipses as used in plot 6.10 will be presented. Starting with the mismatch parameter defined in the last chapter

$$m_p = \frac{1}{2}\left(\tilde{\beta}\gamma - 2\alpha\tilde{\alpha} + \beta\tilde{\gamma}\right), \tag{E.1}$$

one can obtain $\tilde{\alpha}$ using the pq-formula:

$$\tilde{\alpha}_{1/2} = \frac{1}{\beta^2}\left[\alpha\beta\tilde{\beta} \pm \sqrt{-\beta^4 + 2\ m_p\beta^3\tilde{\beta} - \beta^2\tilde{\beta}^2}\right] \tag{E.2}$$

Set the discriminant of the last equation to zero and calculate using the pq-formula $\tilde{\beta}_{\mathrm{min}}$ and $\tilde{\beta}_{\mathrm{max}}$:

$$\tilde{\beta}_{\mathrm{min}} = m_p\beta - \sqrt{-\beta^2 + m_p^2\beta^2} \tag{E.3}$$

$$\tilde{\beta}_{\mathrm{max}} = m_p\beta + \sqrt{-\beta^2 + m_p^2\beta^2} \tag{E.4}$$

Plotting $\tilde{\alpha}_1$ and $\tilde{\alpha}_2$ as a function of $\tilde{\beta}$ gives the wanted ellipse around the ideal Twiss parameters α and β as presented in plot 6.10.

F. Extraction Layout

A top view of the FLASH2 extraction layout including the existing beam line FLASH1 is depicted in Fig. F.1. The picture on the left hand side shows the machine starting from a collimator upstream the vertical kickers to the end of the arc and to a possible extraction position for a proposed third beam line. On the right hand side, one can see a zoom in depiction of the extraction position starting with the septum. In this picture it becomes apparent that there is very little space left for additional elements.

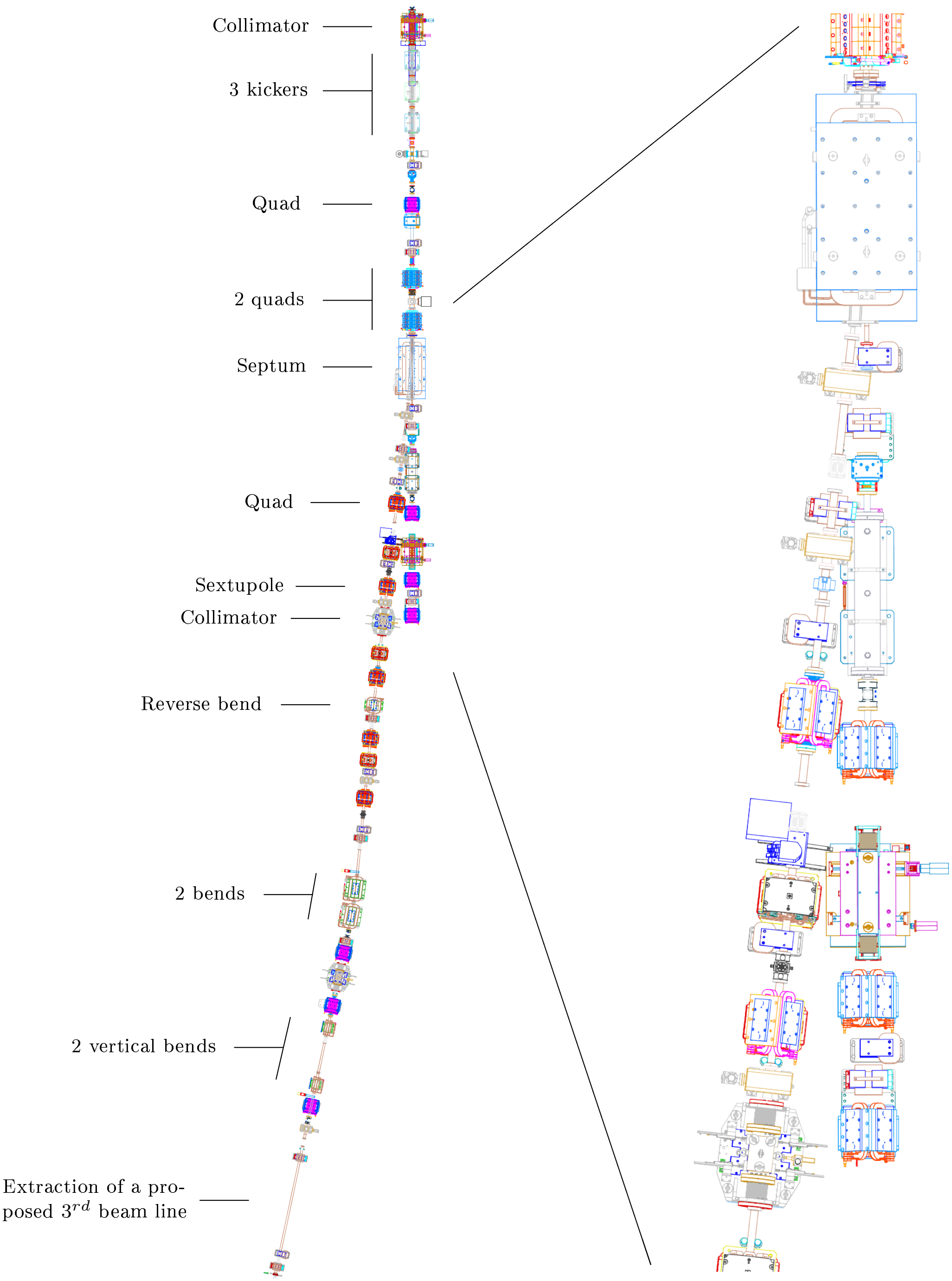

Figure F.1.: Top view of the extraction arc for FLASH2 showing all elements including magnets, diagnostics and vacuum devices. The picture on the left hand side shows the full extraction arc starting with a transverse collimator, three vertical kickers and the septum and ending with the possible extraction position of the proposed third beam line. On the left hand side one can see a zoomed in picture of the septum and the following elements in order to emphasis the limited space available. (CAD drawings in courtesy of J. Gonschior)

Bibliography

[1] History of DESY: desy2.desy.de/e42/, July 2013.

[2] History of BESSY: www.helmholtz-berlin.de, July 2013.

[3] Wikipedia article for ”Synchrotron Radiation Source (SRS)”: en.wikipedia.org/wiki/Synchrotron_Radiation_Source, June 2013.

[4] A. Jackson, *The Advanced Light Source - Status Report*, Lawrence Berkeley Laboratory, Berkeley, CA 94720, USA, Proceedings of PAC 1991, San Francisco, CA, USA.

[5] R. P. Walker, *The ELETTRA Synchrotron Radiation Facility*, Sincrotrone Trieste, Trieste, Italy, Rev. Sci. Instrum. 63 (1), January 1992.

[6] J.-L. Laclare, *ESRF x-ray synchrotron radiation source*, European Synchrotron Radiation Facility, 38043 Grenoble Cedex, France, Rev. Sci. Instrum. 60 (7), July 1989.

[7] PETRA3 web page: petra3.desy.de, June 2013.

[8] R. R. Stone et al., *An FEL-Based Microwave System for Fusion*, Journal of Fusion Energy, Vol. 9, No. 1, 1990, Page 77.

[9] P. Emma et al., *First lasing and operation of an ångstrom-wavelength free-electron laser*, Nature Photonics 4, 641-647; 2010).

[10] M. Altarelli et al., *The European X-Ray Free-Electron Laser Technical Design Report*, DESY 2006-097, July 2007.

[11] Photo Science at DESY web page: photon-science.desy.de, June 2013.

[12] S. Schreiber et al., *FEL User Facility FLASH*, Proceedings of IPAC’10, Kyoto, Japan.

[13] FLASH web page: flash.desy.de, June 2013.

[14] M. Dohlus, J. Rossbach and P. Schmüser, *Ultraviolet and Soft X-Ray Free-Electron Lasers*, Springer, May 2008.

[15] DESY web page: www.desy.de, November 2012.

[16] H. Wiedemann, *Particle Accelerator Physics*, Springer; Auflage: 3rd ed. 2007 (4. Mai 2007).

[17] M. Dohlus, private communication.

[18] E. L. Saldin, E.A. Schneidmiller and M.V. Yurkov, *Design Formulas For VUV and X-Ray FELs*, Proceedings of the 2004 FEL Conference, 139-142, Trieste, Italy.

[19] M. Xie, *Exact and variational solutions of 3D eigenmodes in high gain FELs*, Nucl. Instr. Meth. A 445 (2000) 59-66.

[20] K.-J. Kim, M. Xie, *Self-amplified spontaneous emission for short wavelength coherent radiation*, Nucl. Instr. Meth. A 331 (1993) 359-364.

[21] M. Dohlus, T. Limberg and P. Emma, *Bunch Compression for Linac-based FELs*, International Committee for Future Accelerators, Beam Dynamics Newsletter No. 38, December 2005.

[22] M. Dohlus, T. Limberg, *Emittance growth due to wake fields on curved bunch trajectories*, Nucl. Instr. Meth. A 393 (1997) 494-499.

[23] B. Faatz et al., *Flash II: Perspectives and challenges*, Nucl. Instr. Meth. A 635 (2011) S2-S5.

[24] B. Faatz, private communication.

[25] FLASH web page: flash2.desy.de, June 2013.

[26] B. Faatz et al., *Simultaneous operation of a multi beamline FEL facility*, Proceedings of 2012 FEL Conference, Nara, Japan.

[27] M. Borland, *elegant: A Flexible SDDS-Compliant Code for Accelerator Simulation,* Advanced Photon Source LS-287, September 2000.

[28] R. Horst, P. M. Pardalos and N. V. Thoai, *Introduction to Global Optimization*, 2^{nd} edition, Kluver, 2000. Page 10.

[29] M. Dohlus, T. Limberg, *CSRtrack Version 1.2*, web page: www.desy.de/xfel-beam/csrtrack, March 2013.

[30] S. Reiche, GENESIS web page: http://genesis.web.psi.ch, July 2013.

[31] G. R. Lambertson, *Extractor for high energy charged particles*, United States Patent Office 3,128,405, Patented April 7, 1964.

[32] D. Meeker, *Finite Element Methods Magnetics Version 4.2, femm4.2.*, 2013.

[33] E.-S. Kim, Korea *Bunch Compressors*, Kyungpook National University, ILC Accelerator School, May 2006.

[34] K. Floettmann, *Astra, A Space Charge Tracking Algorithm*, DESY.

[35] J. Rossbach, P. Schmüser, *Basic Course on Accelerator Optics*, CERN Accelerator School, Fifth General Accelerator Physics Course, University of Jyväskylä, Finland, 7-18 September 1992.

[36] B. Holzer, *Lecture: Introduction to transverse beam optics*, CERN.

Acknowledgments

I want to thank Prof. Dr. Jörg Roßbach for being my doctoral thesis supervisor. His interesting lecture at the University of Hamburg regarding accelerator physics convinced me a few years ago to change the main focus of my studies to the field of the particle accelerators and I am still very happy with this decision.

Grateful thanks go to Prof. Dr. Eckhard Elsen for reviewing my thesis. He was also the supervisor and reviewer of my diploma thesis at CERN and I have very good memories of that time.

I would like to thank Dr. Winfried Decking and Dr. Torsten Limberg for tutoring me during my PhD thesis. I appreciated the friendly relationship during the last years and the pleasant working environment in our group. The support from both was always very helpful and I felt always welcome in their offices.

I want to thank also Dr. Bart Faatz, project leader of FLASH II, for many fruitful discussions and for the friendly teamwork. It was a good experience to work with him and to be part of the FLASH II project. Grateful thanks to all my colleagues from the FEL beam dynamics group at DESY. It was great to work with you and I am very thankful for all the help which I received during the last years. I want also to thank my office colleagues and friends at DESY for the nice time we had together and I am sure that the friendships will remain after our time at DESY.

I am also very happy to have Alex as very good friend in Hamburg and I really enjoyed our weekly lunch at the small Italian restaurant on Friday afternoons. It's a great pleasure to know you.

I would like to thank my family for all the support and the familial cohesion which we have. Special thanks are directed to my wife Sonja for the help and backing during the last three years and I want you to know that I am really happy that everything is like it is. I am looking forward to have many years to come with you and I am sure we will have a great time.